POROSITY CONTROL OF ALKALI-ACTIVATED ALUMINOSILICATES VIA FUNCTIONAL ALKOXYSILANE ADDITIVES

BY

BRAYDEN E. GLAD

DISSERTATION

Submitted in partial fulfillment of the requirements
for the degree of Doctor of Philosophy in Materials Science and Engineering
in the Graduate College of the
University of Illinois at Urbana-Champaign, 2013

Urbana, Illinois

Doctoral Committee:

Professor Waltraud M. Kriven, Chair
Professor John R. Abelson
Emeritus Professor James Economy
Professor Leslie J. Struble

ABSTRACT

Geopolymers were synthesized with alkoxysilane and other organo-silane supplements to improve adhesion to organic polymers and to modify porosity. Uncured geopolymer slurry was found to be miscible with various alkoxysilanes, and the resulting cured geopolymer strongly adhered to organic polymers if and only if the alkoxysilane possessed an appropriate coupling agent linking group for the polymer. Issues relating to maximizing reactivity and properly measuring the porosity of these complex systems using gas adsorption porosimetry and mercury intrusion porosimetry (MIP) were addressed. A new pore size distribution calculation using MIP results was tested and applied.

Geopolymer mesoporosity could be minimized through the use of alkoxysilanes with acrylic acid or similar functional groups, which Fourier transform infrared spectroscopy identified as transforming to sodium acrylates in the high pH of the geopolymer system. Transmission and scanning electron microscopy identified the self-assembly of 100 nm-1μm sheets and tubes of the acrylate-functional alkoxysilane which bound strongly to geopolymer precipitates. These small phases were able to inhibit the sequestration of surplus water in mesoporous structures through a waterlocking mechanism. Numerous property modifications were observed as a result. Examination with nitrogen adsorption showed an order of magnitude decrease in mesopore volume, while compressive testing found a 48% increase in Weibull modulus for compressive strength and a probable increase in compressive strength. Mercury intrusion porosimetry measurements showed up to a 24% increase in bulk density. Meaningful property modification and mesoporosity reduction required the addition of at least 0.06 mol acrylate/mol geopolymer, and no sheet or tube phases were observed with smaller amounts of acrylate. This is consistent with a saturation model in which about 0.06 mol/mol of alkoxysilane

monomer is able to co-precipitate directly with the geopolymer, and any surplus forms the sheet or tube phase.

Dilute emulsions of geopolymer reagents with organo-silanes were capable of producing highly porous monolithic solids through templating and surface modification, with or without an additional hydrophobic phase. In the dilute geopolymer emulsion, dimethyldiethoxysilane demonstrated the least phase separation of the several organo-silanes tested and created the most porous monoliths. X-ray diffraction and Fourier transform infrared spectroscopy data illustrated limited geopolymerization in dilute slurries with or without organic additives, but this limitation was reduced through extended mixing of more concentrated slurry, followed by further dilution. Mercury intrusion porosimetry data illustrated the creation of percolating network porous solids with controllable porosity within the range of 60 vol% to 80 vol% or more, and controlled critical percolation pore sizes within the range of approximately 500 nm to the tens of μm. Critical percolation pore size was observed to increase with increasing porosity, and to decrease with increasing emulsion stability. Scanning electron microscopy illustrated the creation of an organic film on the interior surfaces of the pore network. Firing the porous geopolymer at 800 ºC for 4 hours in a nitrogen atmosphere removed the organic film and increased porosity without meaningfully increasing critical percolation pore size. The fired geopolymer sample had X-ray diffraction characteristics of an amorphous glass and demonstrated increased strength. A hard minor phase was identified as ß-SiC.

ACKNOWLEDGEMENTS

This project carries as much the imprint of my caring advisor, Professor Waltraud M. Kriven, as it does mine. I am grateful for the assistance of the Kriven research group members, especially Dr. Pankaj Sarin, Dr. Ryan Haggarty, Dr. Nipa Yossakda, Dr. Pathikumar Sellappan, Dr. Robert Hughes, Zladomir Apostolov, Thomas Carlson, Gregory Kutyla, and Yufan Ding, for assistance with theoretical discussions, measurements or other aspects of the project. Lab coordinators John Bukowski and Nicole Robards, and physical science technician Kyle Webb were vital in assisting with various logistical issues. Additionally, I appreciate the assistance of Dr. Chan Han and Dr. Aleksander Pyzik at the Dow Chemical Company, for their continual consultation and assistance their lab provided. This project would not have been possible without the funding from Dow Chemical Company.

Just as vital to this project has been the earnest support of my family and friends through these several years. Their interest, encouragement and love have made this effort worthwhile.

TABLE OF CONTENTS

CHAPTER 1

INTRODUCTION

Alkali-activated aluminosilicates, or geopolymers[1] (GP), are a class of hard, brittle materials which possess properties of both traditional cementitious materials and engineering ceramics. Their superior mechanical properties to Portland cement provide interest in large-scale manufacturing, while the ability to process at ambient conditions allows for uses that are impractical for traditional fired ceramics.

The material is surprisingly resilient to compositional changes and the presence of impurities, allowing for synthesis from an array of waste materials including fly ash[2], slag[3], and even agricultural wastes[4]. Higher quality geopolymer is synthesized from clays, particularly the highly reactive metakaolin. The latter is more appropriate for engineering-quality ceramic products, producing a more consistent microstructure and a more fully reacted product.

However, understanding and control of geopolymerization and the resulting complicated microstructure is far from complete[5,6,7,8]. This lack of knowledge likely contributes to the wide variety of properties and observations of anomalous material behavior reported in the literature. At the same time, it is possible to successfully engineer specific bulk and microstructural properties using a variety of methods.

One of the most important microstructural parameters for geopolymers is porosity, yet little progress has been made in controlling or tailoring porosity. Reducing porosity is vital for mechanical purposes if geopolymer is to substitute for existing cementitious materials, while increasing the geopolymer porosity opens new applications such as thermal barrier coatings and filters. While some progress[9,10,11,12,13,14] toward porosity control has been made by altering various synthesis parameters, marked property changes have thus far been elusive, and a more

focused investigation is worthwhile. In particular, the great property improvements in Portland cement achieved though the simple addition of various organic materials such as high-range water reducers suggests organic additives might be beneficial for geopolymers as well.

1.1. Project Objectives

This project seeks to demonstrate quantitatively and qualitatively substantial modifications to the porosity of geopolymers without fundamentally altering their character as alkali-activated aluminosilicates. This character includes the simple room temperature and pressure synthesis and curing process mandatory for practical cementitious materials. To operate successfully within this constraint, the project relies upon modifying the geopolymer condensation process at a chemical and nanostructural level through the use of organic additives.

Even more importantly, the mechanisms by which various modifications occur must be fully described, in order that later optimization of the organic-modified geopolymer system can be possible. Currently, minimal knowledge of organically modified geopolymer exists. Observing in detail the interactions of various organic materials with geopolymer during and after the curing process both advances the theoretical understanding of geopolymers and assists the geopolymer community in expanding the use of this material in practical applications.

1.2. Approach

The complex and poorly understood nature of geopolymers has made modifying geopolymers with organic additives a convoluted task. As this project involves both ceramic engineering and polymer chemistry knowledge, the customary thorough review of the literature (Chapter 2) provided the interdisciplinary background so important for this task. It proved

necessary to specifically investigate the interaction of geopolymers with various organic materials, and it was found that certain alkoxysilane additives were able to avoid immediate phase separation from the geopolymer slurry, and thus affect cured properties (Chapter 3). The utilization of such additives posed the problem of reducing geopolymer reactivity, although procedure modifications greatly mitigated that reduction (Chapter 4). Additionally, the objective of understanding porosity modification made correct porosity characterization vital, and some modifications to existing techniques (Chapter 5) proved valuable for useful data about the complex porous structure of the organic-modified geopolymer.

Addressing these concerns along the way allowed for the goals of the project to be met. It was found that hydrogel-like water segregation within the curing geopolymer enabled extensive mesoporosity reduction (Chapter 6), and surface-energy driven liquid phase separation and dehydration methods allowed for the synthesis of highly porous geopolymers (Chapter 7).

CHAPTER 2

LITERATURE REVIEW

Geopolymers[1] have been studied extensively since their discovery, with most of the research having been conducted since 2000[15]. Today, the topic is generally accepted as its own subfield of materials science, with two recent books providing thorough reviews[6,7]. While much of the research has been involved with maximizing compressive and flexure strength, scientific investigations have also probed the effects of alkali-alumina ratio[16], alkali choice[17], alumina-silica ratio[16], choice of precursor[2,3,4,18], filler phases[19,20,21,22,23,24], and other processing considerations. The effects of these variables on microstructure are now generally understood[5].

Investigations of the porosity of geopolymers have been limited to date, likely because of the clear reduction in strength that pores provide. Despite some initial efforts[9,10,11,12,13,14,25,26], true control and understanding of porosity content and size in geopolymers has not been established. In particular, there has been no exhaustive investigation into control of pores smaller than approximately 20-50 μm[9], other than the 5-20 nm nanopores created within the geopolymer through precipitation[14]. Methods to create highly porous geopolymers with pore sizes between these ranges have not been successful.

Additionally, while certain broad patents mention the incorporation of organic materials into various aluminosilicates including geopolymers[27,28], only minimal scientific understanding of the results of such inclusion has been previously gained. In particular, the organic materials that have been incorporated into geopolymers have been incorporated as bulk phases[23,29,30]. In contrast, this document describes the applicability of monomeric organic additives to geopolymer formulations, and the microstructural control that such systems offer. While the effects of organic additives are well-known in the syntheses of zeolites[31] and various sol-gel

silicates such as aerogels[32], the inherent value of combining the simple synthesis of geopolymers with the advanced property control of these engineered aluminosilicates justifies an investigation. The ability for organic systems to self-organize in aqueous systems is unmatched by any inorganic material, so these additives provide the greatest possibility for porosity manipulation. A discussion of the known practical and theoretical considerations for these topics is presented in this section.

2.1. Geopolymer Properties

Geopolymers must be practically distinguished from other similar materials, in order to clearly illustrate the design space. As described in detail below, geopolymers possess properties of cementitious materials, geological minerals and polymer covalent resins, providing the logic behind the name[1]. However, there are important practical differences in both microstructure and bulk properties that differentiate these materials from any of the three classes of materials listed.

2.1.1. Microstructure

Geopolymer microstructure has been previously intensively investigated by a full slate of traditional characterization methods. For the length scale of nanometers to hundreds of nanometers, analysis using transmission electron microscopy and gas adsorption porosimetry has been most beneficial. For larger length scales, scanning electron microscopy has been the chief technique, combined with various bulk tests, including differential scanning calorimetry, mercury intrusion porosimetry, and various mechanical tests. At smaller length scales, x-ray and neutron diffraction, ^{29}Si and ^{27}Al nuclear magnetic resonance, and various spectroscopies have

provided significant insight into the nanostructure, and these results will be discussed in the chemistry portion of the review.

For sodium geopolymers synthesized from metakaolin, the literature[16] recognizes a clear Si·Al ratio effect on the microstructure. As the ratio increases over the range from 1.15-2.15, the geopolymer shows an increasingly homogenous structure at the length scale of μm, with some porosity at this length scale. At smaller ratios, particularly below 1.65, an extremely chaotic structure of loosely connected precipitates, random porosity and unreacted material occurs on a length scale of hundreds of nm. Using other materials often creates additional observable phases[2,33,34] that consist of unreacted impurities. Porosity is present at this length scale and smaller length scales, and will be discussed in detail below.

2.1.2. Mechanical Properties

Improving compressive and flexure strength has been perhaps the major focus of geopolymer research, as providing an alternative to traditional calcium-based cements has been a priority. Numerous techniques and results are summarized elsewhere[7]. Research has been quite successful, identifying formulations that are both relatively resilient to processing and compositional deviation and possessing compressive strength of approximately 80 MPa or more[5,35]. The modulus of rupture is also satisfactory, with the literature reporting widely spread values in the upper MPa and lower tens of MPa[36,37]. Tensile splitting strength[38,39] is also occasionally reported. Sudden brittle failure by cracking is characteristic of unmodified geopolymers.

2.1.3. Use as Composite Matrix

Mitigation of cracking failure has been accomplished by the addition of numerous filler phases, including carbon fibers[19,20], polymer fibers such as poly(vinyl alcohol) or polypropylene[21,40], metal mesh[22], concrete filler and other additives [23, 29,30,41]. The mentioned documents illustrate order-of-magnitude or more improvements over the unmodified geopolymer in properties such as work-to-failure and yield strain in tension or flexure. When mineral aggregates such as sand and other siliceous materials are used as filler, a composite is created without a detectable interfacial transition zone[24], implying very strong interfacial adhesion must occur as the geopolymer cures against the hardened silicate. Thus, it is possible to acquire the mechanical properties of typical concrete formulations fairly straightforwardly.

2.1.4. Other Uses

This natural adhesion to silicates and other ceramics was found to extend to some metals and investigated in detail[42]. This strong adhesive ability also allows for geopolymer to be used in encapsulation of toxic or nuclear wastes[43,44] due to its thermal stability. The same thermal stability allows for its use in insulation if made sufficiently porous[45], and as a catalyst support or a filter[46].

2.2. Geopolymer Chemistry

Geopolymer chemistry and nanostructure have been investigated very thoroughly, in an attempt to both improve bulk properties and to correctly categorize this class of materials. Based on ^{27}Al nuclear magnetic resonance, AlO_4^- was identified as the fundamental building block of the aluminate[47,48]. Use of ^{29}Si NMR allowed for a complete description of the interrelation of Si

and Al in the superstructure[49], identifying a range of systems of the form Si-O-(Si, Al). This included polysialates, polysiloxosialates and polydisiloxosialates[47] in short-range frameworks possessing the repeating units of various zeolites[8,50] such as zeolite A, Na-X and sodalite[1,51]. No Al-O-Al linkages are possible, as normal for aluminosilicates[52].

Geopolymers appear amorphous with a characteristic wide hump at approximately 28º 2-Θ when observed with x-ray diffraction, but electron diffraction is possibly capable of identifying crystallinity[8] at least in low-silica sodium geopolymers. This suggests that the individual precipitates may be too small to be detectible using XRD. This is consistent with pair distribution function studies[15,53,54] which identify minimal correlation beyond roughly a nanometer for either Cs or K geopolymers. The technique is confirmed by demonstrating the conversion of these geopolymers to pollucite and leucite at high temperature[15].

Transmission electron microscopy reveals a structure of agglomerated precipitates of approximately 5-40 nm in size[55,56]. In-situ FTIR studies identify the precipitation of an aluminum-rich phase first, followed by the gradual increase in silicon incorporation[57]. This has the result of an inhomogeneous nanostructure amongst and probably within the individual particulates, although efforts using even synchrotron radiation-based infrared microscopy with hierarchical clustering analysis lacked the resolution to fully analyze individual precipitates[57].

2.2.1. Precursors

As mentioned in the introduction, geopolymers can be synthesized from a vast array of clays, pozzolans, various ashes, minerals and other sources of aluminosilicate, and can be activated using aqueous alkali hydroxides, alkali silicate solutions ("waterglass")[1], and even sodium aluminate or other salts[58]. For practical uses, much of the focus has been on using

various ashes where unreactable material acts as filler[18] but unreacted clay sheets are sometimes observable with SEM in metakaolin-based geopolymers as well[59]. Due to the formulation of highly reactive 5-coordinated aluminum oxide structures[60,61], kaolin calcined in the range of 700 ºC to 750 ºC for 1 to 2 hours produces the best mechanical performance[62] of the various clays investigated, and metakaolin offers the scientific advantage over other precursors of minimal impurity phases.

The choice of alkali activator has been shown to be of great significance, with sodium silicate activator shown to produce a less homogenous microstructure and larger pores than a potassium silicate activator[17,63], perhaps due to differential dissolution kinetics of Al and Si by the activator[64] or differing radii of hydration [65]. It also affects the coefficient of thermal expansion, with cesium hydroxide activation possessing almost zero, while lower atomic numbered alkali have increasing coefficients of thermal expansion[15]. Neither the RbOH nor the CsOH precursor is usable for all but the greatest of value-added systems for cost reasons, and lithium based geopolymeric systems had appeared impossible by traditional synthesis means but might now be possible using some recent techniques[66].

2.2.2. Synthesis

Geopolymerization occurs through a well-recognized three-step process of dissolution of the aluminosilicate source, polycondensation of aluminosilicate oligomers into precipitate nucleation sites, and finally precipitation of individual geopolymer particles on the order of approximately 5-30 nm in diameter to create a gel, with the characteristic size increasing with alkali cation size[7,55,59]. Experiment has shown that starting from an aluminosilicate such as

metakaolin, which is a layered aluminosilicate of composition Al_2O_3•$2SiO_2$, and an aqueous alkali silicate, the reaction proceeds spontaneously as follows[1,7,67]:

$$Al_2O_3 \cdot 2SiO_2 + 2SiO_2 + \ 11H_2O + 2MOH \rightarrow 2MAl(OH)_4 + 4Si(OH)_4 \qquad (2.1)$$

Thus the bulk aluminosilicate is dissolved into monomers. The monomers then polymerize into oligomers, utilizing the additional silicate already in solution:

$$MAl(OH)_4 + n(Si(OH)_4) \rightarrow MAl(OH)_3(Si(OH)_2)_{n-1}Si(OH)_3 + n(H_2O) \qquad (2.2)$$

These oligomers (here indicated as linear, see below) continue to expel water through the condensation process, gradually cross-linking into a covalent network solid that eventually becomes insoluble in the typical manner of such networks:

$$x(MAl(OH)_3(Si(OH)_2)_{n-1}Si(OH)_3) \rightarrow$$

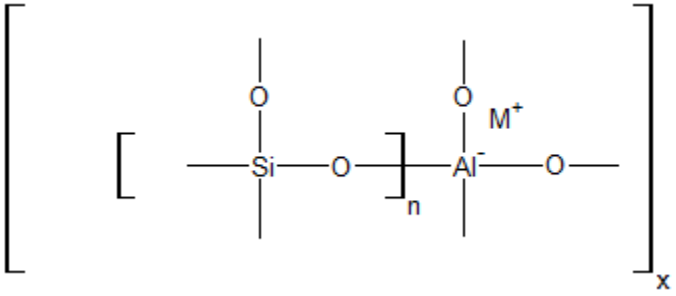

$$+(nx + 2x)H_2O \qquad (2.3)$$

The water synthesized from this reaction tends to be only a small portion of water initially added for rheological purposes, but sets a theoretical lower bound on minimum water content. In practice, alkali cations will bind a portion of the water within their radii of hydration, but not enough to fully solvate the cation as it is partially bound to the aluminate[65].

2.2.3. Curing

The synthesis of geopolymers is so straightforward that the only real considerations are the composition (discussed above) and the curing process. In hydrothermal conditions, the above reaction results in the creation of various zeolites, the study of which is an entire discipline of itself. It is believed that under geopolymerization conditions, insufficient water and heat prevent full synthesis of zeolite crystals and indeed, a relatively smooth transition has been observed between a geopolymer and a zeolite phase as temperature and curing time are increased[8].

Numerous investigations have provided a wealth of data from ambient conditions all the way to hydrothermal conditions. As a rule, temperature provides the greatest effect on properties[68,69] with elevated temperatures producing a weaker product[2,68]. Products produced without sealing generally experience cracking even at relative humidity as high as 70%[70], so the vast majority of experiments utilized sealed molds, although a few humidity-related investigations have been recently conducted[71,72].

2.3. Geopolymer Porosity

The considerable water forced out through this polycondensation reaction ultimately resides in mesopores, as described above. TEM[41] and gas adsorption porosimetry[14] identify the presence of extensive porosity at the length scale of 5-20 nm, which are considered to be spaces between individual precipitates. Differential scanning calorimetry with thermal gravimetric analysis and diliatometry provided evidence that these pores are filled with free water[59,73,74].

It is possible to artificially increase porosity through the use of evolved gasses[9,10,12,25,75], typically using silica fume or an oxidizing metal to evolve hydrogen gas. The oxygen-evolving

reaction using hydrogen peroxide has also been demonstrated[9]. It was found that the pores formed from the evolved gas were large macropores (20 μm to mm)[10,25,75], unless the samples were cured under positive pressure[9], which resulted in minimal porosity gain, cracking and other failures. This is consistent with the well-understood principle that gaseous bubbles in the slurry will not nucleate below a certain diameter[76], as well as the occurrence of cavitation below a certain diameter[77] due to the necessary high pressures required to maintain a highly curved surface.

Efforts to reduce porosity have been generally ineffective, with only relatively recent investigations showing much progress[65]. This is likely because geopolymer porosity tends to consist of both the mesopores between precipitates, which have been viewed as intrinsic to the structure, and macropore voids between aggregates of precipitates. The macropore voids can assume a variety of sizes up to the tens of μm depending on processing conditions[78], but rarely contribute large amounts of pore volume in dense formulations[9,14,56]. The macropores are effectively defects[7], and increasing the water used in geopolymer formulations tends to increase the volume of these macropores[14]. They are thus likely formed from excess water added for rheological reasons.

2.4. Functional Alkoxysilanes

Geopolymers make excellent composites in part because they easily accommodate bulk phases within the matrix by crosslinking around them. Unfortunately, the geopolymerization reaction's flexibility in handling impurities by crosslinking around them can be a curse as well as a blessing. It is difficult to ensure good dispersion of additive phases and prevent agglomeration during curing, particularly with organic additives. To address issues of phase separation, it is

vital that the adhesive performance of geopolymer to organic material be improved. A well-known method[79] of improving adhesion between glasses and organic materials is the incorporation of silane coupling agents at the interface between the silicate glass and the organic filler. These compounds possess both an organic functional group and a silicon atom, with leaving-groups attached to the silicon atom. These groups are most typically chlorine atoms[80], or various alkoxy groups. In a geopolymer, chlorine salts would result from the byproduct, which would result in worsening strength[81] as well as complicating the cation distribution in the geopolymer, so alkoxysilanes are better potential choices.

While the synthesis of useful alkoxysilanes has been known since at least 1867[82], and the compounds are ubiquitous in sol-gel chemistry as a precursor and in fiberglass manufacture as a sizing agent, little investigation of their interaction with either cured geopolymer or geopolymer slurry has been conducted, although a patent[27] now exists that covers the general system. Thus, the existing literature on the chemistry, physics and processing of these materials is substantial but requires consideration of the analogy between geopolymers and glasses. Additionally, the coating of a geopolymer with a sizing agent is a different task than is the reacting of such an agent during the curing process. In particular, alcohol, the expected byproduct of the alkoxysilane condensation, is known to inhibit the geopolymerization reaction[83] although this interaction has not been intensively investigated.

2.4.1. Chemistry

The fundamental idea of the alkoxysilane coupling agent is to bond covalently the agent to silanol groups on the surface of the silicate[84,85], although it is not altogether conclusive that full covalent bonding actually occurs[79,86]. In aqueous medium, the reaction could be expected to

resemble a sol-gel synthesis of a silicate gel if an approximately full reaction is assumed to occur. Under ambient conditions and neutral pH, however, the condensation reaction does not occur readily[79].

Catalysis of this reaction is therefore useful, though not required. This is most often conducted with organotin catalysts[87], but these chemicals are quite toxic[88] and would leech from a geopolymer, so alternatives would be preferred. Acid catalysts and basic catalysts are both possible, however[89]. Thus, the presence of sodium hydroxide already present within the geopolymer slurry should be sufficient. The size of alkane groups on the alkoxide is negatively correlated with reactivity[79]. Additionally, water content and the presence of other solvents play a role in controlling the rate of reaction, with at least some water required to form any cross-linkages[90]. Finally, the reaction can be driven by heating to 140 ºC[91] or even by ultraviolet radiation[92].

2.4.2. Applications

There are several related uses of functional alkoxysilanes. The most obvious is as an adhesive bridge between organic materials and silicates, as mentioned above. The others depend on altering the surface properties of a silica or other monolith. Such changes can include producing a protective coating[93], creating reflective or anti-reflective coatings[94], manipulating the electric double layer or otherwise modifying dispersion[95], templating a pore structure[96] and altering the surface energy of the compound[97]. The latter three effects are of most interest in geopolymeric research.

In particular, xerogel formulations[98] often make use of an alkoxysilane or other silane coupling agent to improve drying characteristics and limit damage from capillary forces. This

blocking agent tends to have a non-functional short alkane group such as a methyl or aryl attached directly to the silicon. The degree of alkoxide functionality controls the morphology of the resulting surface by controlling the amount of crosslinking. Such mono-, di-, or tri-functional alkoxysilanes can be incorporated into an existing sol gel synthesis[99] or added in some subsequent step[98]. Alkoxysilanes can also be polycondensated alone to create a silicone polymer with only alcohol byproducts.

2.5. Emulsions

One system in which the surface energy alteration potential of alkoxysilanes would be useful is within the geopolymer slurry itself. The ability to use the geopolymer slurry as the hydrophilic phase of an emulsion has not been previously investigated. Emulsions are a system in which a non-dissolving liquid is suspended in another liquid as a secondary phase. The size and distribution of these liquid droplets is governed by well-understood principles of interfacial physics, particularly that the creation of the emulsion from two discrete phases involves the creation of extensive amounts of interface. Any interface must store more free energy than a comparable mass of the bulk phase, or the entropy of mixing would prevent the creation of a separate phase.

It is possible to use a surfactant to reduce the free energy of an emulsion. This is done by bridging the two phases with a phase amenable to both, so that two low-energy interfaces replace one very high energy interface. Both the droplet size distribution[100,101,102] and morphology[101,102,103] are heavily influenced by the choice of this bridging phase or surfactant, and in particular, its molecular structure and geometry. Surfactants possess both hydrophilic (head) and hydrophobic (tail) parts of the surfactant molecule. By altering the geometry of the

head and tail parts of these molecules, various organized micelle structures such as sheets, bilayers, spheres and even bicontinuous phases can be formed[101]. It is further necessary to match the selection of the surfactant to the selection of the two bulk phases. Additionally, as temperature and other environmental considerations can affect the functioning of the surfactant, it is obvious that correct choice of surfactant for a particular system is a difficult problem.

2.5.1. Hydrophobic Phase

For a geopolymer, the necessity of water and the hydrophilicity of the aluminosilicate gel suggest that the geopolymer slurry itself be the primary phase, necessitating a hydrophobic liquid as the second phase. There are innumerable possibilities for the hydrophobic phase. To make a template for porosity, there are two factors of importance: interfacial energy minimization for emulsion stability, and control of removal of the emulsion after geopolymer gelation. A simple but effective method is to drain the second phase after curing if damage to the sample caused by capillary forces can be prevented. Thus, these two factors are both addressed by minimizing the interfacial energy of the phases through an appropriate surfactant. Emulsion stability can also depend on the choice of phase due to Oswald ripening, but is generally a modest effect compared to interfacial energy-driven coalescence and coagulation[104].

The straightforward nature of short-chain alkanes made them a natural choice for this investigation. For any such hydrocarbon, increasing chain length implies a higher surface energy at ambient conditions[105], as well as a higher viscosity, boiling point and melting point. Exacting choices can be made between these for various engineering applications, but the length dependence on surface energy is not large.

2.5.2. Ionic and Non-ionic Surfactants

To a good approximation, surfactant properties depend on the sizes of the hydrophobic and hydrophilic molecule ends, the emulsion temperature, and choice of emulsion phases. In return, emulsion properties are heavily modified by concentration of the surfactant. Due to the vast quantity of surfactants possible, engineers have simplified them into categories based on these traits.

For temperature dependence, the "fish diagram" (Figure 2.1) represents the constant water-oil ratio section of the water-oil-surfactant phase diagram[106]. For nonionic surfactants, increasing temperature results in increased hydrophobic character of the surfactant. For ionic surfactants, the rule is reversed[101]. For all effective surfactants, there is a target temperature range in which an emulsion can be made, and that range depends on both water-oil ratio and surfactant concentration.

Consequently, a straightforward categorization of surfactants is required. The hydrophilic-lipophilic balance number (HLB) is a typical characterization. This characterization considers the ratio of the mass of the hydrophilic region to the mass of the entire molecule, normalized by a factor of 20 [107]. Thus, increasingly hydrophilic molecules have higher numbers up to a maximum of 20 for a wholly hydrophilic molecule. Later modifications[108] considered the comparative strength of various groups by weighting them by a weight W:

$$HLB = 7 - (0.475) * N_l + \sum_{groups} \mathrm{W}_{\mathrm{group}} \tag{2.4}$$

In Equation 2.4, N_l is the number of monocarbon lipophilic groups (CH_x) and the other weights are derived from coalescence rates[108,109,110]. Using this equation and the accompanying group weights, it is possible to calculate values for the surfactants of interest in this investigation.

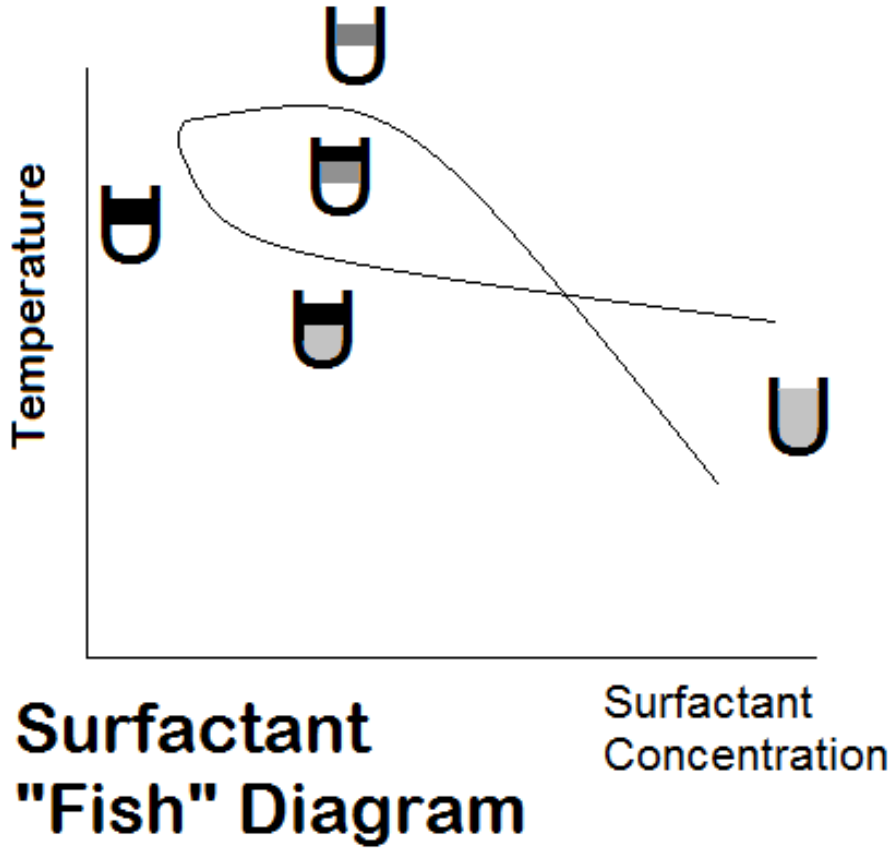

Figure 2.1. The surfactant fish diagram, illustrating temperature and concentration dependence for a non-ionic surfactant emulsion in water and oil. The superimposed beakers provide a visual image of the emulsion at various points on the diagram, where white represents water, black an oil and grey the emulsified mixture. For intermediate concentrations, changing temperature while holding non-ionic surfactant concentration constant results in a pair of phase transitions.

2.5.3. Functional Alkoxysilanes as Surfactants

Using the HLB number for functional alkoxysilanes produces only an estimation of the surfactant's performance due to the resulting silicone polymer phase[111]. Instead, hydrophilic groups, lipophilic groups and silicone groups that are neither are all considered in the "3-D HLB" system. According to that methodology, separate HLB numbers are generated for silicone/oil emulsions and silicone/water emulsions, using the masses of the regions as described

above[111]. The weighting modifications do not appear to have yet been satisfactorily applied to alkoxysilanes.

From this data, it is clear that functional silanes can be either hydrophobic or amphiphilic. It is important to note that, as these molecules polycondense, they will yield alcohol byproducts that will reduce the 3-D HLB numbers, and at the same time, the silicone portion of the molecules will be immobilized in the covalent network. Thus, the effective HLB numbers can be approximated by those of its functional ligand and the 3-D HLB method might be applicable. The effective HLB numbers of typical surfactants are presented in Table 2.1, and calculated results from some of the more useful additives discussed in later chapters are presented in Table 2.2. The MEMO surfactant appears quite amphiphilic by this analysis, while the amine-functional surfactants appear more hydrophilic by this measure. The silicone precursor DIDE contains no hydrophilic material after reaction and is thus assigned an HLB of 0. The exact surfactant properties of these materials do not appear to have been previously investigated.

Table 2.1. Calculated Hydrophilic/Lipophilic Balance Numbers for Typical Surfactants

Surfactant	HLB Number
Cetyltrimethylammonium chloride (CTAC)	22.1
Tetraethylene glycol lauryl ether ($C_{12}E_{4)}$	2.6
Tricosethylene glycol lauryl ether ($C_{12}E_{23}$)	8.9

2.6. Percolating Networks

For isotropic porosity systems and rigid pore walls, geometry dictates a maximum possible closed pore volume percentage as roughly 74%. In polymer foams, the presence of a blowing agent allows for much higher closed porosities as the individual pores can expand to fill

space without failure of the pore walls. Consequently, to exceed this porosity in a ceramic, it is necessary to utilize an open network.

Table 2.2. Calculated Hydrophilic/Lipophilic Balance Numbers for Silane Coupling and Blocking Agents

Surfactant	Silicone/Water HLB	Silicone/Oil HLB	Estimated Ligand HLB
Methacryloxypropyltrimethoxysilane (MEMO)	7.5	10.2	7.0
Phenylaminopropyltrimethoxysilane (PAMS)	4.9	12.9	13.3
Aminopropyltrimethoxysilane (AMS)	7.0	9.8	15.0
Dimethdiethoxysilane (DIDE)	4.3	7.8	0
Note: The estimated ligand HLB considers the silane head group immobilized within the matrix, leaving only the ligand to contribute to surface properties.			

Due to the value of open network solids in a vast array of applications, the physics of such materials are extremely well understood. For the purposes of characterization, full flow through the material is preferable, but will increase the thermal conductivity properties of the material because of convection effects. However, it turns out that the critical porosity required for an open material allowing flow across an infinite distance (a percolating network) is merely a function of geometry and has been found by both Monte Carlo simulation[112,113] and practical experiment[113] to fall in the range of only about 16-18 vol% of pores for cementitious materials. This suggests that for a highly porous random network, the system will always be open or at least percolating.

Previous research on metakaolin geopolymers using mercury intrusion porosimetry[114] (MIP) and octane intrusion[11,55] suggested that porosity approaches 40 vol%. Other previous investigations of geopolymer porosity have used primarily nitrogen adsorption[14], reporting

porosities on the order of 0.1 cc/g, roughly equivalent to about 7% porosity. For traditional cements, the difference in porosity observed by gas adsorption and MIP was related to pore sizes larger than the range of the gas adsorption technique[115].

The other major anomaly possible in these measurements is an incompletely percolating network. In this case, it is very difficult to determine the total porosity of a combination of open and closed pores, and one method to do so involves considering samples of various sizes[116]. For a highly porous geopolymer, closed porosity is not expected to be an issue. For a minimally porous geopolymer, closed porosity does represent a problem, but it is a problem that can be mitigated by estimation of the density of a hypothetical fully dense geopolymer. Using these tools, it should be possible to estimate the total porosity of the entire continuum from a minimally dense geopolymer to a highly porous one.

CHAPTER 3

ALKOXYSILANE INTERACTION WITH GEOPOLYMER

This chapter is partially comprised of previously published material[*].

3.1. Background Information

The ability to cure geopolymers under ambient conditions offers a valuable application in the creation of ceramic coatings on polymer substrates. In particular, geopolymers could be an obvious choice as an adhesive or protective coating for polymers in high-temperature applications, especially those where application of an intermediate epoxy or other adhesive layer is impractical. A previous investigation[42] demonstrated conclusively the possibility of creating strong adhesive geopolymer-ceramic bonds and geopolymer-steel bonds, but generally only minimal adhesive strength is observed between geopolymer and an organic substrate. It is necessary to establish the adhesive interaction between alkoxysilanes and geopolymers, and considering this problem is a practical way of doing so. Before addressing this possibility, it is useful to examine other mechanisms of adhesion between organics and geopolymers as well.

Wet geopolymer slurries adhere strongly to some polymers, including polystyrene, due to partial wetting. This adhesive force is eliminated due to the increasing of surface tension with solidification, but during early stages of geopolymer precipitation the material is both mobile enough and proximate enough to allow for dispersive adhesion. Thus, mechanical interlocking is not in principle required. The simplest method of enhancing adhesion is to increase wetting and

[*] B. E. Glad, C. Han, and W. M. Kriven, "Polymer Adhesion to Geopolymer Via Silane Coupling Agent Additives," J. Am. Ceram. Soc., 95[12] 3758-62 (2012).

polar dispersive forces through the addition of a surfactant or other wetting agent that permanently reduces the surface energy of the resulting geopolymer.

For this to be practical, liquid must be permanently entrapped at the interface between the geopolymer and the substrate. Mass measurements imply that excess water migrates to the surface of the geopolymer during the latter stages of geopolymer curing. This is most obviously observed in a molded geopolymer, which is often able to easily slip from a polymer mold due to the lubricating effect of the liquid interface. Obviously adhesion from this water is not capable of promoting adhesion due to its freedom of movement, suggesting that entrapped polar material would be more effective.

Expected to be far more effective is another traditional method of promoting adhesion. Typically, adhering amorphous silicates such as glasses to polymer consists of treating the ceramic surface with coupling agents (also called "sizing agents") consisting of an organic functional group covalently bonded to a tri- or dihalosilane, or to various tri- or dialkoxysilanes. These materials, as well as their adhesion to glass and other substrates, is well known and extensively described by Plueddemann[79]. Coupling agents are generally considered to create a successful bond between a silicate and polymer through a combination of covalent and noncovalent forces, and in particular are known to react readily with silanol. For this application, alkoxysilanes were used rather than halosilanes because hydrolysis of the halosilanes would result in production of a strong acid, which would yield alkali halide salt precipitates in the basic solution. The effects of such precipitates has been previously investigated and found to decrease durability in geopolymers unless extremely small quantities of water are used, which would result in decreased strength[81].

Both of these methods are considered and evaluated against a selection of substrates. It was found to be possible to synthesize adhesive geopolymeric material with bonding strong enough for a variety of real-world purposes, with almost no modification of processing time or conditions.

3.2. Adhesion Test Design and Procedures

The values of many mechanical properties can be legitimately observed using a variety of different tests, described in numerous different geometries. In contrast, measured adhesive strength, is highly variable depending on geometry, because adhesive failure depends on a complex interaction of local delamination, highly asymmetric stress distributions, surface asperities and imperfections. Consequently, it is valuable from both a scientific perspective and practical materials design considerations to evaluate adhesion using multiple geometries. This is especially true when cohesive failure of the adhesive or the substrate is the dominant form of adhesive failure. Various formal tests that were conducted are described below.

In many cases, very low adhesion is observed, making sample handling difficult and formal quantitative measurement impossible. In those cases, a lack of effective adhesion is simply reported instead. Samples which delaminated due to procedural miscues were not factored into the results.

3.2.1. Synthesis

Metakaolin (MetaMax HRM, 3.6 μm median particle size[117], BASF Corp., Florham Park, NJ) was used as received. An aqueous sodium silicate solution (waterglass, $Na_2O{\bullet}2SiO_2{\bullet}11H_2O$) was prepared from fumed silica (Cab-o-sil LM-150D, Cabot Corp., Boston,

MA), sodium hydroxide granules (Fisher Scientific Co. L.L.C., Waltham, MA) and deionized water. The solution was stirred for 24 hours to allow for full dissolution of the silica, and then aged for at least 2 weeks at ambient temperature to ensure typical oligomer relative concentrations.

Adhesive additives were added dropwise to 11.1 g batches of metakaolin, and the result mixture was combined with either 19.0 g (Formulation A, see Appendix) or 18.5 g (Formulation B) waterglass. Adhesive additives consisted of the silane coupling agents N-phenylaminopropyltrimethoxysilane (PAMS), methacryloxypropyltrimethoxysilane (MEMO) and/or aminopropyltrimethoxysilane (AMS) (all Gelest, Inc., Morrisville, PA), and these coupling agents were used as received.

High-impact polystyrene (HIPS) sheet (U.S. Plastic Corp., Lima, OH) and polystyrene foam (Styrofoam Ag board, bulk density=0.03 g/cm^3, Dow Chemical Corp., Midland, MI) were used as substrates.

3.2.2. ASTM Tensile Adhesion Test

Tensile adhesion of geopolymer (Formulation A2) to polystyrene foam was investigated using the ASTM E736 test, since one possible use of an adhesive geopolymer is as a fireproof polymer coating in building insulation. To conduct this test under controlled conditions, a customized apparatus was developed, as illustrated in Figures 3.1 and 3.2.

A standard test sample for this method requires a 30 cm x 30 cm x 1.25 cm sample of both coating and substrate, which requires the synthesis of approximately 1.6 kg of geopolymer (for a geopolymer with a bulk density of about 1.4 g/cc). However, the available laboratory synthesis methods allow a maximum mass of roughly 200 g per slurry batch. It was also

observed that a foam substrate of that size would experience considerable deformation, reducing the accuracy of the test. Thus the sample size was reduced to 10 cm x 10 cm x 1.25 cm, which proved to be satisfactory. The metal adhesive cup was a cylinder 6.67 cm diameter and adhered directly to the geopolymer surfacing using the EpoxiCure system (Buehler, Lake Bluff, IL) and the appropriate hardener.

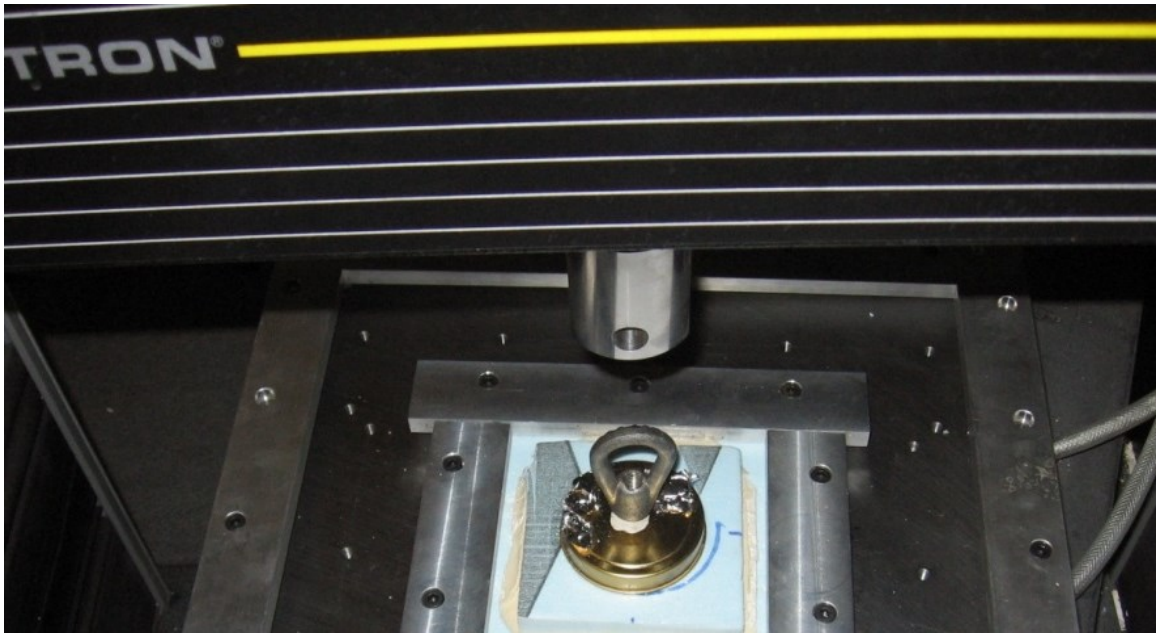

Figure 3.1. A sample loaded into the custom ASTM E736 fixture. The length of a side of the plate is 40 cm, allowing for the loading of a 30x30 cm sample.

3.2.3. ASTM Double-lap Shear Adhesion Test

Adhesion of geopolymer (Formulation A) to HIPS was measured using ASTM D3527 (a double-lap shear test) at standard laboratory humidity and temperatures of 27 ± 1 °C. The inherent flexibility of HIPS sheets meant that the panel cutting prescribed was likely to place the adhesive under tension, so the sheets were cut to the specified testing width prior to curing the geopolymer, as defined in a permitted modification of the standard. As a result, some deviation

from the prescribed 0.1 mm precision of the lap sizes occurred due to slippage and normal handling. Instead, the lap sizes were carefully measured to the nearest 0.1 mm length and width after the test, and the reported values are the observed force normalized by the true total lap area. Tests were conducted at 3 days and 15 days after initial curing was initiated. Samples were cured sealed at 25 °C unless otherwise specified.

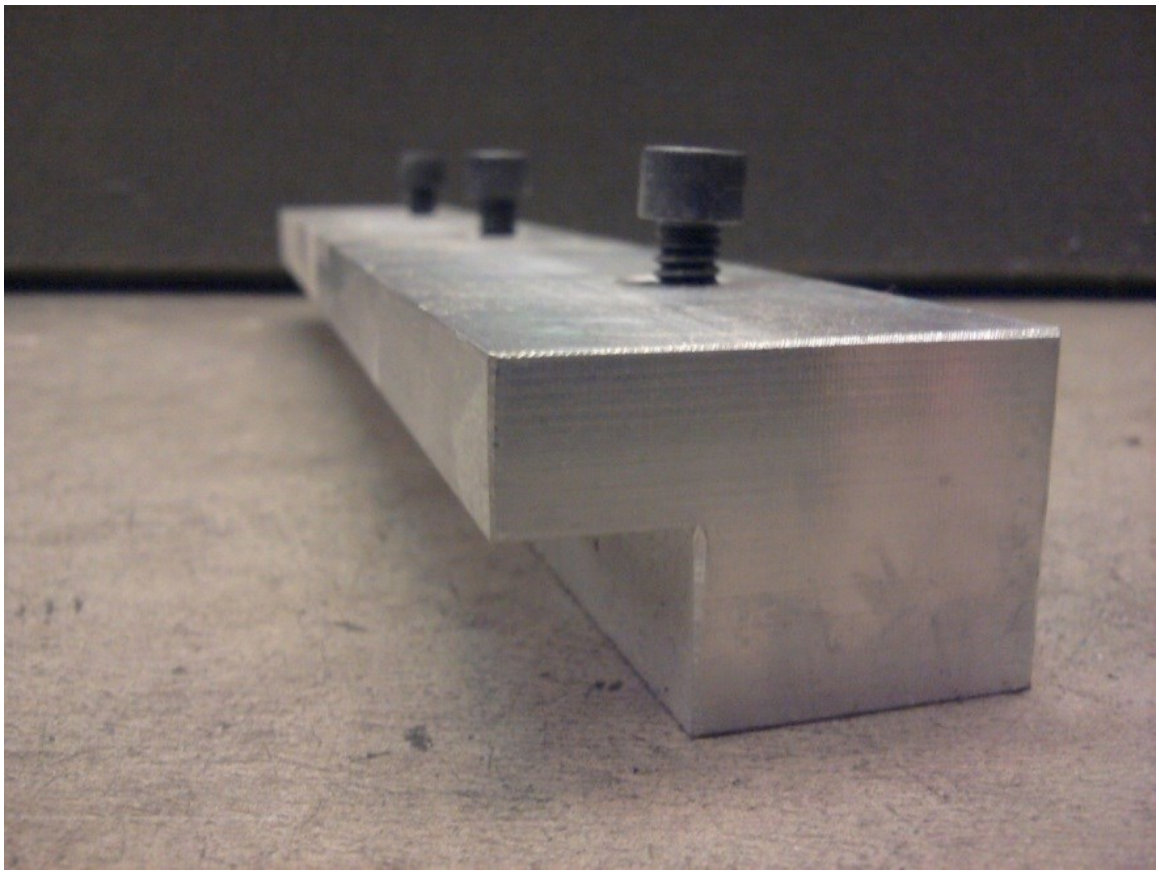

Figure 3.2. A side view of the custom ASTM E 736 fixture, illustrating the nominal 2.5 cm width overlap used to clamp the polystyrene foam board flat against the load exerted upwards on the specimen.

3.2.4. Polymer Foam Sandwich Test

Adhesion of some organically-modified geopolymer (Formulation B) to polystyrene foam caused failure of the foam from shear prior to debonding, so additional tensile tests were conducted. Each sample for these tests consisted of two 50x50 mm squares of foam, each with a thickness of 25 mm, bonded by the geopolymer, and adhered securely to a tensile tester using a commercial polystyrene-steel bonding agent. The samples were allowed to rest sealed at ambient conditions for more than one month to provide a good estimate of final adhesive strength in a practical application.

3.3. Other Characterization

Cu-Kα X-ray powder diffraction (XRD) testing was conducted with a Seimens-Bruker D5000 diffractometer. Tests were conducted at 40 kV, 30 mA, a step size of 0.02° 2-theta, and a measurement time of 4 seconds/step. Scanning electron microscopy (SEM) micrographs were captured using a JEOL 6060 scanning electron microscope with specified excitation energies. Diffusion reflection infrared spectra were taken using a Nicolet Nexus 670 spectrometer on powdered samples mixed with KCl (1:19 wt ratio). Powder samples of adhesive were generated by dry grinding in an alumina mortar, and were collected after being passed through a 44 μm mesh.

Diametral compression strength testing of these samples was conducted according to ASTM D3967 (a Brazil test) at standard laboratory humidity and temperatures of 26 ± 1 °C. The samples were cast in sealed cylindrical poly(tetrafluoroethane) molds of 25.4 mm in diameter, and cut with a diamond-edged wafer blade to a thickness of approximately 8 mm in diameter. At least 10 samples cut from 3 different cylinders were used for each test.

3.4. Results

XRD data such as Figure 3.3 confirmed that the addition of the silanes tested did not alter formation of the amorphous network or inhibit reactivity. The transition of the amorphous peak from 22-degrees to 28-degrees in the XRD plot is well-known and taken as evidence that the geopolymerization proceeded as expected. Additionally, no evidence of zeolitic formations or other crystalline structures was observed. Anatase, present as an impurity in the metakaolin precursor used, was observed unchanged in the final product.

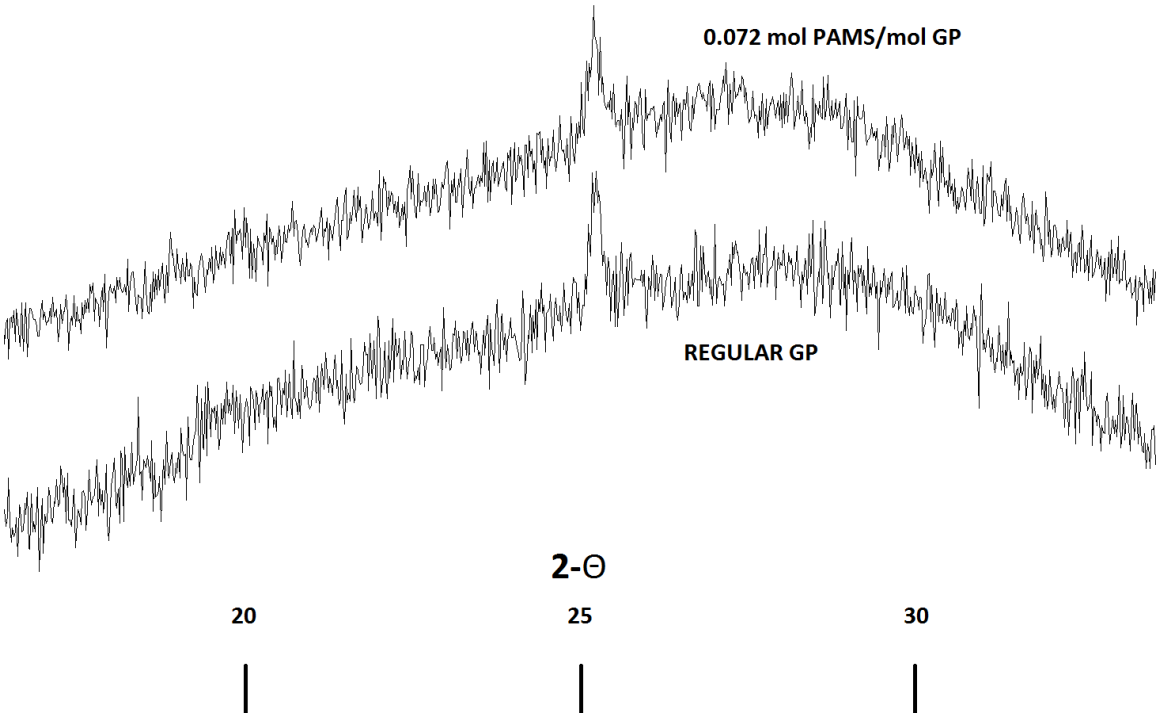

Figure 3.3: X-ray diffraction spectrum of a Formulation B adhesive GP modified with PAMS is qualitatively similar to that of regular Formulation B GP. The hump at ≈28° 2-Θ in indicative of typical geopolymerization. The peak at ≈25.5 2-Θ indicates titania impurities.

3.4.1. Comparison of Adhesion

Testing on the E736 samples was abandoned after further investigation revealed that failure of the polystyrene foam resulted in an inability to reach even 100 kPa tensile adhesion strength (Table 3.1, Figure 3.4). Attempts to conduct statistical analysis using 13 samples of PAMS-modified geopolymer identified a meaningful positive relationship between curing time (measured as time between casting and testing) and tensile adhesion strength. Substantial adhesion remained following exposure of the open side of the 1.3 cm-thick sample (≈1 min) to the unvarying flame of a propane torch.

Table 3.1. Results of Fire-proof Monolith Testing

Sample parameters	Maximum adhesion
0.072 mol PAMS/mol GP, cured 20 days	0.091 MPa
0.024 mol PAMS/mol GP, cured 29 days	0.065 MPa

Adhesion testing results for the double-lap shear tests (Table 3.2) indicated that the addition of coupling agents to geopolymer offers advantages for adhesion to polymer sheets. It appears that the low strength of unreinforced geopolymer was the limiting factor for the observed adhesive strength. It was observed in every case that the 80-mm adhesive laps demonstrated far less adhesive strength than did the 8-mm laps for identical Formulations of adhesive, providing evidence that failure occurs due to high stresses propagating from areas with adhesive or structural imperfections.

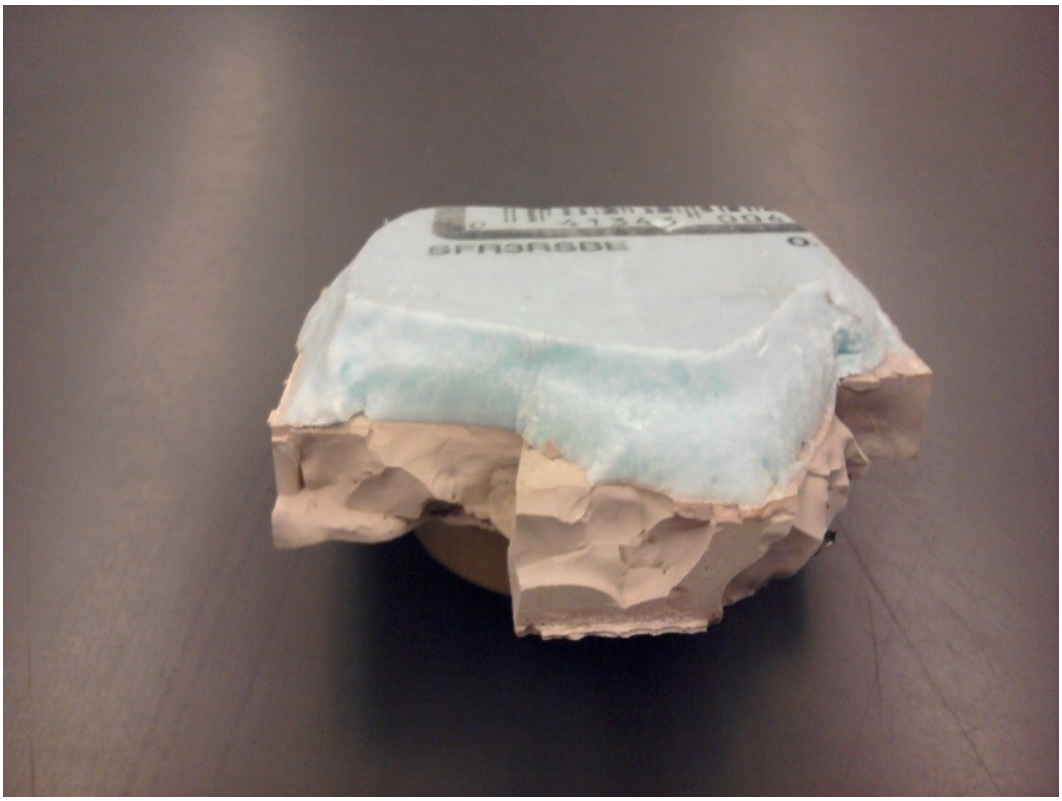

Figure 3.4. An optical photograph of 0.072 mol PAMS/mol GP 25 °C (Formulation A2) cured adhesive (bottom) attached to polystyrene foam (top). The adhesive remained bound to the polystyrene foam after a tensile adhesion test (ASTM E736 with reduced sample size), as the polystyrene foam has failed before the coating delaminated. The width of the sample in the image was 10 cm.

Table 3.2. Comparison of Coupling Agent Additives

Alkoxysilane Additive (0.072 mol/mol GP)	Double-lap adhesive strength (MPa)		
	80 mm lap, 3 days	10 mm lap, 3 days	10 mm lap, 15 days
None	0.06 ± 0.009	0.06 ± 0.015	--
MEMO	0.08 ± 0.015	0.28 ± 0.028	0.05 ± 0.004
AMS	0.10 ± 0.007	0.59 ± 0.12	0.12 ± 0.032
PAMS	0.09 ± 0.030	0.52 ± 0.10	0.10 ± 0.037
PAMS, 50 °C 1-day cure	--	0.06 ± 0.013	0.10 ± 0.040

Brittle failure of the geopolymer prior to or concurrent with delamination was observed in nearly every lap test using AMS or PAMS adhesive geopolymers, and a reticulated network of

cracks was visible in SEM micrographs of the geopolymer surfaces after failure (Figure 3.5). Both of these modifiers proved to greatly improve adhesive strength as compared to both the unmodified control and the MEMO-modified geopolymer. Results are presented in Table 3.2. Not included in Table 3.2 are the results of several similar coupling agents (including glycidoxy, isocyanate, vinyl, and non-functionalized silane coupling agents), or ionic or non-ionic surfactants, each of which demonstrated too little adhesion to be useful or easily measured by the apparatus.

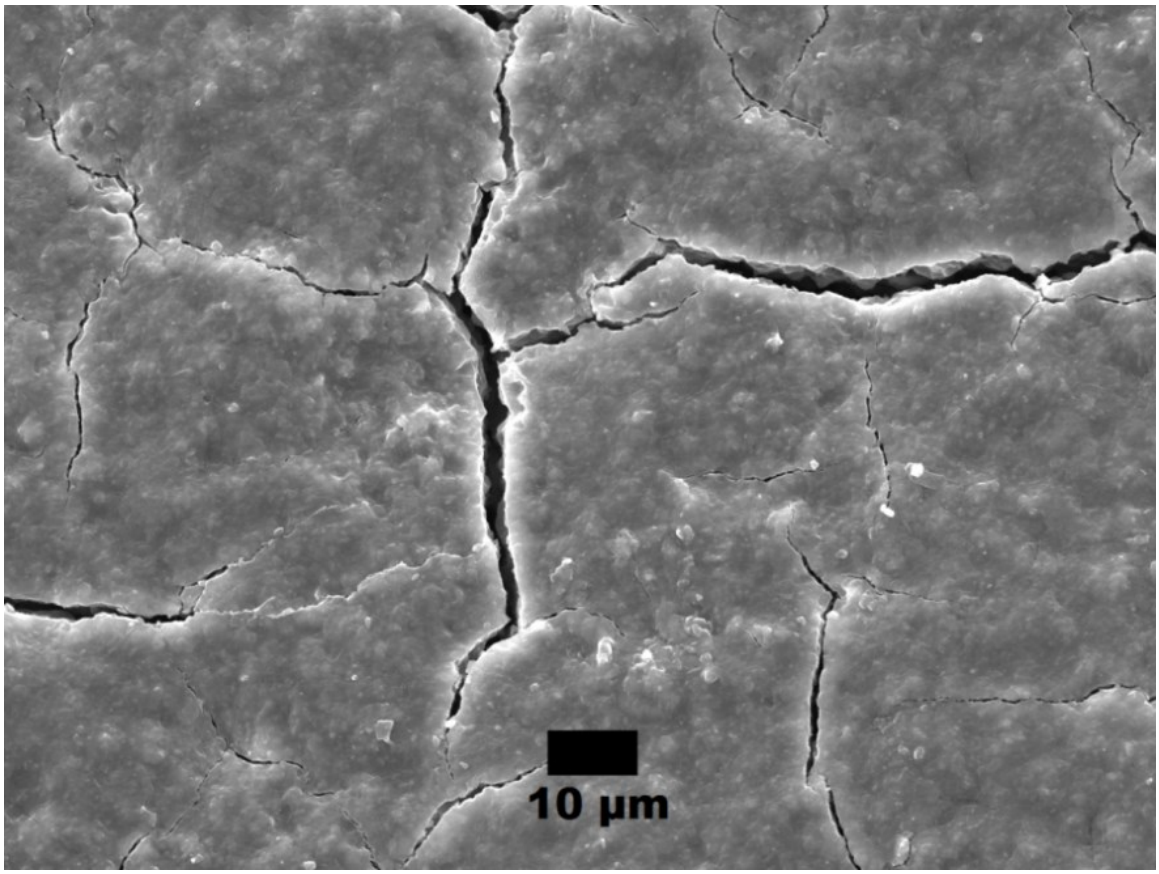

Figure 3.5: A scanning electron micrograph (25 kV excitation energy) of a 0.072 mol PAMS/mol GP 25 °C (Formulation A) cured adhesive. A reticulated network of cracks is visible after cohesive failure in a double-lap shear test. This adhesive did not demonstrate such a crack network prior to the test.

Results for tensile sandwich adhesion to expanded polystyrene foam are shown in Table 3.3. The foams were found to have experienced linear shrinkage of approximately 1% after the curing in contact with the adhesive geopolymer. This suggests that the failure at relatively low strengths observed in the double-lap tests was a result of drying shrinkage observed in the geopolymer that created tremendous stresses on the adhesive bonds at the interface. For the laps, stress was maintained, but for the foams, the foam itself yielded in preference to debonding. Clearly, adhesion to polystyrene foam using an aniline-functional coupling agent is superior to an amine-functional coupling agent once cohesive and drying-related failures are mitigated.

Table 3.3. Results of Foam Tensile Adhesion Tests

Tensile Adhesion Strength (MPa)		Curing Temperature (24 hours)	
		Ambient	50 °C
Sample additive (18 g/mol GP)	PAMS	0.340 ± 0.0245	0.266 ± 0.0518
	AMS	0.0503 ± 0.0182	0.0352 ± 0.0332

The time-dependent results of adhesion are presented in Figure 3.6 as well as Tables 3.1 and 3.2. It is clear that the adhesion observed is much stronger before long-term curing and drying have taken place. Based on the foam results, it seems likely that this decrease in strength is due to drying shrinkage of the geopolymer. However, improved results with increasing amounts of coupling agent begin to occur as drying time increases. If adhesive failure is a result of local cohesive failure of the adhesive, then clearly strength increases more slowly for the geopolymer with increased amount of additive.

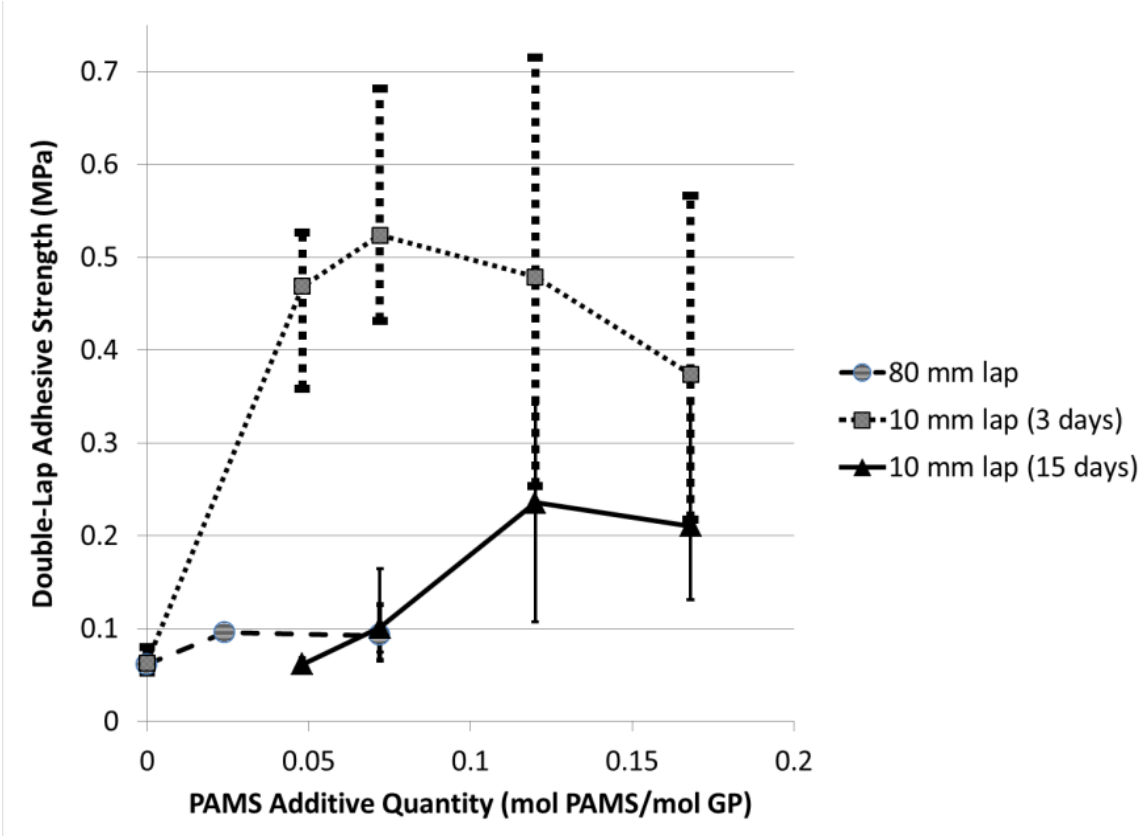

Figure 3.6. The relationship of additive quantity versus adhesion strength as measured by double-lap shear tests. Error bars indicate the maximum and minimum adhesion strengths measured.

3.4.2. Mechanical Strength

The results of diametral compression data are presented in Table 3.4. Unfortunately, the adhesive benefits of PAMS were accompanied by a loss of strength. This loss of strength was mitigated by curing at ambient temperature rather than elevated temperature. The Weibull modulus (calculated using median ranks) of the adhesive was much higher, indicating a more reliable failure mode and more uniform flaw distribution in the sample. This observation is suggestive of a more polymeric character, which is consistent with the addition of the organic

material to the matrix. The Weibull scale factor (also known as characteristic life) estimates the stress required to cause approximately 63.2% of the samples to fail.

Table 3.4. Comparison of Diametral Compressive Strength of Modified and Unmodified Geopolymer

Sample type	Splitting Strength (MPa)	Weibull Scale Factor (MPa), Modulus
GP	4.00 ± 1.76	4.53, 2.52
GP with .072 mol PAMS/mol, 50 °C	2.46 ± 0.53	2.68, 4.94
GP with .072 mol PAMS/mol, ambient	3.20 ± 0.74	3.49, 4.72

3.5. Discussion

Through a control geopolymer-modified geopolymer difference method, FTIR data (Figure 3.7) allowed for the identification of distinctive PAMS peaks noted in the literature[118] even at concentrations of 0.072 mol PAMS/mol geopolymer. The presences of an aromatic group (multiple stretching bands from approximately 1400-1500 cm^{-1}), aromatic and aliphatic C-N stretches (1322 and 1255 cm^{-1}, respectively), and an alkane C-H bend (1466 cm^{-1}) were confirmed, as expected for the molecule. Also matching the reference sample over the range 800 cm^{-1} to 1650 cm^{-1} were distinctive peaks at 811 cm^{-1} and 1600 cm^{-1}.

A peak at 3745 cm^{-1} is characteristic of free, isolated silanol[119] but appears only with the addition of PAMS. This may be indicative of the slightly higher ratio of Si:Al in the modified geopolymer (due to the silane component of PAMS), or it may indicate that the addition of the silane somehow causes the formation of small amounts of free silanol within the geopolymer. This peak is very sharp, and distinct from the hydrogen-bonded O-H stretch (observed as a broad peak in the vicinity of 3400 cm^{-1}, as expected due to the presence of water, Si-OH and related

species) clearly evident in both the PAMS geopolymer and the control. This seems to indicate relatively little covalent interaction between the adhesive and the geopolymer, but the adhesion remained strong even after multiple years.

It is possible to attribute this time dependence to the effect of methanol byproducts of the coupling agent condensation reaction with silanol, in light of the known retarding effects of alcohols on the geopolymerization reaction[83]. This effect is in contrast to an overall weakening of the system brought about by the addition of 3-coordinated network modifiers, as the cohesive effects of such weakening should be approximately constant over time. The system was sealed during the entire drying period, so loss of coupling agent from the system should not be an appreciable factor. There was no meaningful difference observed in the microstructures of 50 °C versus 25 °C cured PAMS geopolymers far away from the adhesive interface (Figure 3.8).

Notably, for both adhesives a large proportion of the available interface area is instead occupied by pores, as seen in Figure 3.8. These large pores were not observed in the geopolymers adhered to the HIPS sheets. Because of the irregular distribution of the pores over the interface surface, it is not likely that the pores are the result of templating by the foam, especially as extruded polystyrene foam does not have features on that length scale. Instead, it is likely that the presence of water at the interface causes such porosity. It is possible that a reduction in water could thus improve adhesion to foams. That may require a change in precursors from metakaolin to fly ash, where a lower water ratio is typical[7].

Clearly, the necessary route to improved adhesion is through improved cohesive strength rather than stronger adhesive characteristics. Strength improvement has been a central focus for geopolymer research for quite some time and a tremendous variety of references exist on this topic, and has been well-summarized previously[5].

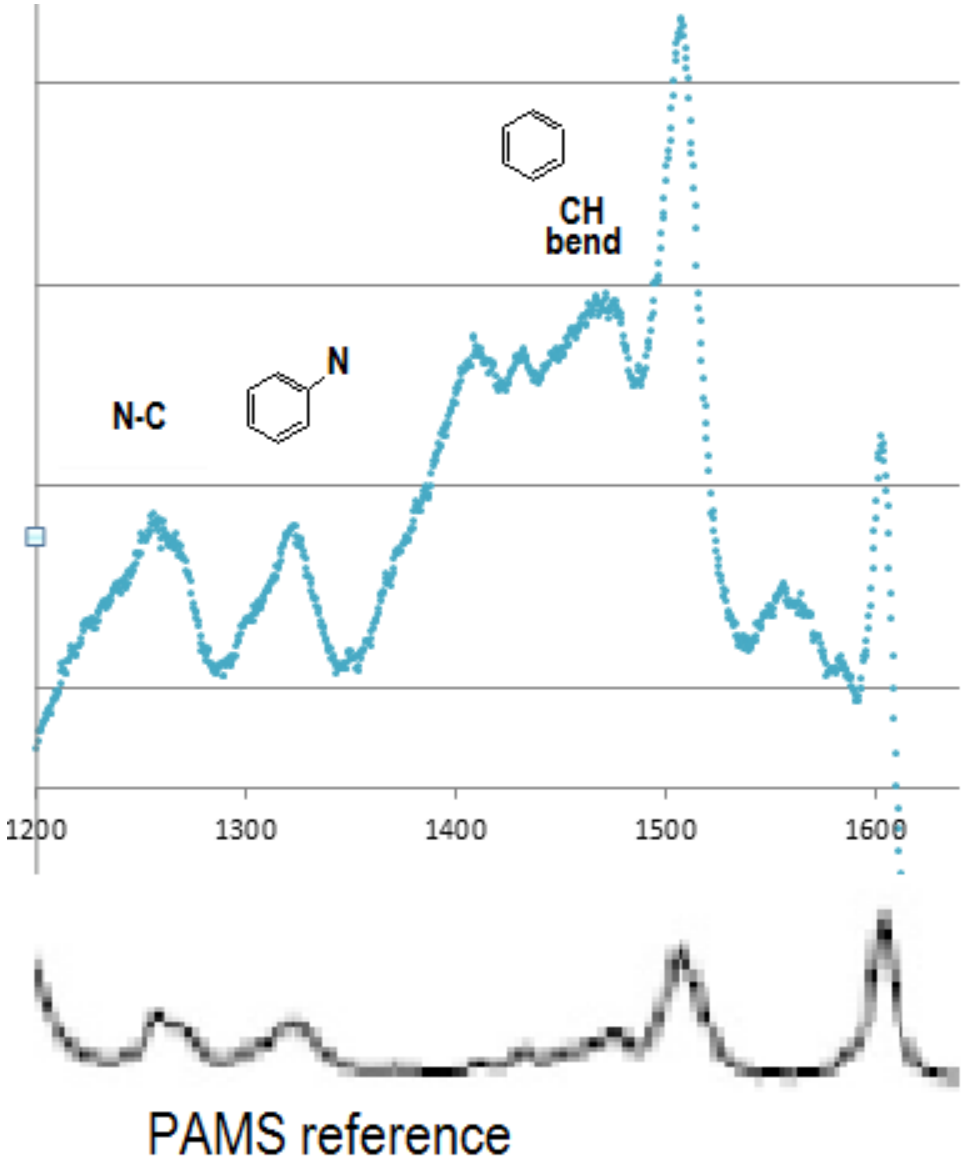

Figure 3.7. A comparison of a portion of the spectrum representing the difference between an FTIR spectrum of Formulation A geopolymer modified with 0.072 mol/mol PAMS and an unmodified one. Comparison to a reference[118] suggests that the PAMS functional group remains largely unchanged.

That being said, the incorporation of silane coupling agents into the geopolymer slurry was successful and resulted in modification of mechanical and adhesive properties. The additives resulted in reduced mechanical strength but an increased Weibull modulus. Double-lap

tests and tensile adhesion tests identified drying shrinkage and thermal expansion mismatch were identified as the major obstacles to adhesion, which were found to be mitigated by the easy yielding of polystyrene foam. Considerable variation of results occurred based upon choice of organic functional group, with aniline functional groups proving superior to amine, methacrylate and other functional groups. There was little evidence that the coupling agents provided large microstructural modification, but further microstructural analysis is required.

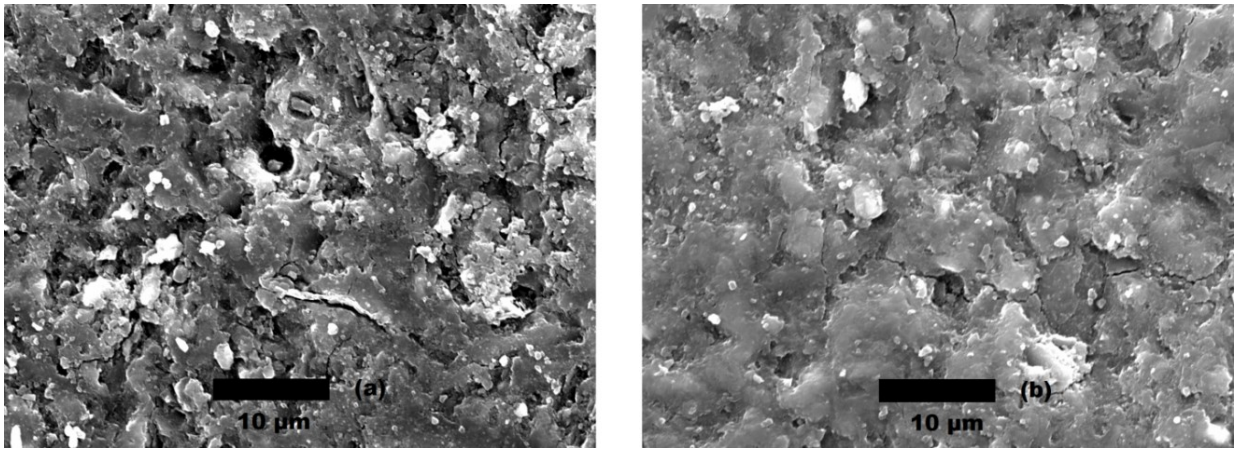

Figure 3.8. Scanning electron micrographs (20 kV excitation energy), illustrating a comparison of bulk 0.072 mol PAMS/mol geopolymers cured at 25 °C (a) versus 50 °C (b). Microstructure alone provides little indication of greatly differing adhesive properties.

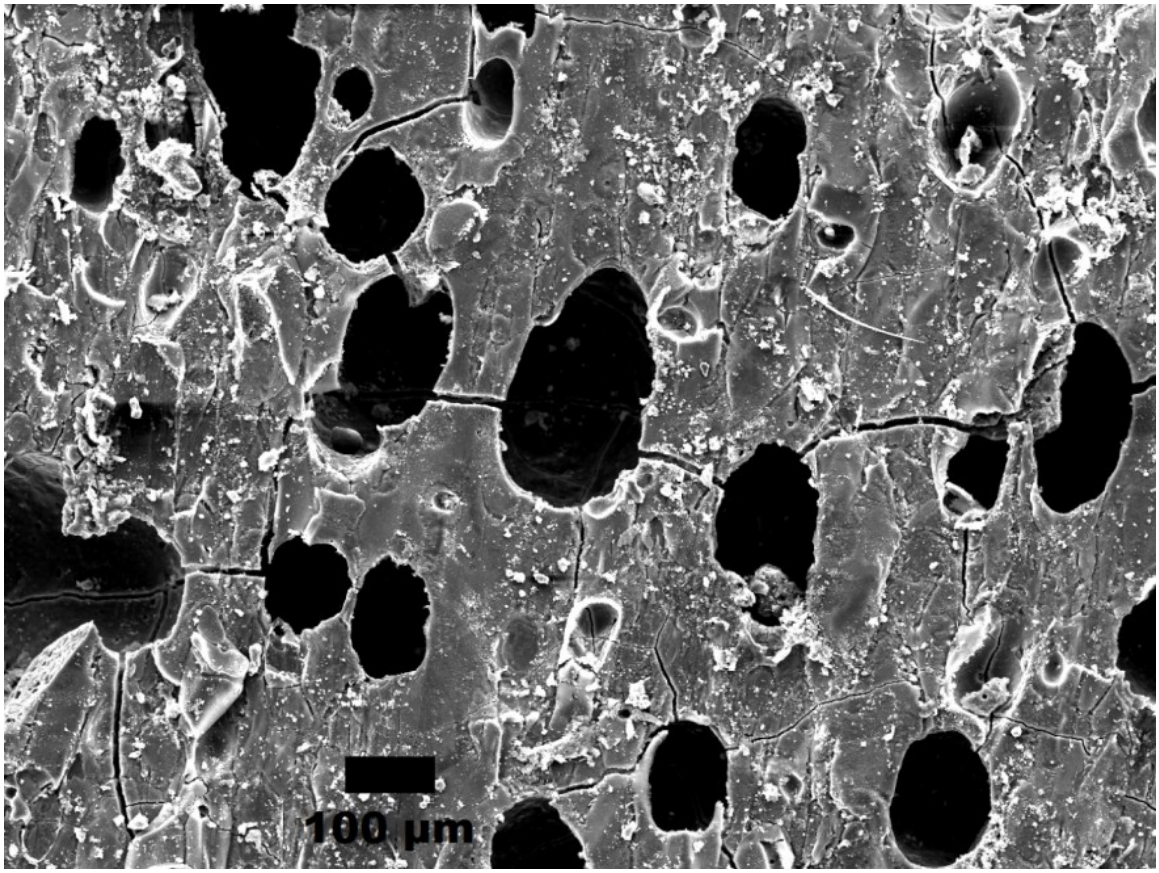

Figure 3.9. A scanning electron micrograph (20 kV excitation energy) of macroscale pores in the adhesive at the PAMS GP-PS foam interface. Clearly, these macropores reduce the total interfacial area. They are likely the result of water expelled from the adhesive during drying, and are not observed at the PAMS GP-HIPS interface.

CHAPTER 4

GEOPOLYMER CURING AND DRYING CONDITIONS

This chapter is partially comprised of previously published material[†].

4.1. Background Information

Full or nearly full geopolymerization is necessary for a sufficient sample. It is observed that reactivity is decreased due to the addition of the organic additives, but is it also observed that processing differences greatly influence the microstructure. The evaporative method used to synthesize highly porous geopolymers (Chapter 7) represents a departure from understood processing practice. Thus, it is valuable to consider the effect of these conditions on geopolymerization, and isolate them from the effects of the organic material. This investigation thus considers geopolymer evaporative material alone.

While geopolymer research has been conducted in both relatively humid and relatively arid environments, little to no research has investigated the effects of humidity and water vapor conditions on geopolymerization. Most investigations have used sealed containers or molds in geopolymer preparation, resulting in substantial information on the geopolymerization process at effectively saturated conditions and little otherwise[5,6,7,15].

The effect of water content has been previously investigated under sealed conditions, identifying microstructural changes in porosity[14] and specific surface area[2]. However, for many practical applications, including bulk uses such as construction as well as coatings, a geopolymer

---

[†] B. E. Glad and W. M. Kriven, "Humidity Effects on the Completion of Geopolymerization in Dilute Evaporative Slurries," pp. 25-30. in Developments in Strategic Materials and Computational Design III: Ceramic Engineering and Science Proceedings, Vol. 33, Iss. 10. Edited by W. M. Kriven, A. L. Gyekenyesi, G. Westin, and J. Wang. American Ceramics Society, Daytona Beach, Fl., 2012.

formulation that does not require sealing might provide advantages over the traditional formulations. This investigation intended to determine what sort of changes to processing were required in accounting for this difference, since it was observed that drying geopolymers for extended times leads to failure by cracking and that a minimum amount of water needs to be retained to prevent this failure[2].

It has been known for many years that drying of precipitating silica networks may result in either bulk precipitation or skin growth from the evaporative surface, depending on the condensation rate of the silica formulation[120]. In the case of skinning, the resulting precipitate microstructure would be expected to depend on distance from the free surface, and drying characteristics would be difficult to predict. For bulk precipitation, normal drying kinetics in a system with time-varying porosity might be expected to suffice in describing the system. Due to this ambiguity, an investigation of geopolymer thickness on curing and drying was beyond the scope of this report.

4.2. Experiment Procedures

Sodium silicate solution (waterglass) was prepared as follows: 160.0 g sodium hydroxide (Sigma-Aldrich Co., LLC, St. Louis, MO) was added to 360.0 g DI water in a stainless steel container and stirred using a polytetrafluoroethane stir bar with a magnetic stir plate until fully dissolved. The container was then sealed with polyethylene terephthalate plastic film, and the temperature of the stir plate was set to approximately 45 ºC. A total of 240.0 g fumed silica (Cab-o-sil LM-150D, Cabot Corp., Boston, MA) was then added in small batches of approximately 10 g, each time allowing for complete or almost complete dissolution of the silica before adding the next batch, with the container remaining sealed when not adding silica. After

all silica was added, the container was resealed and the contents were allowed to stir at the elevated temperature for 24 hours. After 24 hours, the solution of sodium silicate was poured into a polyethylene container, and allowed to equilibrate at ambient conditions for at least two weeks. Metakaolin (Metamax EF, median particle size[117] 2.7 μm, Engelhard Corp., Iselin, NJ) was used as received.

Samples were synthesized using 2.78 g metakaolin, 4.75 g waterglass, and additional water (Formulation C and C2, described in Appendix A), as appropriate for the non-premixed samples or the premixed samples. The premixed samples also used 0.51 ± 0.02 g dispersant (Darvan 821A, 40% ammonium polyacrylate in water, R. T. Vanderbilt Co., St. Norwalk, CN) as specified in Formulation C2. Samples without additional water (Formulation B) were used as controls. A sample was taken from each premix slurry after 1, 3 and 7 days, and then diluted and processed according to procedure C2 to 197 moles water/mol geopolymer (a value corresponding to the addition of 40.0 ml water) to create the Formulation C2 premixed geopolymer.

4.3. Characterization

Cu-Kα X-ray powder diffraction (XRD) testing was conducted with a Siemens-Bruker D5000 diffractometer. Tests were conducted at 40 kV, 30 mA, a step size of 0.02° 2-Θ, and a measurement time of 8 seconds/step. Diffuse reflection infrared spectra were taken using a Nicolet Nexus 670 spectrometer on powdered samples mixed with KBr (1:19 wt ratio). Powder samples were generated by dry grinding in an alumina mortar, and were collected after being passed through a 44 μm mesh.

4.4. Analysis of Ambiently Cured Geopolymers

During the porosity investigation, observed qualitative differences between sealed samples and samples cured under low-humidity conditions led to a question as to where precisely curing of the geopolymer ends and drying begins for an unsealed geopolymer. While obviously geopolymerization can be inhibited through dilution, the question of whether evaporation of an excessively dilute geopolymer slurry down to normal synthesis conditions would result in the same or different microstructure as a regularly cured geopolymer had not been investigated. As slurry viscosity is an important consideration, this investigation was conducted in an attempt to minimize slurry viscosity, which would have resulted in more flexibility in experiment design. Instead, a different solid structure was observed, and it was found that the degree of geopolymerization could be carefully controlled by manipulation of the water content at various degrees of the geopolymerization process. This experiment was conducted at 25 ºC and desiccant conditions to both closely simulate geopolymer curing under arid conditions and more clearly identify differences.

4.4.1. Results

It was found that the highly alkaline $18Na_2O•Al_2O_3•4SiO_2•197H_2O$ dilute slurries did not fully evaporate or form a coherent solid. In every other case, monolithic samples eventually formed, but the mechanical properties, microstructure and phase composition of the monoliths varied considerably. All of the monoliths cured under the desiccant conditions experienced cracking failure, as expected. However, because of the massive excess of water used in these slurries, it is unsurprising that maximizing the humidity for even two full days (95% humidity) prior to reducing the humidity to desiccant conditions had no meaningful effect on the results,

but increasing the humidity to 70% and 30% for the duration of curing resulted in a solid monolith with minimal cracking.

As seen in the x-ray diffraction data in Figure 4.1, the characteristic shift of the large geopolymer amorphous hump from metakaolin's ≈22º 2-Θ to ≈28º 2-Θ was not observed in the highly dilute geopolymer slurries. Instead, there is a large amorphous hump at ≈25º 2-Θ and unreacted metakaolin visible at ≈22º 2-Θ. Additionally, the presence of sodium carbonate monohydrate (thermonatrite, $Na_2CO_3 \bullet H_2O$, ICDD No. 04-009-3774) indicates that this phase was formed in parallel to the geopolymer reaction. In every case, the presence of carbonate was associated with an incomplete reaction. The sharp peak at ≈25.2 2-Θ is indicative of anatase (ICDD No. 00-21-1272). That peak appeared in each pattern and is the result of titania impurities in the metakaolin.

Infrared spectroscopy data reflect the same result, as seen in Figure 4.2. In the controls, there is a clearly visible characteristic peak shift of the ≈1080 cm^{-1} Si-O-Si symmetric stretch to a ≈1000 cm^{-1} asymmetric stretch representing the interaction of the Si-O-Si bonds and the Al-O-Si stretch observed at ≈810 cm^{-1} [121]. In the samples produced from highly dilute slurries, such a shift was greatly reduced, and the carbonate peaks at ≈1460 cm^{-1} and ≈2900 cm^{-1} were substantially more prominent.

The premixed samples illustrated incomplete reactions as well, but demonstrated a pronounced difference in reactivity as measured by FTIR peak shift, as shown in Table 4.1. However, these samples produced similar diffraction profiles as the dilute slurries, with the amorphous hump position apparently unchanged. A limited amount of sodium carbonate decahydrate (natron, $Na_2CO_3 \bullet 10H_2O$, ICDD No. 00-037-0451) was also observed in these diffractograms, but only in samples premixed for more than one day.

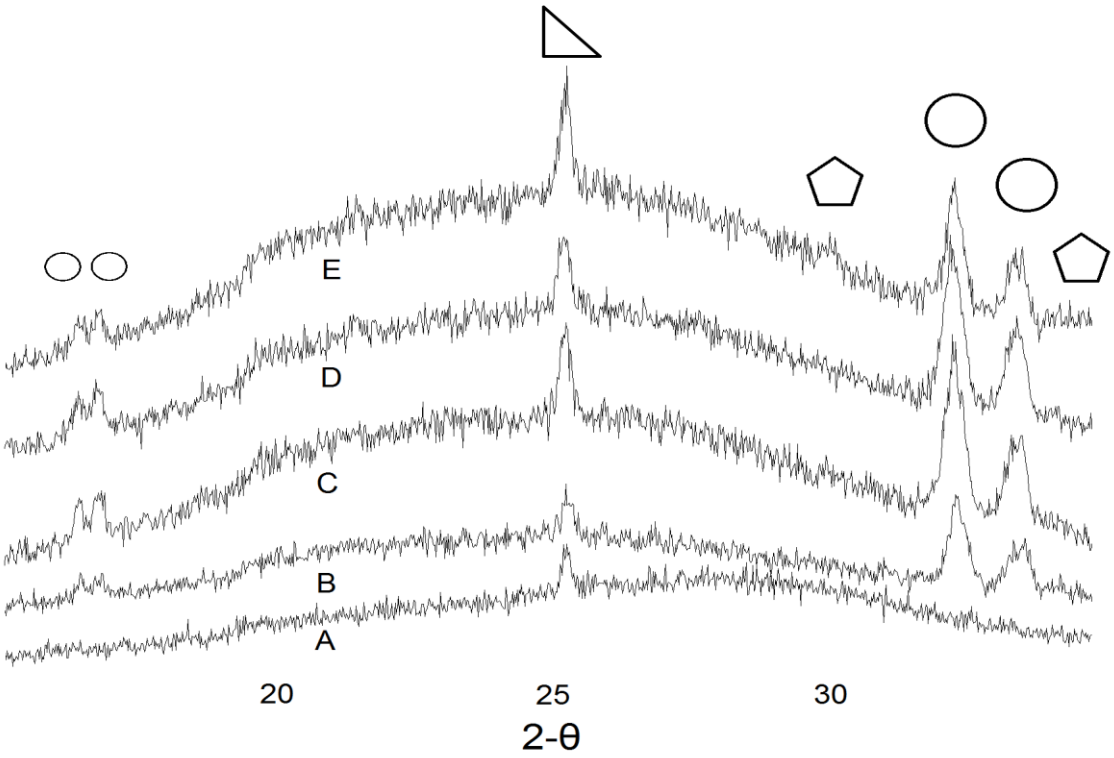

Figure 4.1. X-ray diffraction data of a geopolymer control (1·1·4·11 Formulation B) (A), a dilute slurry without premixing (B), and the results of 18.1 mol water-1 day (C), 22.9 mol water-1 day (D) and 37.4 mol-7 day (E) premixes. Present in all the samples was anatase (TiO_2, triangle). In all the dilute slurries thermonatrite ($Na_2CO_3 \bullet H_2O$, circles) was observed and the amorphous hump at 28º 2-Θ is shifted to 25º. In the 7 day premixed samples traces of natron ($Na_2CO_3 \bullet 10H_2O$, pentagons) are present.

4.4.2. Discussion

The fact that premixing appears to have improved reactivity suggests that some initial reacted material is preserved through the subsequent dilution and evaporation, since the immediately diluted samples showed such minimal reactivity. This could be useful for certain applications where viscosity must be minimized (such as spray coatings). The fact that premixing time had a greater influence than concentration over the ranges investigated in this

experiment suggests that the range of premix concentrations could be expanded for further viscosity control.

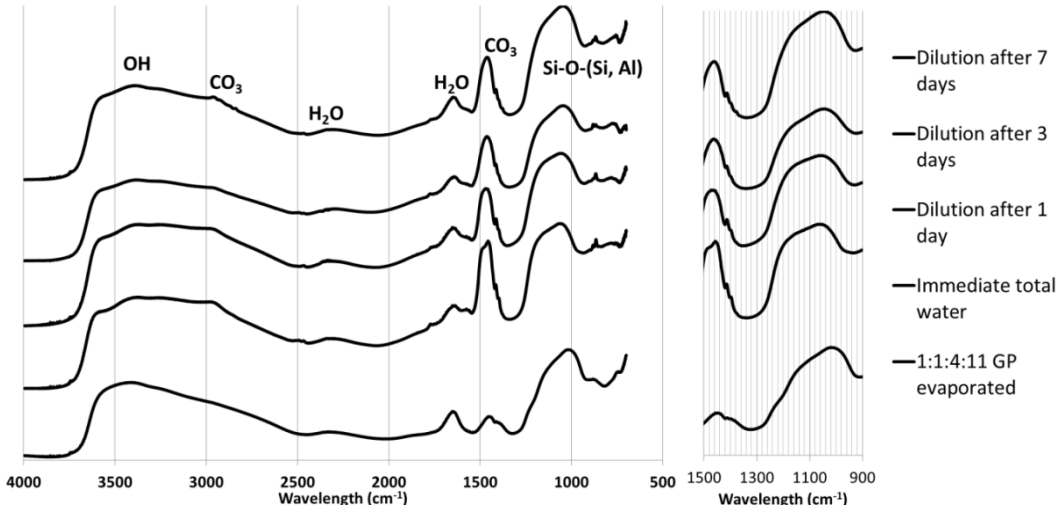

Figure 4.2. FTIR spectra of premixed evaporative geopolymers are compared. Dilute evaporative samples (197 mol water/mol GP) made with premixtures (34.2 mol water/mol GP) and without are compared to a standard dense geopolymer control. As seen in the closeup (right), premixing for an extended period shifts the Si-O-(Si, Al) stretch peak towards the right, indicating greater aluminate incorporation.

The ability to form carbonate rather than geopolymer is also apparently a consequence of the differing concentrations of reagents in solution. Kinetic analysis of geopolymer[67] and similar systems[122] identify hydroxide concentrations as critical to dissolution of the aluminate species. The subsequent condensation reaction depends completely and approximately quadratically on the concentration of aluminosilicate oligomers in solution[67] while the formation of the competing carbonate salt precipitates should depend only linearly on carbonate concentration. Thus in a dilute system carbonate salt precipitation should dominate.

Alternatively, sample temperature differences might significantly affect precipitation nucleation. Although all samples were present in 25 ºC conditions, relatively rapid

geopolymerization occurring in regular geopolymer controls increases the sample temperature significantly. At temperatures around 25 ºC, thermonatrite precipitation occurs readily with minimal nucleation time, while at higher temperatures significant nucleation time has been observed[123].

Table 4.1. Position of primary Si-O-(Si, Al) stretch peak, as determined by FTIR

Sample Initial Water Content 1•1•4•x (mol/mol GP)	Si-O-M FTIR peak (cm^{-1})			
	Never diluted	Diluted to 1•1•4•197 after 1 day	Diluted to 1•1•4•197 after 3 days	Diluted to 1•1•4•197 after 7 days
11 (control B, sealed)	1008	Solid	Solid	Solid
11 (control B, evaporative)	1019	Solid	Solid	Solid
197 (dilute slurry C)	1061	--	--	--
18.1 (premix C2)	--	1056	Solid	Solid
22.9 (premix C2)	--	1051	Solid	Solid
34.2 (premix C2)	--	1058	1042	1044
37.4 (premix C2)	--	1059	1057	1046

Note: Values close to 1080 cm^{-1} indicate that the symmetric Si-O-Si stretch dominates. Premixes marked 'solid' solidified despite the mixing process and were thus unable to be used.

Creation of a dilute evaporative geopolymer with full reactivity proved to be difficult. Substituting the sodium aluminate for the less reactive metakaolin proved ineffective, as bayerite ($Al(OH)_3$) was produced in preference to geopolymer. For controls, Metamax EF solidified within the planetary mixer for any reasonable degree of mixing, so Metamax HRM (3.6 μm median particle size[117], BASF Corp., Florham Park, NJ) was used. Likewise, the dispersant was omitted due to its phase separation in the planetary mixer. Other experiments indicated that there is no meaningful effect of these changes on geopolymerization.

CHAPTER 5

CONSIDERATIONS ON POROSITY MEASUREMENT

This chapter is partially composed of material submitted for publication[‡§].

5.1. Introduction

Despite several tools devoted to the purpose, an exact porosity and pore size distribution measurement remains impossible. Unlike other material property tests in which consistent methods apply over a range of materials, porosity measurement techniques require adaptation to the sample, due to the vast differences that are possible in pore size, shape, interconnectivity, accessibility and surface roughness. Consequently, it is imperative that porosity measurement techniques be carefully justified or at least described.

At the same time, advancing the theory of porosity measurement itself is useful, because important processing and industrial decisions are made with data from these measurement techniques. From a practical standpoint, pore size distribution data generally speak only indirectly toward material properties, but is valuable in scientific analysis as a microstructural and nanostructural description.

5.2. Problems in Porosity Measurement

The difficulties in measuring porosity in ceramics are both theoretical and practical. The theoretical issues are mostly issues of geometry and in the functional definition of a pore

---

[‡] B. E. Glad and W. M. Kriven. "Optimization of Gas Adsorption Porosimetry for Geopolymer Analysis," J. Am. Ceram. Soc., (2013), submitted.

[§] B. E. Glad and W. M. Kriven. "Augmentation of Cycling Intrusion-Extrusion Mercury Intrusion Porosimetry for Percolating Network Solids," Cement Concrete Res., (2013), submitted.

diameter. While air entrainment[45] and similar methods can produce spherical pores, and various other templating methods can produce pores of specified shape, pores of uncontrolled shape are harder to describe.

It has been typical[124] to use approximations such as dividing interior open volume into relatively large spherical or ellipsoidal cavities (pores) and constrictions connecting these pores (throats), or defining spaces between hypothetical close-packed spheres as the pore network. Standard analysis then defines pore diameter as an equivalent sphere (for pores) or an equivalent cylinder (for throats). Certain modifications can be made to accommodate slit-like geometries[125], but for intermediate and arbitrary geometries, no truly satisfactory measurement scheme has been devised. Thus, any pore size distribution measurement has meaning only with regards to the model used to derive it.

On a practical note, there are three different common methods for measuring pore size distribution. The first and most straightforward is a variety of different cross-sectional imaging methods which identify the pores visually and count the pores of various sizes in a randomly selected area or randomly selected set of lines. The difficulties involved in this method relate both to correctly contrasting pores and solid material, and to correctly interpreting pore shapes from the two-dimensional images. The other two methods, mercury intrusion porosimetry and gas adsorption porosimetry are investigated extensively in this project and specific difficulties with these tools are described below.

5.2.1. Nitrogen Adsorption

Nitrogen adsorption porosimetry is exceedingly valuable in both specific surface area measurement and in pore size distribution for micropores. While obtaining the adsorption

isotherm is relatively straightforward, converting the result to meaningful microstructural data is not so simple. Traditionally, specific surface area measurement is calculated using the BET method[126], while pore size distribution is estimated using the BJH desorption method[127]. Both of these methods make relatively crude assumptions in order to convert the adsorption isotherm to useful information.

BET theory assumes that every adsorbed layer after the first has an identical number of sites and thus implicitly ignores all geometric concerns. BJH theory assumes only cylindrical pores (although numerous corrections exist to expand the work to various geometries such as slits). Thus, both methods are only approximations. The most modern treatment of adsorption pore size distribution, non-linear density function theory[128], is today's primary method of adsorption pore size analysis, but is relatively crude itself.

Of more concern to the experimenter using this technique for geopolymers is that outgassing from the sample meaningfully affects the measurement. Since geopolymers at equilibrium possess several moles of water per mole geopolymer, it is quite possible for even tiny amounts of water to be released during the analysis. The partial pressure of this water is incorrectly interpreted as originating from unadsorbed nitrogen molecules, resulting in understating the quantity of nitrogen adsorbed. Unfortunately, this is only detectable from data analysis in very obvious cases (such as a region where negative adsorption is observed with increasing pressure, or when the total volume desorbed exceeds the amount adsorbed during the same analysis).

To prevent this effect, samples are extensively degassed. Existing geopolymer work has required both vacuum and elevated temperatures[14,15], but the effects of this treatment on the microporosity and the specific surface area have not been evaluated because an untreated sample

is not possible to test. Consequently, for geopolymers and other hydrated gels, the accuracy of this measurement is not known. Zeolites have such substantially higher gas adsorption than geopolymers that inferences from zeolite measurements are not appropriate.

5.2.2. Mercury Intrusion Porosimetry

By considering the capillary forces on pores filling with a non-wetting liquid, mercury intrusion porosimetry can provide a pore size distribution from ≈5 nm to hundreds of μm for certain simple pore geometries. An amount of mercury intrudes a pore of a certain size at a pressure inversely proportional to its entrance diameter, so that the number of pores of certain sizes can be determined. Thus, samples consisting of a percolating network of approximately monodisperse throats without interior pores can be measured accurately. Unfortunately, most real samples have pore size distributions radically different than this ideal case. In an open network of pores and throats, percolation theory (see Part 2.6) predicts that flow within the sample occurs above a certain critical value of porosity and only minimally below it. This criticality implies that in gradually increasing pressures to measure increasingly small pore volumes, the mercury intrusion porosimetry technique will observe a sudden large volume of porosity when the cumulative volume of pores larger than or equal to the size currently being measured first exceeds the critical value.

Thus interpreting the pressure data according to the Washburn equation[129] has obvious flaws for percolating networks. A more traditional analysis[130] argues that mercury intrusion porosimetry underestimates the volume of large pores and overestimates the volume of small pores, due to volumes interior to the sample unable to be intruded at low pressure due to the necessity of intruding smaller throats en route to a larger-diameter interior pore. One method of

compensating for this error is to intrude to a certain pressure, record volume intruded, and then decrease pressure to some intermediate value, which will cause extrusion from the narrow throats but not the interior wider pores. This allows deconvolution of interior pore volume from throat volume[131]. For a percolating network, minimal extrusion should occur until the pressure is fully decreased, but experimental evidence illustrates some mercury remains intruded even at a return to the filling pressure.

It is also reasonable to use a full intrusion to maximum pressure and then incrementally decrease and raise pressure to isolate intrusion of certain sizes of pores, by assuming that all other pores either do not drain or will never be filled at this pressure[132]. The presence of irreversibly filled pores casts doubt on the accuracy of this method as well[133], because once one break occurs at a tight neck, any appropriately sized pores behind the neck do not drain, and the subsequent intrusion underreports pores of that size by a value different than the amount irreversibly filled. Certain models[134,135] have attempted to account for these issues for various types of materials, in the hope of more accurately approximating pore size distribution.

5.3. Gas Adsorption Considerations for Geopolymers

Geopolymer mesoporosity makes gas adsorption an essential tool for the microstructural and nanostructural analysis of geopolymers, as it is for many ceramics. However, because geopolymerization reactions and curing occur at ambient or near-ambient temperatures, accurate measurement of the gas adsorption isotherm is quite difficult. Although geopolymer water can be removed prior to sample analysis, doing so requires heating and vacuum conditions that are more extreme than any environment to which the geopolymer was previously exposed. As a

consequence, several additional considerations beyond simple dryness of the ceramic are necessary to garner useful results from the technique.

Both the theoretical groundwork and many practical considerations for gas adsorption measurements are well understood and summarized elsewhere[136]. In most cases, the information acquired through gas adsorption, including specific surface area, mesoporosity and microporosity, cannot be easily acquired using other methods. Unfortunately, as seen in Figure 5.1, previous gas adsorption results for geopolymer have been ambiguous. This investigation seeks to evaluate how the typical gas adsorption techniques used are inadequate for geopolymers and to identify alternatives.

Common sources of experimental error in gas adsorption include surface alterations caused by the removal of adsorbed gasses or sintering, or structural changes to the sample due to the vacuum or temperature conditions. Typical artifacts of the experimental process may include free space and measurement errors due to gasses evolving from the sample, false equilibria due to long nitrogen diffusion times, or the inconsistency between model and real pore systems. Unfortunately, the only practical way of accounting for these errors in a sample as complex as a mesoporous geopolymer is through variance of sample preparation and experimental parameters. This document analyzes the effect of varying these parameters and shows that expected properties are only observed if correct experimental parameters are chosen.

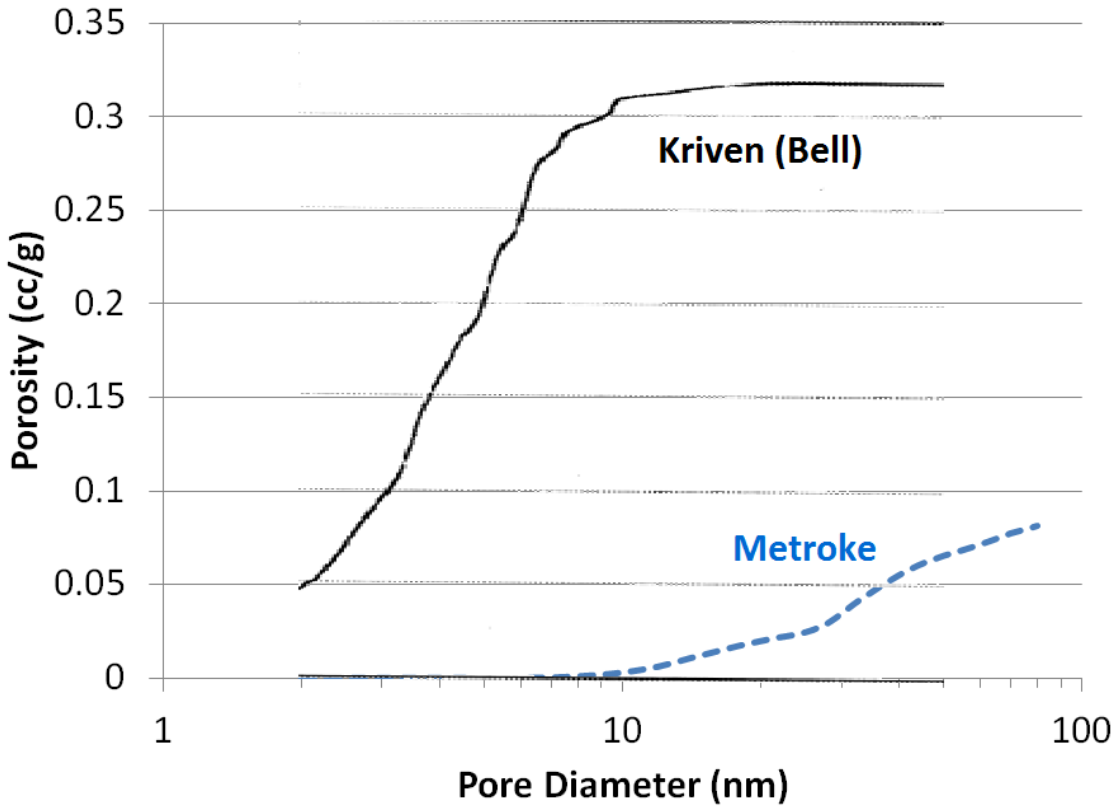

Figure 5.1. Porosity measurements of sodium silicate-metakaolin geopolymer as reported by Metroke[14] and Kriven[55]. Despite similar processing and composition, reported gas adsorption results are qualitatively different.

5.3.1. Gas Adsorption Experimental Procedures

(1) Synthesis

Geopolymers were synthesized from as-received metakaolin (MetaMax HRM, 3.6 µm median particle size[117], BASF Corp., Florham Park, NJ) and sodium silicate solution. Sodium silicate solution (waterglass) was prepared as follows: 160.0 g sodium hydroxide (Sigma-Aldrich Co., LLC, St. Louis, MO) was added to 360.0 g DI water in a stainless steel container and stirred using a polytetrafluoroethane (PTFE) stir bar with a magnetic stir plate until fully dissolved. The container was then sealed with plastic film, and the temperature of the stir plate

was set to approximately 45 ºC. A total of 240.0 g fumed silica (Cab-o-sil LM-150D, Cabot Corp., Boston, MA) was then added in small batches of approximately 10 g, each time allowing for complete or almost complete dissolution of the silica before adding the next batch, with the container remaining sealed when not adding silica. After all the silica was added, the container was resealed and the contents were allowed to stir at elevated temperature (≈45 ºC) for 24 hours. After 24 hours, the solution of sodium silicate was poured into a polyethylene container, and allowed to equilibrate sealed at ambient conditions for at least two weeks.

Samples were then synthesized in accordance with previous work[41] with 11.1 g metakaolin and 19.0 g (Formulation A, see appendix) or 18.5 g (Formulation B) waterglass, producing a nominal $Na_2O•Al_2O_3•4(SiO_2)•11(H_2O)$ Formulation (precise ratio for A 1.06•1•4.23•11.58, and for B 1.03•1•4.17•11.28 when impurities in the metakaolin are considered) and mixed in a planetary centrifugal mixer (ARE-250, Thinky Corp., Tokyo) at 1000 rpm for 180 seconds, with a 60 second debubbling at 1200 rpm.

Samples were cured in sealed PTFE or polyoxymethylene (POM) containers for the times specified, and held at temperatures specified until cured. Samples were ground into powder with an alumina mortar and pestle, and passed through a 44 μm mesh.

(2) Gas Adsorption Characterization-Instrument

Gas physisorption tests were conducted using ultra-high pressure (UHP) N_2 and H_2 and a commercial instrument (ASAP 2020, Micromeritics Instrument Corp., Norcross, GA). Free space analysis was conducted using UHP He immediately prior to each analysis.

(3) Gas Adsorption Characterization-Degassing

Prior to analysis, samples were degassed within the instrument's degasing system. All degasing was conducted at an evacuation rate of 670 Pa/s, with an unrestricted evacuation beginning when a pressure of 670 Pa was reached. During this evacuation, the temperature was increased to 90 °C or the target degassing temperature, whichever was less. When the chamber pressure of 1.3 Pa was reached, the temperature was, if necessary, further increased to the specified target temperature. Degassing was then conducted for 24 hours or longer at the target temperature, which was 200 °C for all experiments unless specified otherwise.

(4) Gas Adsorption Characterization-Experimental

Each nitrogen analysis consisted of a complete adsorption curve measurement between relative pressures 0.001 ± 0.0005 and 0.995 ± 0.007 P/P_0 (or to saturation, as specified), with an immediate desorption curve down to 0.05 ± 0.0025. The equilibration interval used was defined as the minimum time over which a 0.01% pressure change can be observed before a data point would be recorded, and this pressure change was evaluated using an 11-point Savitzky-Golay method[137]. Hydrogen analysis consisted of a complete adsorption-desorption curve between 16 ± 0.8 Pa and 93.3 ± 0.67 kPa using the same equilibration settings.

(5) Gas Adsorption Characterization-Analysis

BET surface area analysis[126] and non-local density functional theory (NLDFT) pore size distribution analysis were conducted using commercial software (MicroActive, Micromeritics Instrument Corp., Norcross, GA). BJH[127] adsorption and desorption pore size distribution results were compared for the purposes of tortuosity analysis. Langmuir[138] analysis was used for

hydrogen adsorption as no saturation pressure exists at 77 K for hydrogen. While a variety of other models exist, these are some of the most commonly used tools for mesoporous samples and are thus appropriate for comparison.

BET analysis was conducted using a 9-point fit of evenly spaced pressures between 0.075 and 0.275 P/P_0, inclusive. NLDFT pore size distribution analysis was conducted over the range 0.001 to 0.9 P/P_0, inclusive, using the Jaroniec cylindrical model[139] for zeolites and silica. This range corresponds to pores of sizes 1.3 nm to 25 nm. Fitting was conducted using ridge regression, with a regularization number[140] r_r of 0.0316. The regularization and fit is achieved by finding the pore distribution vector $\bar{f}$ minimizing the residual in Equation 5.1, where q_e is a vector of the experimental isotherm as a function of relative pressure P/P_0 and $\mathbf{Q}_m$ is a matrix of model isotherms of individual pores of various sizes, each described as a function of relative pressure.

$$minimize:\ 10\left\|\bar{q}_e - \bar{f}\boldsymbol{Q}_m\right\|^2 + r_r\left\|\frac{d^2\bar{q}_e}{d\left(\frac{\bar{P}}{P_0}\right)^2} - \frac{d^2(\bar{f}\boldsymbol{Q}_m)}{d\left(\frac{\bar{P}}{P_0}\right)^2}\right\|^2 \qquad (5.1)$$

BJH adsorption and desorption isotherms can provide a meaningful picture of tortuosity as a function of relative pressure and as an approximate function of pore size.

5.3.2. Gas Adsorption Results for Unmodified Geopolymers

As a rule, the investigation observed approximately the same amount of nitrogen adsorption onto metakaolin geopolymers as had previously been reported in the literature[14] when an identical 200 °C degas treatment was used. All of the nitrogen isotherms were type IV, which

is consistent with geopolymer mesoporosity observed throughout the literature. The investigation revealed that several processing parameters have an outsized effect on the adsorption and desorption isotherms. Artifacts related to the adsorption process, including prior degassing, appeared to be meaningful but predictably systematic as long as reasonable preparation conditions were used. Most notably, degassing at temperatures at or only slightly above the curing temperature resulted in a geopolymer with significantly increased surface area versus the same geopolymer degassed at 200 °C, and this significantly increased surface area resembles that of fly ash geopolymers[14], suggesting that the nanostructures of the two materials may be more alike than had been previously believed.

(1) Effects of Equilibrium Time

Results of a nitrogen adsorption test with 5 s, 20 s and 60 s equilibrium times on a typical geopolymer illustrate minimal differences in the resulting isotherms, as shown in Figure 5.2(a). A qualitative difference in isotherms between the powder samples and a bulk monolithic sample of the same material (also with 60 s equilibration time) illustrates the practical necessity of using powder for tests of reasonable length. As seen in the close-up of the isotherm (Figure 5.2(b)), at higher relative pressures the total adsorption measured increases with decreased equilibrium pressure rate. The qualitative and quantitative similarity between the 20 s and 60 s desorption curves suggest minimal accuracy gains from increasing the equilibrium time further.

Table 5.1 illustrates the total nitrogen adsorption and desorption at pressures $P/P_0 = 0.3$, 0.95 and 0.99 for these various tests, as well as the data collection time of the test. Balancing experimental accuracy with equipment availability was challenging, but this evidence suggests that a 5 s equilibration time was reasonable for this investigation. Only at pressures near

saturation was the deviation between the powder samples considerable. However, the high tortuosity of geopolymers makes a long equilibrium time mandatory for bulk samples. Note that the bulk sample was run to saturation rather than $P/P_0 = 0.995$. Although a considerable portion of the observed hysteresis is evidently an artifact of the time required for the adsorbent to reach equilibrium, the hysteresis provides valuable information on the pore tortuosity.

Table 5.2 illustrates that for BET specific surface area measurement, the powder sample results are approximately independent of equilibrium time. This is unsurprising because the BET method uses adsorption relative pressures up to approximately 0.3 P/P_0. The negative C value observed for the bulk sample indicates an extremely unreliable analysis as it implies a negative free energy of adsorption[136].

Table 5.1. Adsorption/desorption Data of a 25 °C Formulation A Geopolymer Measured with Various Equilibrium Times

Equilibrium Time (s)	Quantity of Nitrogen Adsorbed (cm^3 STP/g)			Data Collection Time (h:mm)
	$P/P_0 = 0.3$	$P/P_0 = 0.95$	$P/P_0 = 0.99$	
60 (bulk sample)	0.27	0.81	5.0	7:29
Desorption	0.20	2.4	15.6	6:14
5 (powder)	2.7	11.6	23.5	1:34
Desorption	2.7	15.1	25.1	0:55
20 (powder)	2.6	11.9	27.3	3:22
Desorption	2.6	14.3	27.8	2:15
60 (powder)	2.6	12.3	29.2	7:25
Desorption	2.6	14.4	29.2	5:04

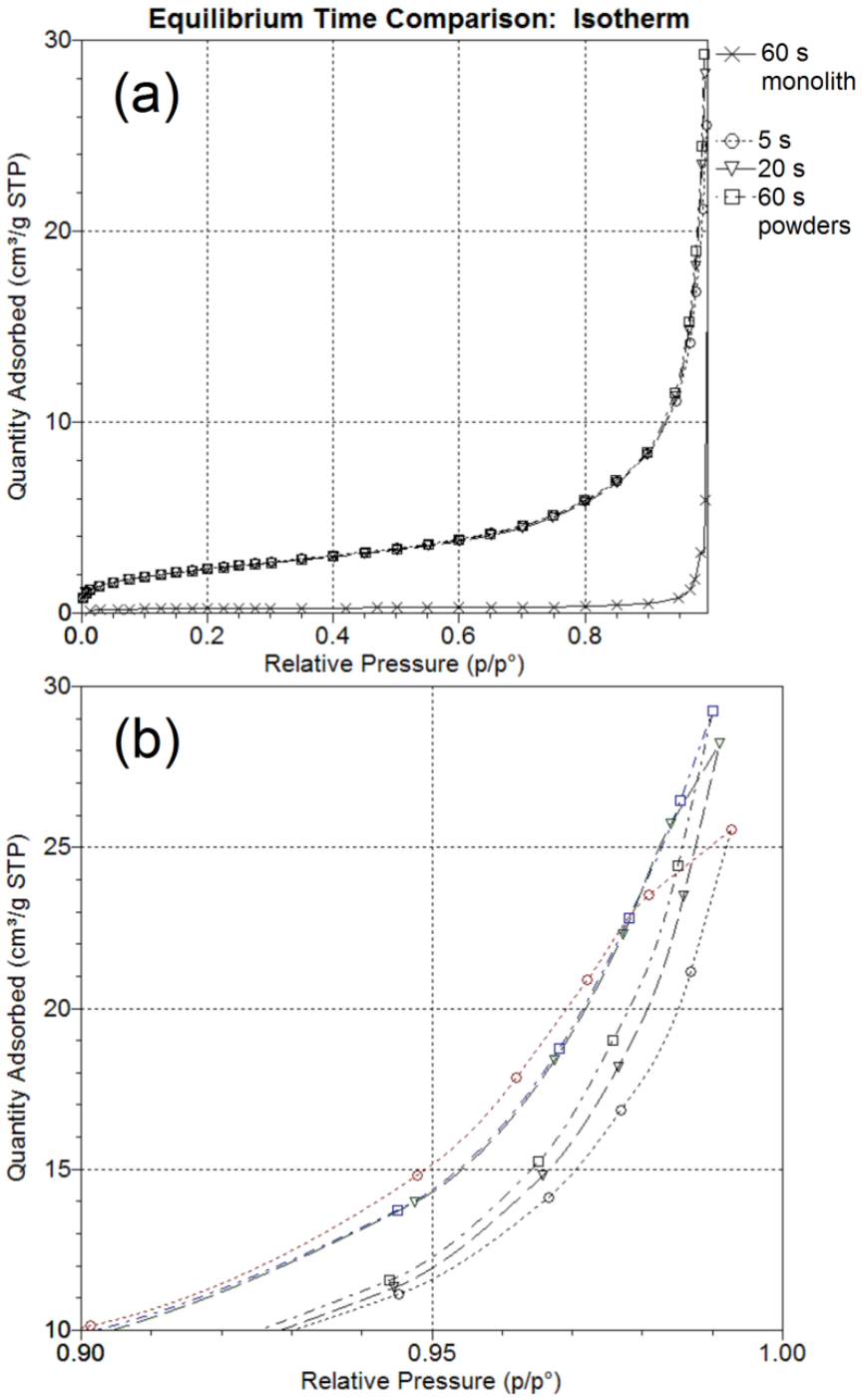

Figure 5.2. Nitrogen isotherm of a 25 °C Formulation A geopolymer, as recorded with various equilibration times (0.01% / time). All of the powder samples produced roughly the same isotherm (a), but deviation is visible at the highest relative pressures (b).

Table 5.2. Specific Surface Area of a 25 °C Formulation A geopolymer Measured with Various Equilibrium Times			
Equilibrium Time (s)	BET Specific Surface Area (m^2/g)	BET C-value	BET Correlation
60 (bulk sample)	0.85 ± 0.02	-306	0.9975
5 (powder)	8.58 ± 0.05	64.5	0.9999
20 (powder)	8.38 ± 0.05	77.3	0.9999
60 (powder)	8.42 ± 0.05	72.4	0.9999

(2) Effects of Degas Temperature

Figure 5.3 illustrates the effects of degassing to various temperatures on the adsorption-desorption isotherm. It is not clear that there exists an optimum degassing temperature for this material. However, the isotherms in Figure 5.3 illustrate a substantial difference between the 50 °C degas and the results from higher temperatures.

These samples were degassed using Transeal (Micromeritics Instrument Corp., Norcross, GA) sample holder stopper technology to maintain an airtight seal during transfer to the analysis port, which should prevent stray gasses or humidity from even minutely affecting the results. These samples were also run to equilibrium to identify contributions from all pores. The effect of the Transeal on the adsorption curve can be observed by comparing the 5 s equilibrium time results in the Effects of Equilibrium Time section above with the 200 °C results here. Table 5.3 shows the specific surface area results. It is important to note that not only the specific surface area but also the C coefficient is highest for the 50 °C degas sample. The C coefficient is a measure of the strength of gas-solid interaction versus gas-gas interaction, and its large value is consistent with the preservation of polar hydroxyl groups that may be removed in the degassing process[136,141,142]. It is also possible that these structural changes occur due to further polycondensation at incompletely reacted sites, which would also reduce the number of hydroxyl

groups. A water adsorption experiment would further alter the pore morphology with capillary forces as water reenters pores, but might still have value in helping to identify error sources.

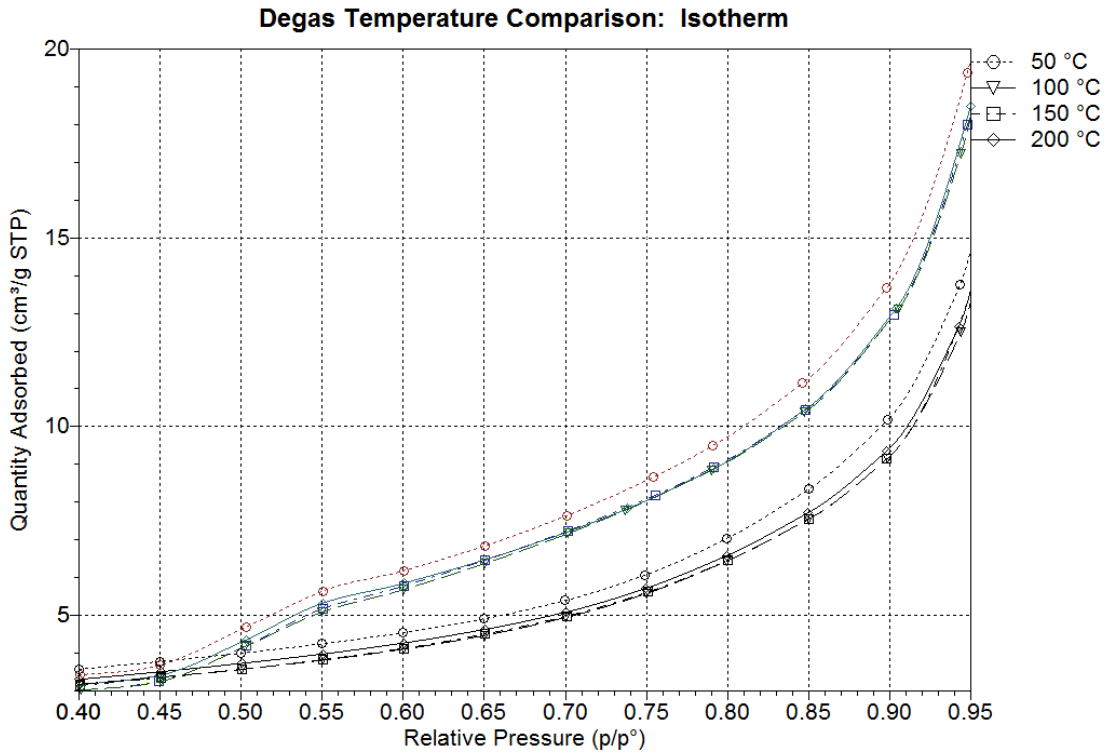

Figure 5.3. Nitrogen isotherm of a 25 °C Formulation A geopolymer after exposure to various target pressures during degassing. A change in the morphology of the geopolymer upon heating to 100 °C is evident.

Table 5.3. Specific surface area data of a 25 °C Formulation A geopolymer after exposure to various target pressures during degassing.

Degassing Temperature (1 day) °C	BET Specific Surface Area (m^2/g)	BET C-value	BET Correlation
50	10.09 ± 0.08	153	0.9998
100	8.95 ± 0.07	103	0.9998
150	8.87 ± 0.04	58.6	0.9999
200	9.35 ± 0.05	72.1	0.9999

It appears that a degas temperature greatly exceeding that of the sample curing temperature causes structural changes that meaningfully reduce the surface area and quantity of gas adsorbed. While degasing at room temperature is unreasonable due to practical concerns, it appears that a degas temperature less than 100 ºC may provide a clearer picture of the total surface area and gas adsorption. Examinations of the pore size distribution using NLDFT and adsorption BJH did not identify a particular set of pores that were being eliminated, but rather suggested decreased porosity at most pore sizes greater than about 8 nm. Similar results are shown in Figure 5.4, which demonstrates that the same effect occurs even for geopolymers cured at elevated temperatures.

(3) Curing Temperature Considerations

Figures 5.5(a) and 5.5(b) illustrate that compositional and curing temperature changes in the geopolymer synthesis create variation considerably larger than the above artifact-driven changes. In particular, curing temperature changes had a substantially greater effect than the composition change tested. Each temperature tested had a different characteristic isotherm, and the general features of this isotherm are consistent between both compositions.

This is reflected in the pore size distributions shown in Figure 5.6, and the specific surface area data in Table 5.4. Importantly, all six samples illustrate substantial similarities, including a maximum pore volume in the vicinity of 16 nm, and other clear maxima at approximately 8, 10 and 12 nm. These maxima may relate to additional nitrogen layers forming[143] or could potentially indicate a characteristic precipitate size.

The higher surface area for elevated-temperature cured geopolymers, and for the lower-silica Formulation B geopolymers, may represent increased zeolitic character in both cases.

With degassing at curing temperature, the temperature effect is even more readily visible, as seen in Figure 5.3. This would be reflective of the nanocrystal zeolites attributed to geopolymers in the literature, which include zeolite A, Na-X and sodalite[1,51]. All of these zeolites have Si:Al ratios considerably less than 2, and would be more likely to exist in silicon-depleted geopolymer. It is already well established that sufficient curing temperature can create a substantially zeolitic sodium geopolymer structure[8].

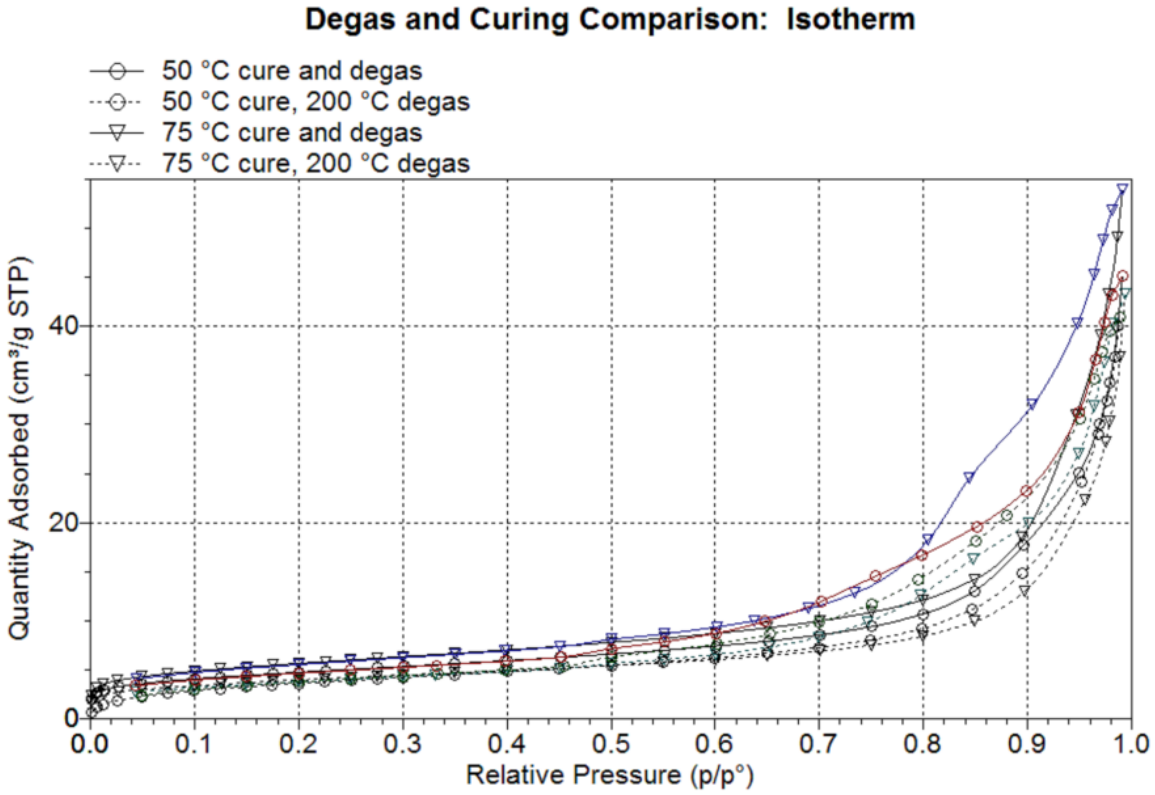

Figure 5.4. Nitrogen isotherms of 50 °C and 75 °C Formulation A geopolymers degassed either at their curing temperature or at 200 °C. Decreased adsorption with higher degas temperature is apparent. Only without the degassing at 200 °C is it possible to discern much greater adsorption for the 75 °C geopolymer than the 50 °C geopolymer.

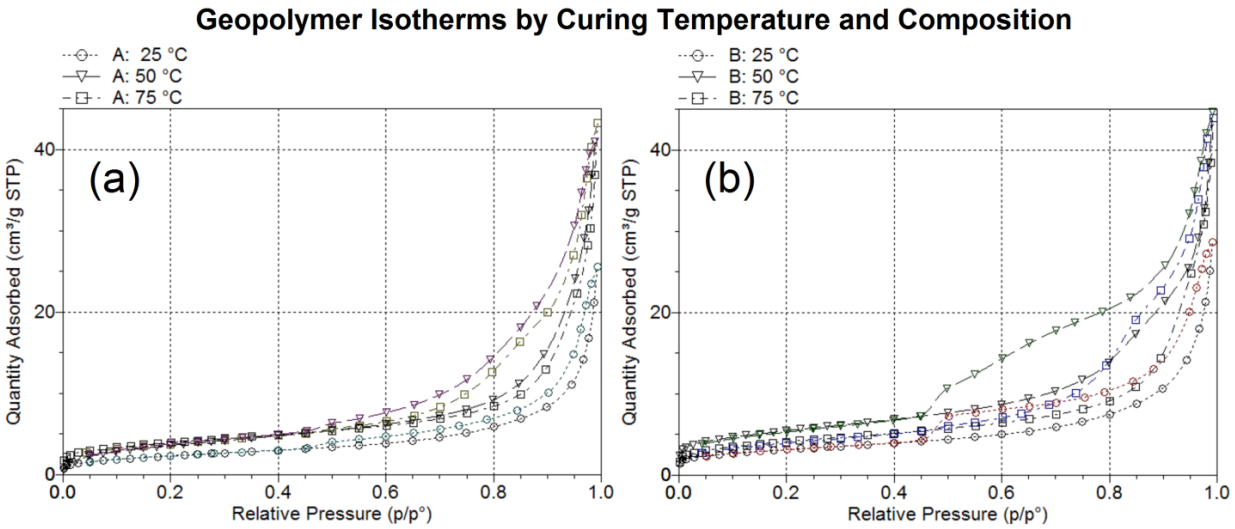

Figure 5.5. Nitrogen isotherms of Formulations A and B geopolymers cured at various temperatures (a), (b). Isotherm shape and degree of hysteresis appears to depend more on curing temperature than on Si:Al ratio.

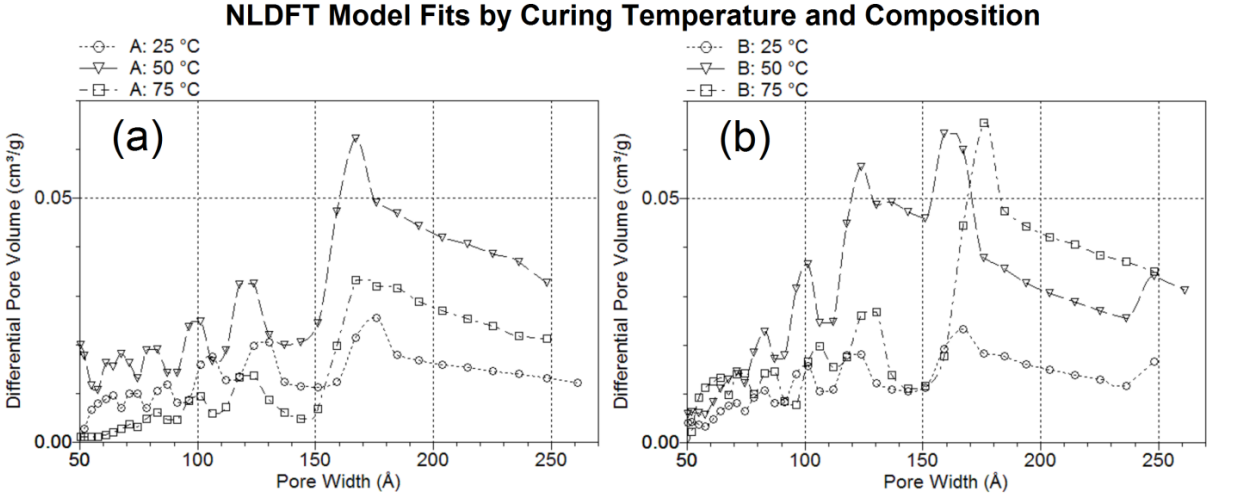

Figure 5.6. Non-local density functional theory pore size distribution results of Formulations A and B geopolymers cured at various temperatures (a), (b). All six samples illustrate a qualitatively similar distribution.

(4) Notes on Hydrogen Physisorption

A hydrogen physisorption experiment was conducted on a 25 °C Formulation A geopolymer to evaluate its applicability to the geopolymer system. The geopolymer hydrogen isotherm proved to be a Type I, as seen in Figure 5.7, as the much weaker gas-gas interaction results in a lack of multilayers. Thus, Langmuir specific surface area should be a reasonable approximation, but the surface area measured by this method was substantially less than that measured using nitrogen. Instead, the Langmuir specific surface area resembled that which would be measured with a nitrogen test at very low pressures ($P/P_0 \approx 0.001$ or less) which is consistent with the premise that the saturation pressure of hydrogen, if it existed at 77K, would be very high. More investigation is necessary to determine to what extent the hydrogen isotherm can substitute for time-consuming nitrogen micropore adsorption experiments at very low P/P_0 values.

Table 5.4. Specific Surface Area Results as a Function of Composition and Curing

Geopolymer	BET Specific Surface Area (m^2/g)	BET C-value	BET Correlation
A, 25 °C	8.58 ± 0.05	64.5	0.9999
A, 50 °C	13.77 ± 0.06	39.5	0.9999
A, 75 °C	13.97 ± 0.11	184	0.9998
B, 25 °C	11.14 ± 0.08	203	0.9998
B, 50 °C	19.38 ± 0.13	174	0.9998
B, 75 °C	14.61 ± 0.10	151	0.9999

5.3.3. Summary of Results

Nitrogen adsorption provides useful, repeatable data for both specific surface area and pore size distribution of geopolymers, and 0.01% / 5 s equilibration interval was found to be

sufficient for most characterization purposes. It was identified that even typical degas temperatures of 100 °C or higher meaningfully reduce the observed gas adsorption and specific surface area of a geopolymer sample and mask the important positive relationship between geopolymer curing temperature and specific surface area. This result and the observed positive relationship between metakaolin:waterglass ratio and specific surface area imply increased zeolitic character of metakaolin geopolymers under these conditions, and is consistent with known theory. Hydrogen physisorption was proposed as a possible alternative to low-pressure nitrogen micropore analysis, but more work is required to develop this possibility.

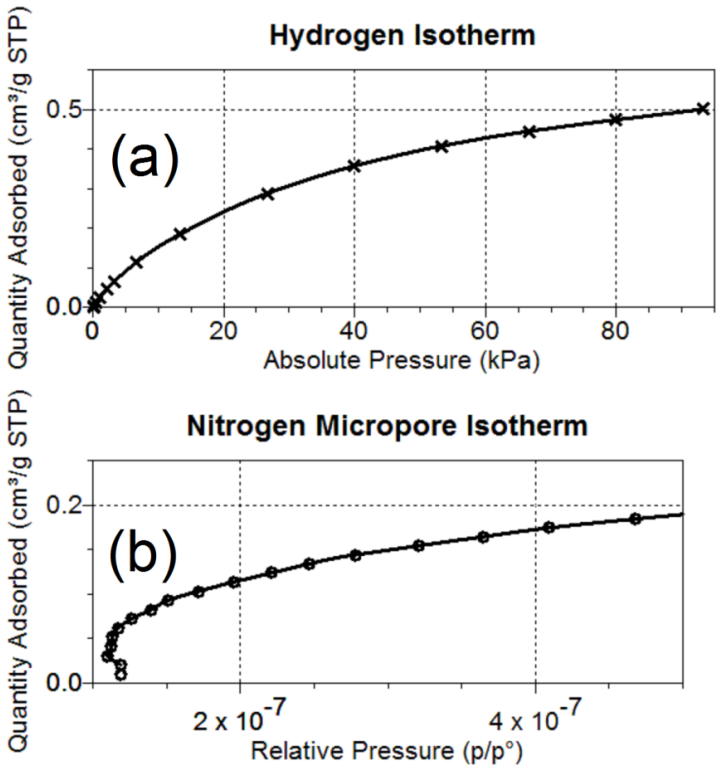

Figure 5.7. A comparison between hydrogen physisorption (a) and nitrogen micropore physisorption (b) isotherms for a 25 °C Formulation A geopolymer. The plots clearly resemble each other, but the nitrogen isotherm shows an artifact of trace helium residue from the free space measurement[136] because the pressures involved in the experiment are so small.

5.4. Proposed Kinetic Modification to Mercury Intrusion Methods

In theory, it would be possible to determine accurately a pore size distribution through the kinetics of intrusion, given a sufficiently accurate apparatus and a sample of sufficient size. It does not appear that such a mechanism has been considered elsewhere, possibly for technical reasons, but this section considers that possibility.

5.4.1. Proposed Kinetic MIP Theory

To correctly interpret kinetic results, several data are required. First, the head-dependent and channel-diameter dependent volumetric flow rate for mercury in the sample must be known. Appropriate values have already been described from Poisoulle-Darvy flow analysis and the results are described in Equations 5.2 and 5.3[133], where average velocity $\bar{v}$ over a distance L is in m/s, the diameter D and length L are in m, with a fluid pressure P in Pa.

$$\bar{v} = \frac{D^2}{L} * \frac{1}{2.21 * 10^{-10}s + 1.0 * 10^{-8}(Pa * s)/\,\Delta P} \tag{5.2}$$

$$L = D\sqrt{\frac{t}{2.21 * 10^{-10}s + 1.0 * 10^{-8}(Pa * s)/\,\Delta P}} \tag{5.3}$$

$$\frac{dL}{dt} = \frac{D}{2} * \left((2.21 * 10^{-10}s + 1.0 * 10^{-8}(Pa * s)/\,\Delta P)t\right)^{-\frac{1}{2}}$$

To determine L_{eff}=Lτ, a measure of the tortuosity τ is required, to determine the ratio of the length of the side of the sample to the length of the intrusion paths through the sample. This has been investigated intensively[144] although not for geopolymers. For a cylindrical pore network, τ is a function only of accessible pore proportion φ(D) (Equation 5.4).

$$\tau(\varphi) = 2.23 - 1.13\varphi, \qquad 0.05 < \varphi < 0.95 \tag{5.4}$$

In addition, a correction exists[144] for arbitrary pore shapes, requiring the diffusivity of the sample as a function of pore size and the specific surface area.

Using this velocity, the logic of the kinetic-based calculation is straightforward. As seen in Equation 5.2, the smaller the pore diameter, the slower intrusion would take place. For simplicity, this section will utilize a theoretical geometry consisting of an open pore network in a cubic monolithic solid of side length s, sealed from mercury intrusion on five of its six sides. Thus, there is a percolating network extending from a single surface plane.

The Washburn equation ensures that pores smaller than a certain diameter D_w (corresponding to the pressure chosen for the test, and the contact angle of the material with mercury) will never be intruded. Thus, there is a maximum intrusion time t_f that relates both to the pressure and the size of the sample, and relates to the volume of mercury reaching the opposite side of the cube following a path using only the smallest possible pores D_w, (with measurement imprecision, this measured volume describes the interior pores of some size range $[D_w, D_w + \varepsilon]$, with the range determined by the interval of recorded data points). In practice, the intrusion time should always be shorter than that time, because the mercury will pass through wider regions and progress through the cube faster. Thus, the last measurement recorded will be a measurement representing use of only the smallest pores at the 'deepest' part of the sample (that is, the portion of the sample farthest from the porous surface). Thus, the volume of the smallest pores is Equation 5.5.

$$V_{smallest} = \left.\frac{dV}{dl}\right|_{l \to L_{eff}} * L_{eff} \tag{5.5}$$

This value can be solved as a function of the time-domain data using Equation 5.3 if L_{eff} is known. For an unintruded sample, L_{eff} would be simply the product τs, in keeping with the

cube defined above. For an intruded sample, there is already mercury scattered through the entirety of the sample, so use of this method is more difficult.

However, with extrusion and a second intrusion, the ratio of throat volume to inkpot volume over this size range becomes known if appropriate intruding and extruding contact angles are used[130]. Thus, the volume measured has been divided into not two, but three types of pores: throat pores of size range $[D_w, D_w + \varepsilon]$, inkpot pores of size larger than $D_w + \varepsilon$, and interior pores of size range $[D_w, D_w + \varepsilon]$. This measurement could be repeated with new intruded samples and different initial pressures, or one might assume that the observed ratio of throat pores to interior pores of the same size is reasonably constant over the whole range of pore sizes, in which case a full pore distribution can be achieved with the cycling MIP technique[131] and appropriate addition of the throat and interior pores of each measured range.

This assumption is more complicated, but it also seems more reasonable than the typical assumption that is made. That assumption is that the sizes of inkpot pores for a given D_w possess the same distribution as the throat pores larger than D_w, and that assumption lays the groundwork for typical cycling MIP calculations. This method is thus proposed as a refinement to such calculations.

5.4.2. Caveat

The major limitation to pore size measurement on the scale of micrometers and smaller is the complexity of the required equipment. Testing of this kinetic MIP method was not possible for this investigation due to lack of continuous data collection in the Autopore II 9220 (Micromeritics Instrument Corp., Norcross, GA) porosimeter available, but more modern

porosimeters should be able to utilize it. It also was not possible to conduct the great variety of experiments required to verify this method elsewhere for funding and logistical reasons.

5.5. Augmentation of Cycling Intrusion-Extrusion Mercury Intrusion Porosimetry for Percolating Network Solids

The pressurization-depressurization cycling[131] mercury intrusion porosimetry system (PDC-MIP) is one of a vast number of modern efforts relating mercury intrusion porosimetry (MIP) results to pore size distribution (PSD). It was recognized long ago[145,146,147,148] that the Washburn equation[129] for capillary flow within parallel tubes is inadequate for pore size distribution analysis of MIP intrusion curves[133]. Errors occur due to hysteresis effects, which have been addressed several different ways, but no way has been altogether satisfactory. Hysteresis occurs as a result of several factors, including interior cavities (inkpots), surface roughness, network effects and draining energy issues[133].

PDC-MIP is particularly appropriate for accounting for hysteresis due to inkpots, but does not consider these convoluting factors in its calculations, instead assigning them to typical contact angle hysteresis[131]. This is probably appropriate for non-highly porous networks, but is problematic for higher porosities that lead to a percolating network. This document shows that, for percolating networks, the pore size distribution results from the PDC-MIP method are extremely sensitive to the choice of receding contact angle. It addresses that issue by presenting a modification to the PDC-MIP method derived from percolation theory.

5.5.1. PDC-MIP Background

A percolating network, defined as one in which flow can occur through an infinite volume[112], typically produces intrusion curves with minimal initial intrusion followed by a critical pressure P(Φ_{crit}) at which intrusion occurs (Region III in Figure 5.8). The shape of the curve (Region II in Figure 5.8) prior to that value depends not on the pore size distribution but instead on the ratio of sample size to the critical pore size[116]. Effectively, local areas which have both abnormally high porosity and are near the sample surface are intruding, and this intrusion is measured by the porosimeter.

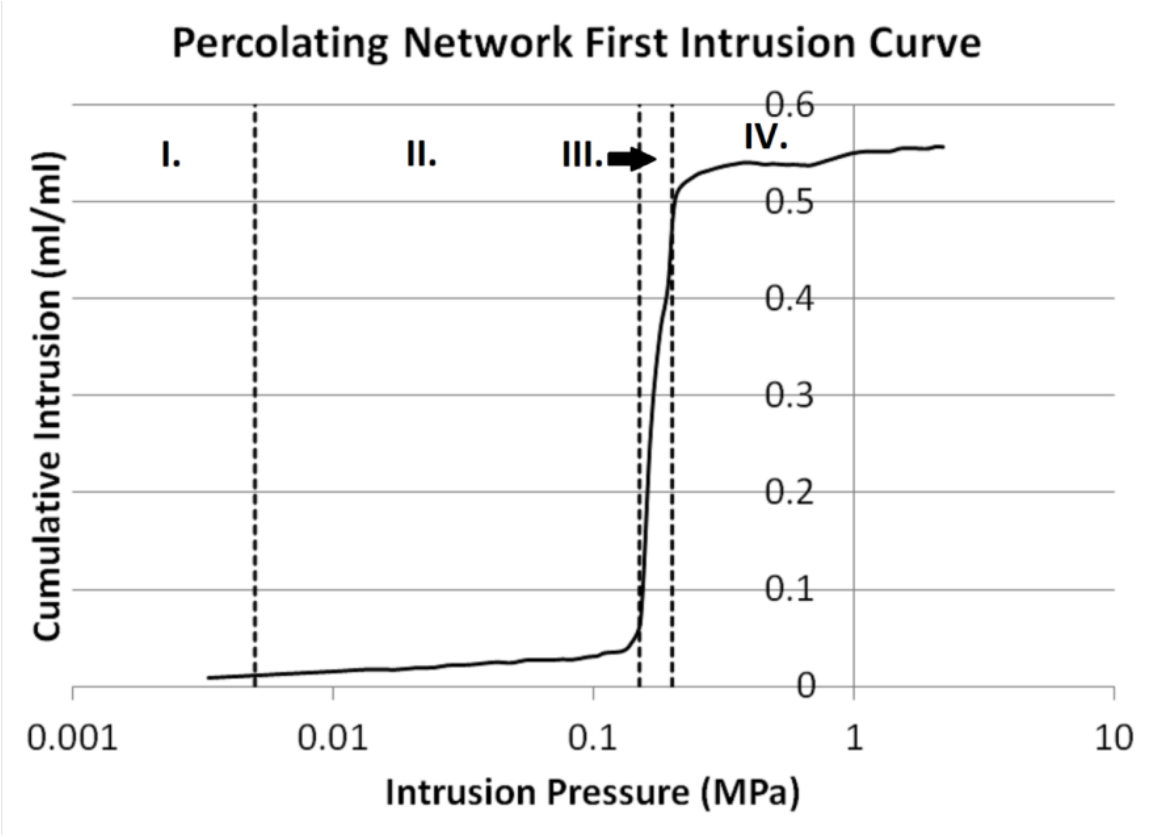

Figure 5.8. A first intrusion curve of a percolating solid (AF6). Indicated are the four major portions of the curve: Pre-intrusion region (I), pre-critical region (II), critical region (III) and intruded region (IV).

Accordingly, for an infinitely sized sample, percolation only occurs when accessible porosity exceeds some proportion Φ_{crit}. In a mercury intrusion porosimeter, no intrusion should occur until a pressure $P(\Phi_{crit})$ corresponding to a pore size smaller than the diameter of pores with total volume at least Φ_{crit}. Accordingly, in Figure 5.8, Region II should not exist, and Region III should be infinitely narrow. In cementitious materials, Φ_{crit} is approximately 18 vol%[113], implying coordination number Z of approximately 8.3, as in general $\Phi_{crit}*Z\approx1.5$ is a geometric result[112]. This is substantially similar to the 16% typically seen in simulations of percolating networks formed by non-overlapping particles[149]. When PDC-MIP is applied to a percolating network, it applies the vast majority of this entire 16-18% observed porosity prior to Φ_{crit} to the diameter ranges comprising Region II, which exists only because of the finite sample size. This network effect makes the PDC-MIP results difficult to interpret for percolating networks, because the amount of mercury that extrudes in the depressurization step is wholly dependent on the choice of depressurization pressure at each incremental step.

To determine the depressurization pressure as a function of the current intrusion pressure, the PDC-MIP method relies on knowledge of both advancing and receding contact angles[131]. As the receding contact angle Θ_{ext} is smaller than the advancing contact angle Θ_{int}, the depressurization portion of the cycle reduces the pressure by a constant proportion $\cos(\Theta_{ext})/\cos(\Theta_{int})$ for each data point, and in doing so implies that the incremental intrusion experienced during the first intrusion should all drain. Any volume that does not drain is assumed to have entered larger internal cavities that cannot drain until lower pressures, i.e. inkpot structures. By making the simplifying assumption that the observed inkpot volume can be distributed into large pores in proportion to the current pore size distribution, it is possible to

generate an entire distribution which will have necessarily larger pores than the first intrusion distribution.

5.5.2. PDC-MIP Modification Theory

The modification examined in this document derives straightforwardly from known theory. From Cassie-Baxter[150], we have the widely cited apparent contact angle for a liquid resting on a heterogeneous surface consisting of a portion φ of solid material and the remainder air (or vacuum), with a roughness parameter[151] k corresponding to the equilibrium areal ratio between a flat surface and the total surface contacted (Equation 5.6).

$$\cos\theta_{apparent} \equiv k\,\varphi\cos\theta_{solid} - (1-\varphi) \tag{5.6}$$

Combining Young's equation[152] for contact angle (Equation 5.7) with Washburn's parallel cylindrical tube model[129] provides the well-known result (Equation 5.8)

$$\gamma_{LV} * \cos\theta_{solid} = \gamma_{SV} - \gamma_{SL} \tag{5.7}$$

$$Pdl\pi r^2 = dl2\pi r * [(1-\varphi)(\gamma_{LV} - \gamma_{VV}) + k\varphi(\gamma_{SL} - \gamma_{SV})] \tag{5.8a}$$

$$P = \frac{2\gamma}{r} * [(1-\varphi) + k\varphi(-\cos\theta_{solid})] \tag{5.8b}$$

Cassie-Baxter's widely used approximation fails for extrusion due to an assortment of pinning effects[153, 154, 155] which result in contact angle hysteresis (CAH, the difference between intruding and extruding contact angles). The most typical method to estimate CAH is to compare the extrusion curve and the second intrusion curve and assign a receding contact angle such that the curves overlap[148,156].

However, the choice of receding contact angle is crucial to the PDC-MIP method as it effectively determines the proportion of throats to inkpots. From Equation 5.6, however, we observe that the ratio $\cos(\Theta_{ext})/\cos(\Theta_{int})$ might vary as the total amount of porosity observed changes. Unfortunately, this might mean that the appropriate ratio could change during the PDC-MIP experiment as with increasing pressure unintruded volume will decrease.

For an interconnecting or percolating network, one can generalize the pore structure as the scheme in Figure 5.9. It is convenient to assume, therefore, that every pore has roughly the same morphology and that therefore the cross-sectional area that a pore encounters as it opens into another is roughly proportional to its volume. Then, with only previous knowledge of total porosity, it is possible to approximate the void space that an incremental addition of mercury encounters at its triple-phase contact line (TCL) as unfilled porosity/unfilled space. Thus, the apparent advancing contact angle changes and converges on the equilibrium angle for the smooth solid as intrusion is completed.

Unfortunately, this method cannot work during extrusion as the entirety of the intruded volume must be considered rather than the differential area comprising the TCL. For a percolating, highly interpenetrating network, the pore volume can be divided into two straightforward categories. If Φ is the proportion of solid material in the sample in analogy to the area proportion φ described above, it is useful to define $ß(P)$ as the pore portion empty and $\alpha(P)=(1-ß-\Phi)$ as the pore portion full.

During the extrusion process, wherever there are interconnecting pores, two new bare mercury surfaces must be created to separate the mercury flow out of them. However, in each such case, two different pores are being emptied simultaneously. In a percolating network, one can approximate that this process happens with every pore not already drained. The likelihood

of encountering an area of full pores is α, but it is necessary to have two such areas coincident. By approximating the existence of these areas as two separate events, the probability of it occurring is $\approx\alpha^2$.

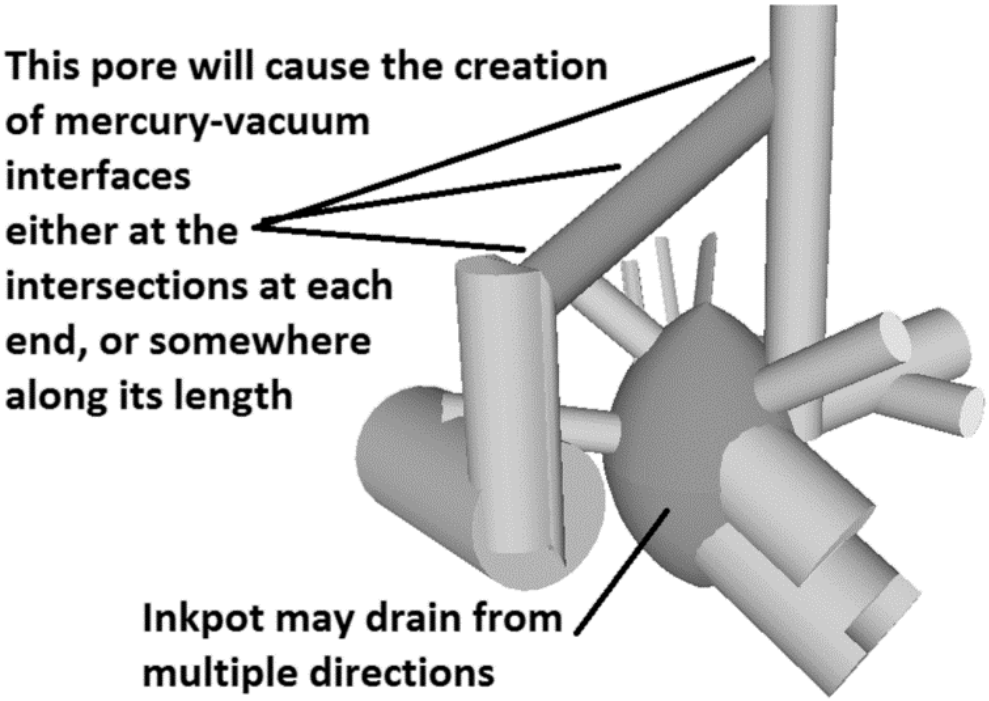

Figure 5.9. A sketch of a portion of a complex, interconnected pore network. During the depressurization step, some pores may be able to drain via two or more exits at once. To do so, a gap in the mercury must somehow be created, which requires the creation of two mercury-vacuum interfaces.

Thus Equation 5.9a, and trivially simplified 5.9b, is formed by modifying Equation 5.8b to account for this extrusion energy cost. This is the extrusion pressure-pore size relation, describing the pressure P_{ext} to which one must extrude to empty a pore of radius r. Equation 5.10, the intrusion pressure-pore size relation, utilizes Cassie-Baxter's method (Equation 5.8b, weighted by $1/(1-\alpha)$ to account for already-intruded volume), and P_{int} is always a larger pressure than is P_{ext}, as expected.

$$Pdl\pi r^2 = dl2\pi r * [\beta(\gamma_{LV} - \gamma_{VV}) + k\Phi(\gamma_{SL} - \gamma_{SV}) + 2\alpha^2(\gamma_{VV} - \gamma_{LV})] \quad (5.9a)$$

$$P_{ext} = \frac{2\gamma}{r} * [\beta + \Phi k(-\cos\theta_{solid}) - 2\alpha^2] \quad (5.9b)$$

$$P_{int} = \frac{2\gamma}{r(1-\alpha)} * [\beta + \Phi k(-\cos\theta_{solid})] \quad (5.10)$$

This pair of equations creates a system in which virtually no extrusion should be possible at low pressures where α is small, and extrusion should occur only until ≈ Φ_{crit} after P(Φ_{crit}) when α is large. This is exactly the same regime as should occur with the choice of an appropriate receding contact angle for the existing PDC-MIP method. Thus, this arithmetic would be expected to augment existing PDC-MIP method for percolating solids because it should a provide a qualitatively identical and quantitatively similar result as one would acquire using an appropriate receding contact angle with PDC-MIP, and does so without outside measurement of this receding contact angle.

5.5.3. PDC-MIP Modification Experiment

(1) Materials Evaluated

For evaluation of this methodology, it was necessary to use a simple, well understood product as a standard rather than a true cementitious material. Accordingly samples were taken from an AF6 alumina filter (Refractron Technologies Corp., Newark, NJ) with known specifications (Table 5.5). These monoliths were cut into cubes of side length 6.3 mm using a diamond edge wafer blade, and placed in a drying oven at 100 °C until dry.

Table 5.5. Alumina AF6 Filter Data[157]	
Open Porosity	42.9%
Maximum Pore Size	25.6 μm
Mean Pore Size	6.77 μm

(2) Mercury Intrusion Porosimetry

Mercury intrusion porosimetry data were taken using an Autopore II 9220 (Micromeritics Instrument Corp., Norcross, GA) porosimeter, and quadruple-distilled mercury (Bethlehem Apparatus, Hellertown, PA). AF6 cube samples were placed in 3cc sample holders and were evacuated for 5 min at 6.7 Pa immediately prior to filling at 3.5 kPa. It was found that an equilibrium rate of 0.001 μL/s resulted in incomplete equilibration, so a minimum of 5 minutes equilibration per step was used as an additional constraint. All data points used were averages of two or three experiments.

(3) Pore Image Analysis

Scanning electron microscopy SEM was used to obtain an independent measurement of the pore size distribution. AF6 rectangular prisms were mounted in epoxide, and the mounts were then vacuum-intruded with epoxide to enhance contrast. The samples were smoothed to a flat surface with a diamond-colloid polisher-grinder, Au-Pd sputter-coated to a thickness of 5 nm, and imaged at 25 kV using backscattered electron data (JSM-6060LV, JEOL USA, Inc., Peabody, MA). Ten 1280x960 pixel micrographs at magnification corresponding to 0.1 μm/pixel (1kx) were taken from random portions of the sample, and an additional five were taken at magnification corresponding to 0.4 μm/pixel (250x). Regular images with secondary electron detection were compared, and it was visually verified that the contrast observed in the

backscattered electron micrographs corresponded to the presence or absence of surface pores. Between image captures the stage was rotated to mitigate anisotropic microstructural effects.

Images were analyzed with a process depicted in Figure 5.10. The backscattered images were reduced to binary 'cow' images using the default threshold of ImageJ 1.46r (National Institutes of Health, Bethesda, MA) after a 0.5 μm Gaussian blur was applied. From each 1kx 'cow' image six 1280 pixel lines were randomly selected. Two each were selected from the top fifth, middle fifth and bottom fifth of the image to limit correlation effects. From each 250x image twelve lines were likewise used, three each from the top seventh, third seventh, fifth seventh and bottom seventh. Along each selected line, a pixel-counting algorithm estimated pore volume as a function of measured length by recording the distance between the start and end of each pore, considering that distance the pore length, and using a cylinder approximation with a circular cross section having an area equal to $\pi/4$ multiplied by the weighted areal average (that is, the second moment) of the recorded data. A spherical approximation, using the measured length as pore diameter, was also considered for comparison. The cumulative porosity was normalized to a maximum of the ratio of pore image area to total image area.

5.5.4. Results and Discussion

A first intrusion curve, PDC-MIP results for a variety of a variety of different Θ_{ext} values and results using modified pressure-pore size relation derived in this document are presented in Figure 5.9. The value used for Θ_{int} was 140°, as is typical for alumina standards[158,159], and was also the value used for Θ_{solid} for the modified relation sample.

It can be seen that the PDC-MIP results vary drastically depending on what receding contact angle is chosen. The modified relation result is intermediate between the various PDC-

MIP results, and it effectively assigns the critical percolation volume (16-18 %) to early data points, while the various PDC-MIP results vary drastically in this region according to the receding contact angle. In this manner, it organically derives the appropriate amount of depressurization for a useful result. Thus, the modified technique's results in Figure 5.11 are in qualitative and quantitative agreement with the expected results based upon percolation theory.

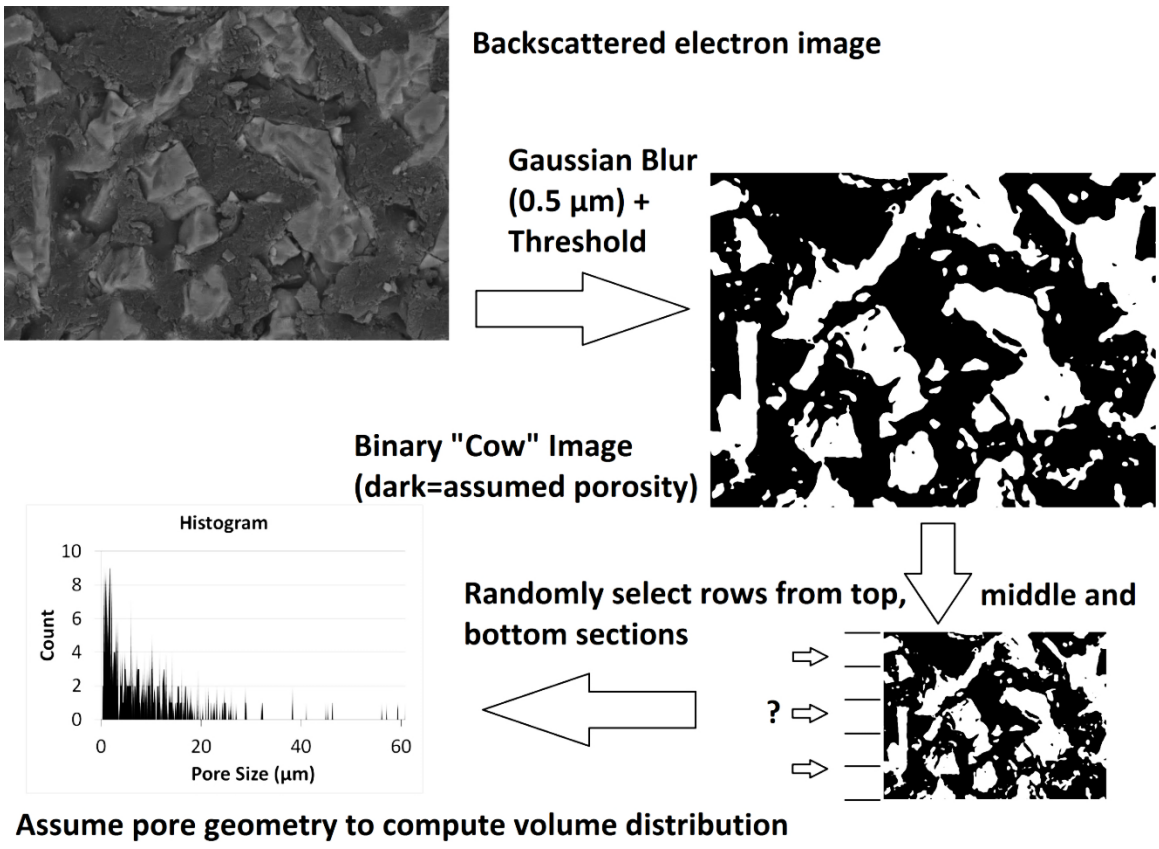

Figure 5.10. Scheme showing image-analysis process used for quantitative comparison of pore size distributions.

It is clear that neither the PDC-MIP technique nor the modified technique produce results resembling the cumulative pore size distribution curve observed with microscopy. As expected, the results were instead similar to a first intrusion curve due to the lack of observed throats prior

to the critical percolation pressure. It is expected that for purposes requiring a completely accurate pore size distribution, the well-understood[160, 161] repeated hysteresis loop method is still probably better than this method, but the experiment time is considerable. This method provides quantitatively intermediate results with relatively few data points required.

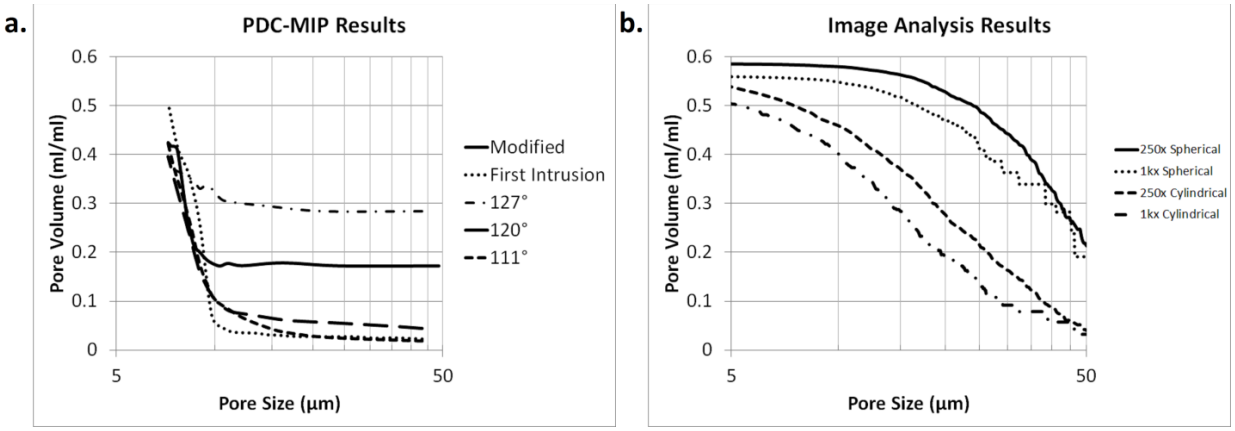

Figure 5.11. Direct comparison of PDC-MIP (a) and image-analysis (b) results. The PDC-MIP results vary dramatically with receding contact angle, and none of the curves qualitatively resemble the image-analysis curves. The modified method described here produces a curve intermediate between the various typical PDC-MIP curves.

The method was also tried using Formulation D porous geopolymers (see Chapter 7), but in each case it was observed that thermal effects caused by the repeated fast pressure changes created anomalies at high pressures. A typical result is shown in Figure 5.12. The total intruded volume drops below that of the first intrusion curve at high pressures, which is a nonphysical result suggestive of a nonequilibrium state. The experimental conditions heat the sample more vigorously, causing mercury to expand and a smaller value of porosity is measured. There is currently no in-situ temperature measurement which would permit fully compensating for temperature changes, so the testing method was not utilized for the porous geopolymers.

It is also possible that this result is due to the limited ability of the MIP to maintain high pressure for a long period of time, as the samples were given at least 300 s to reach equilibrium per point. Depressurization prevented equilibrium from being achieved at high pressures, so data was only applicable over the range shown in Figure 5.12.

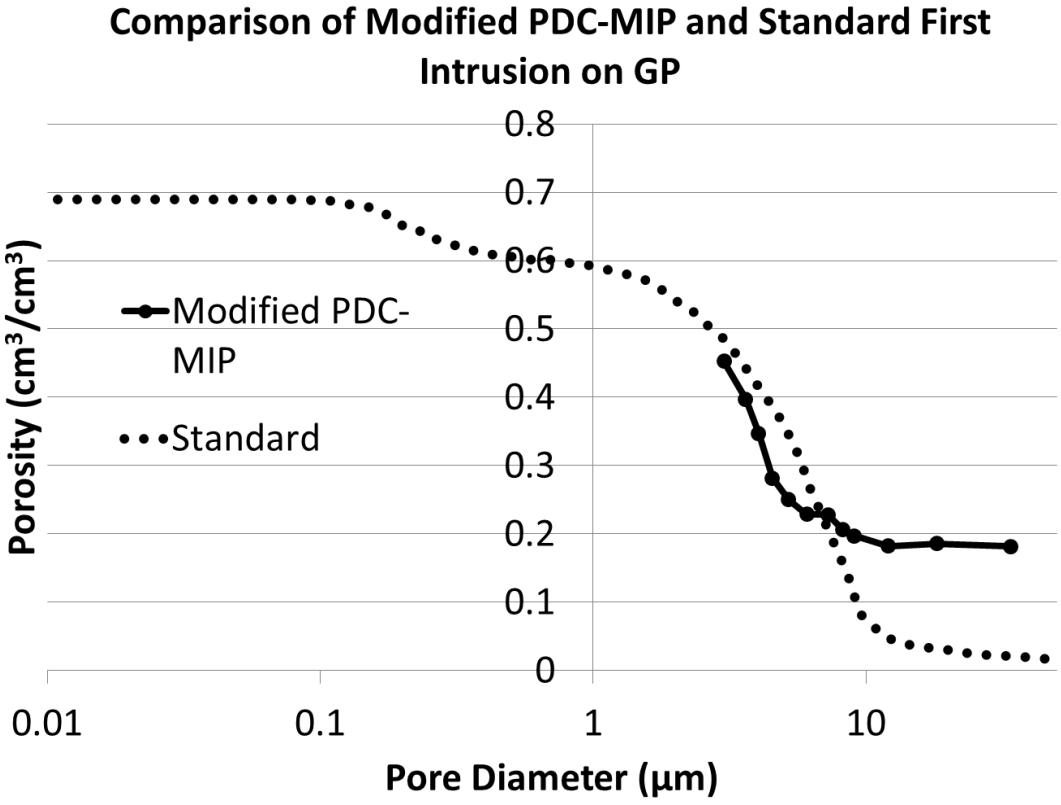

Figure 5.12. Comparison of modified PDC-MIP method and a typical first intrusion for a Formulation D geopolymer (GP composition 1•1•4•197, with molar ratio 1 Na_2O•1.00 $C_{12}H_{26}$•2.00 $Me_2Si(OEt)_2$). The modified PDC-MIP curve drops below the first intrusion curve due to thermal effects caused by repeated pressurization and depressurization. Longer equilibrium times could have allowed the system to reach equilibrium, but the inability for the porosimeter to maintain high pressure for long periods of time made that test impossible.

CHAPTER 6

GEOPOLYMER HYDRATION PROPERTY MODIFICATION USING ALKOXYSILANES

This chapter is partially comprised of material submitted for publication[**].

For most long-term uses, a geopolymer must survive, at the very least, humidity changes and most preferably immersion and drying. While existing composite geopolymers can do this, in many cases an unfilled geopolymer will experience cracking if aggressively dried or immersed. This topic was thus worthy of consideration, and some qualitative and quantitative testing was done.

6.1. Initial Experimentation

When it was established that slurries modified by silane coupling agents indeed created a geopolymeric solid with significantly reduced strength (see Chapter 3), it was also determined that the resulting solids showed a somewhat more reliable failure mode. This more reliable failure might be attributed to an organic second phase, but no large separate organic phases could be observed for the PAMS solids. It was possible that another mechanism other than reinforcement was in place, or that reinforcement was simply occurring in phases too small for noticeable effects on the scanning electron micrographs reviewed. To investigate this hypothesis, samples were made utilizing hydrophobic and hydrophilic coupling agents, mixtures, and controls.

[**] B. E. Glad and W. M. Kriven. "Geopolymer with Hydrogel Characteristics via Silane Coupling Agent Additives," J. Am. Ceram. Soc., (2013), submitted.

6.1.1. Drying Failure Analysis

It was found that geopolymers modified with some organics were capable of surviving difficult environmental conditions, including extended total immersion, drying at 95 ºC for 4 hours and immersion to full evaporation. It was observed that cylindrical samples (1.00 cm diameter, 1.00 cm height molds, Formulation B) synthesized with a mixture of MEMO and PAMS (1.5 wt% each) were capable of enduring any or all of these sequential treatments, and still possessed significant impact resistance. Unmodified geopolymers failed in fracture during immersion after drying.

It was found that the mixed silanes formulation described above observed densification (1.58 g/cc bulk density to 1.85 g/cc bulk density) as well as the expected mass loss (6.8 %) during drying at 95 ºC, while unmodified samples generally experienced a decrease in density despite a higher mass loss (10.3 %).

6.1.2. Modification with Polymer Superabsorbents

Sodium polyacrylate (repeat unit [-CH_2-CH(COONa)-]) is a well-known superabsorbent material that, when crosslinked, can absorb hundreds of times its weight in water[162]. It was expected that such materials would be able to trap water within the geopolymer if the superabsorbent formed only small separate phases. Acrylic acid (CH_2=CH-COOH) was expected to polymerize in geopolymeric curing conditions, while poly(acrylic acid) (PAA, repeat unit [-CH_2-CH(COOH)-]) was expected to remain a separate phase. Both would contain large proportions of the sodium acrylate conjugate base due to the high pH of geopolymer slurries.

The addition of acrylic acid (10 wt%) to Formulation B geopolymer resulted in total drying of the slurry during mixing, with a resulting crumbly, presumably unreacted solid. Lower

quantities of acrylic acid created a separate polymer phase which separated during mixing (presumably sodium polyacrylate). Addition of PAA to samples created a solid with an organic secondary phase, as predicted. Geopolymers with this additive had no improved water resistance versus unmodified geopolymer.

6.2. Modification with Superabsorbing Alkoxysilanes

Based on these observations and the discoveries discussed in previous chapters, it was reasoned that a major issue of geopolymers might be addressed through the addition of superabsorbing properties to the geopolymer slurry. A major weakness of geopolymer gels remains in that the large amounts of water required for both curing[67] and rheological reasons[7] create mesoporous structures which are sensitive to hydration and dehydration and will crack and fail if fillers are not adequately dispersed in the geopolymer matrix[26,163]. A reduction of post-curing drying shrinkage would greatly expand the applications of the geopolymer, especially in molded uses.

6.2.1. Introduction and Justification

No reliable method of decreasing slurry viscosity of geopolymers for a given amount of water content is known in the literature, despite there being evidence that the amount of water typically used in geopolymers is excessive. Recent investigations show that shrinkage occurs when the total water in the system decreases to the point where the hydration of the alkali cations begins to decrease[65], and that the majority of water used in geopolymer synthesis exists merely as free water in the final product. This would be expected to have detrimental effects on mechanical properties.

It has been observed that water reducers designed for Portland cement do not impart increased workability or final strength when added to a geopolymer mixture. This is unsurprising, as the geopolymer is seen to precipitate from monomers or short chain oligomers, such that there is minimal solid binder to disperse[164]. Thus, any structural changes that could impart increased strength for a given workability must apply to the latter stages of precipitation.

One method by which these structural changes can be made is through the co-condensation of alkoxysilanes within the geopolymer precipitates. Functionalization on the alkoxysilanes can alter the geopolymer network, resulting in nanostructural changes. These nanostructural changes would be expected to have predictable results on the microstructure and properties of the material. In particular, it is reasonable to expect that the addition of acrylic functionalization within the geopolymer might have long-range effects on the water transport and porosity, as the highly basic environment would create sodium acrylate functional groups within the structure. Such groups are typically used in polymer covalent networks to produce superabsorbing polymers, which deform in shape or 'swell' to accommodate vast quantities of water within the covalent matrix[165]. Without a network, the radius of hydration is severely limited[166]. Solvent swelling has been observed in certain acrylate-functionalized alkoxysilanes networked onto a polystyrene particle, but in that case the system is obviously quite different[167]. In this case, the covalent network that creates the swelling volume would be supplied by the SiO_4 and AlO_4^- tetrahedra amorphous network itself.

No previous investigation had considered the possibility of utilizing this swelling to accommodate the excess geopolymer water. This investigation involves the synthesis of a variety of different sodium metakaolin geopolymers based on this premise, and their characterization.

6.2.2. Experimental

(1) Synthesis

Geopolymers were synthesized from as-received metakaolin (MetaMax HRM, 3.6 μm median particle size[117], BASF Corp., Florham Park, NJ) and sodium silicate solution. Sodium silicate solution (waterglass) was prepared as follows: 160.0 g sodium hydroxide (Sigma-Aldrich Co., LLC, St. Louis, MO) was added to 360.0 g DI water in a stainless steel container and stirred using a polytetrafluoroethane (PTFE) stir bar with a magnetic stir plate until fully dissolved. The container was then sealed with plastic film, and the temperature of the stir plate was set to approximately 45 ºC. A total of 240.0 g fumed silica (Cab-o-sil, Cabot Corp., Boston, MA) was then added in small batches of approximately 10 g, each time allowing for complete or almost complete dissolution of the silica before adding the next batch, with the container remaining sealed when not adding silica. After all the silica was added, the container was resealed and the contents were allowed to stir at the elevated temperature (≈45 ºC) for 24 hours. After 24 hours, the solution of sodium silicate was poured into a polyethylene container, and allowed to equilibrate sealed at ambient conditions for at least two weeks.

Samples were then synthesized in accordance with previous work[41], except with the addition of one or more silane coupling agents (Gelest, Inc., Morristown, PA) or other organic modifiers (Sigma-Aldrich Co., LLC, St. Louis, MO), each used as received. The additives tested are listed in Table 6.1. Sample compositions consisted of 11.1 g metakaolin and 19.0 g (Formulation A) or 18.5 g (Formulation B) waterglass, plus the prescribed quantity of coupling agent. The reagents were mixed in a planetary centrifugal mixer (ARE-250, Thinky Corp., Tokyo) at 1000 rpm for 180 seconds, with a 60 second debubbling at 1200 rpm. The samples were then cured sealed at 25 °C for at least two days, before being removed from their molds and

stored in plastic zipper storage bags. For the cylindrical samples used in the drying experiment or in the compression tests, chamotte (Ceske Lupkove Zavody, Pecinov, Czech Republic) was added to the slurry to make a typical geopolymer composite. It was used as received.

Table 6.1. List of Additives and Their Abbreviations

Additive	Abbreviation	Summary of Results
Acrylic acid	AA	Phase separated during mixing
Methacrylic acid	MAA	Phase separated during mixing
Methacryloxymethyltrimethoxysilane	MEMO-Me	Limited microstructure modification
Methacryloxypropylmethyldimethoxysilane	MEMO-2,1	Minimal observed effect
Methacryloxypropyltrimethoxysilane	MEMO	Important microstructure modification
Phenylaminopropyltrimethoxysilane	PAMS	Minimal observed effect
Poly(acrylic acid)	PAA	Phase separated during mixing

(2) Macropore Size Distribution

Macropore size distribution was measured using mercury intrusion porosimetry (MIP). MIP was conducted using both traditional intrusion and modern cycling intrusion-extrusion methods[131], and experiments were conducted using purpose-built equipment (Autopore II 9220, Micromeritics Instrument Corp., Norcross, GA). Samples tested were cut with a diamond-edge wafer blade into cubes with 1 cm sides, and were degassed to 6.7 Pa prior to mercury filling at 3.5 kPa. Effective contact angle was determined using intrusion in slits cut with a diamond-edge wafer blade, and comparing the results to slit widths measured with an optical microscope.

(3) Mesopore Size Distribution

Mesopore size distribution was measured along with surface area using nitrogen adsorption. Gas physisorption tests were conducted using ultra-high purity (UHP) N_2 and H_2 in a commercial, purpose-built instrument (ASAP 2020, Micromeritics Instrument Corp., Norcross, GA). Prior to analysis, samples were degassed using the included degasing system. All degasing was conducted at an evacuation rate of 670 Pa/s, with unrestricted evacuation beginning when a pressure of 670 Pa was reached. During this evacuation, the temperature was increased to 90 °C. When the chamber pressure of 1.3 Pa was reached, the temperature was further increased to 200 °C and the sample was degassed for 24 hours, or longer if outgassing was still observed. In accordance with previous geopolymer research[168] some noteworthy results were verified with samples degassed at a maximum temperature of 50 °C for the several days required, and the predictable small increase in adsorption was observed.

BET specific surface area[126] analysis was conducted using a 9-point fit of evenly spaced pressures between 0.075 and 0.275 P/P_0, inclusive. Non-local density functional theory (NLDFT) pore size distribution analysis was conducted over the range 0.001 to 0.9 P/P_0, inclusive, using the Jaroniec cylindrical model[139] for zeolites and silica. This range corresponds to pores of sizes 1.3 nm to 25 nm. Fitting was conducted using ridge regression, with a regularization number r_r of 0.0316 [140]. The regularization and fit is achieved by finding the pore distribution vector $\bar{f}$ that minimizes the residual (Equation 6.1), where q_e is a vector of the experimental isotherm as a function of relative pressure P/P_0 and $\mathbf{Q}_m$ is a matrix of model isotherms of individual pores of various sizes, each described as a function of relative pressure.

$$minimize:\ 10\left\|\bar{q}_e - \bar{f}\boldsymbol{Q}_m\right\|^2 + r_r\left\|\frac{d^2\bar{q}_e}{d\left(\frac{\bar{P}}{P_0}\right)^2} - \frac{d^2(\bar{f}\boldsymbol{Q}_m)}{d\left(\frac{\bar{P}}{P_0}\right)^2}\right\|^2 \tag{6.1}$$

For pore sizes from ≈20 nm to 100 nm, the BJH method[127] of gas adsorption porosimetry analysis is considered to describe an approximation of the pore size distribution.

(4) Chemical and Reactivity Analysis

Analysis of the interaction between the condensed geopolymer and the coupling agent was conducted using X-ray diffraction (XRD) and Fourier transform infrared spectroscopy (FTIR) analysis. Cu-Kα X-ray powder diffraction testing was conducted with a D5000 diffractometer (Siemens-Bruker, Madison, WI). Tests were conducted at 40 kV, 30 mA, a step size of 0.02° 2-Θ, and a measurement time of 8 seconds/step. Diffuse reflection infrared spectra were taken using a Nicolet Nexus 670 spectrometer on powdered samples mixed with KBr (1:19 wt ratio). Powder samples for both instruments were generated by dry grinding in an alumina mortar and pestle, and were collected after being passed through a 44 μm mesh.

(5) Microstructural Analysis

Scanning and transmission electron microscopy (SEM, TEM) were used to investigate the microstructure and nanostructure of the material. SEM data were obtained on sample cross-sections cut with a diamond-edge wafering blade, mounted in epoxide and smoothed to a flat surface with a diamond-colloid polisher-grinder. The sample mount was Au-Pd sputter-coated to a thickness of 5 nm. SEM Micrographs were captured at 25 kV using a typical instrument (JSM-6060LV, JEOL USA, Inc., Peabody, MA).

TEM micrographs were obtained on powder samples prepared as above and placed on a carbon film. Samples were imaged at room temperature using an excitation voltage of 200 kV and a lanthanum hexaboride filament (JEOL 2010, JEOL USA, Inc., Peabody, MA). Care was taken to minimize beam exposure until immediately prior to image capture, especially for images of the organic phase.

(6) Drying analysis and shrinkage

Drying analysis was conducted on both geopolymers and geopolymer composites. Geopolymer experiments were conducted at ambient conditions and using Formulation B geopolymer composition samples modified with silanes as specified. They were cured at 50 °C in a cylindrical mold of 1 cm height and 1 cm diameter. Geopolymer composite experiments were conducted using 25 °C, 30% humidity conditions with cylindrical molds of 5 cm height and 2.5 cm diameter. Shrinkage was measured by the final equilibrium width of Formulation A geopolymers cast in 10 mm-width rectangular prism molds. The equilibrium widths of each were measured by calipers (average of six measurements) in the same ambient conditions after more than 2 months, and compared to the original 10 mm molded width.

Differential scanning calorimetry data were acquired at a rate of 1 °C/min from room temperature to 400 °C, and then immediately tested from 400 °C to 1100 °C at 5 °C/min. The testing chamber used (STA 409 CD, Netzsch Group, Burlington, MA) was a continuous airflow chamber and the gasses used were Ultra Zero Air and UHP Helium at a 15:8 volume ratio, which is a typical ratio with helium used to prevent damage to the instrument.

(7) Compression Testing

Compression tests were conducted on geopolymer and geopolymer samples with and without the addition of 0.1 mol MEMO/mol GP. Geopolymer slurry was poured into a cylindrical mold of 30 cm height and 1.27 cm diameter and vibrated on a vibration table until no further debubbling was observed. These samples were cured and the resulting geopolymer rods were cut into 2.5 cm high cylinders. Compression tests were conducted using an Instron 5882 load frame (Instron Corp., Norwood, MA) according to ASTM C39, except that drying shrinkage meaningfully altered the final diameters of the MEMO samples (see below) and in some cases caused eccentricity in the cylinder cross-section. Height-width correction factors were applied using a cubic fit. At least ten samples of each MEMO formulation were tested.

6.2.3. Results and Discussion

It was found that meaningful microstructural and property changes occurred as a result of adding MEMO to the geopolymer. Alterations in mechanical properties, water retention properties and drying shrinkage all directly result from the simple addition of this silane to the geopolymer slurry. It was shown that the effectiveness of the modifier on these properties depends on all aspects of the molecule, as none of the variations of MEMO tested caused substantial property modification. The addition of the silanes reduced the reaction completion, but not enough to significantly reduce mechanical properties or cohesion.

(1) Water Retention

Drying under various conditions revealed that the MEMO-modified geopolymer possessed greatly improved water retention characteristics, whether or not chamotte was added.

As seen in Figure 6.1, while both the MEMO samples and controls had flux-limited drying (rather than having a constant-rate evaporation-limited drying period) drying of the control was substantially faster, where the control geopolymer lost 20 % of its theoretical water mass within 9 hours, while the geopolymer modified with MEMO required 68 hours. It was further observed that the MEMO geopolymer did not approach equilibration within 2 weeks. The additional mass loss at very long times may have been due to loss of the silane itself or may suggest a higher equilibrium water loss. The latter might suggest the gradual depletion of hydrated sodium ions as they formed sodium methacrylate groups, which would be consistent with previous geopolymer research[65].

A direct comparison of the drying of several MEMO-modified, PAMS-modified, mixed MEMO-PAMS-modified and unmodified Formulation B geopolymers at ambient conditions found that drying rate depended on the presence and concentration of MEMO, and that the addition of PAMS had no effect on the drying rate. The results were observed for both as-cast samples and samples prepared by removal of the surface using a file, indicating that drying effects of MEMO occurred within the bulk of the geopolymer and were not merely a surface-sealing effect.

DSC-TGA data showed a delay in the onset of mass loss during heating, with control and 0.05 mol MEMO/mol GP samples exhibiting an immediate broad exotherm beginning at room temperature, while 0.10 mol MEMO/mol GP delayed the exotherm until ≈62 °C. The 0.15 mol MEMO/mol GP sample showed a sharp exotherm beginning at ≈69 °C. At the boiling point of MEMO (≈190 °C at atmospheric pressure), a small exotherm was observed for the 0.15 mol MEMO/mol GP sample but not for lower additive concentrations.

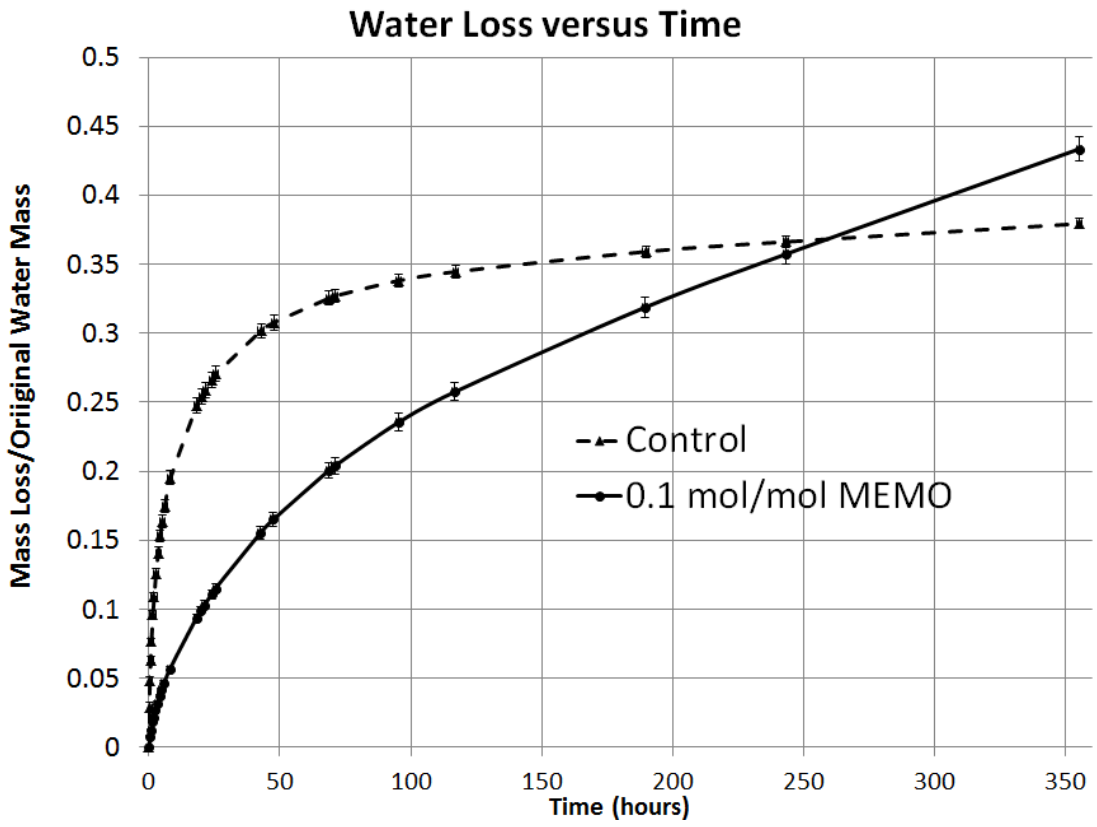

Figure 6.1. A comparison of mass loss rates as a function of time held at 25 °C and 30% relative humidity. Formulation A geopolymers cured at 50 °C showed rapid mass loss, while the same geopolymer modified with MEMO dried substantially more slowly.

(2) Mechanical Properties and Shrinkage

Compression and shrinkage properties of MEMO-modified geopolymers and geopolymer composites were compared with controls. As seen in Table 6.2, the effect of the MEMO additive on the compressive strength was minimal, but its effect on the Weibull modulus was considerable. This increased modulus implied a more reliable failure, suggesting that the MEMO was able to reduce crack propagation or other sources of brittle failure. Interestingly, MEMO additive reduced the strength benefit of the filler while the filler reduced the reliability benefit of the MEMO additive.

Table 6.2. Compressive strengths of geopolymer with and without MEMO additive		
Geopolymer Formulation (number of samples tested)	Strength (MPa)	Weibull Scale Factor (MPa), Modulus
A 25 °C (6)	15.5 ± 9.3	17.8, 1.80
A 25 °C with 0.10 mol/mol MEMO (10)	18.8 ± 5.3	20.8, 3.84
A 25 °C with 25 wt% chamotte filler (10)	44.6 ±21.9	51.5, 2.11
A 25 °C with 25 wt% chamotte filler and 0.10 mol/mol MEMO (11)	41.6 ±13.7	46.9, 3.14

Figure 6.2 shows the approximate drying shrinkage incurred by geopolymers as a function of MEMO additive. It is clear that significant shrinkage occurred upon addition of sufficient amounts of additive. The densification of the geopolymer that occurred during this shrinkage is even more directly related to the amount of additive. The bulk densities observed, as measured using mercury pychometry, are extremely high compared to other metakaolin Na-geopolymers described in the literature[13], and resemble those achieved for wet metakaolin geopolymers cured at low temperatures[68]. As the MEMO additive is not massive and could not be expected to form a particularly dense structure, these effects were attributed to changes in the porous geopolymer structure. The linear shrinkage results were observed to be related non-linearly to concentration, but the bulk density results showed a clear linear trend. This discrepancy could have been caused by the anisotropy of the sample shapes used in the linear shrinkage tests (1x1x10 cm bars), or to the additional vacuum drying of the samples required for the MIP test. Mercury intrusion found the porosity to be only minimally open, which is consistent with the micrographs observed. The lack of intruded volume in the MEMO-modified geopolymers made meaningless the macropore size distribution observed with MIP.

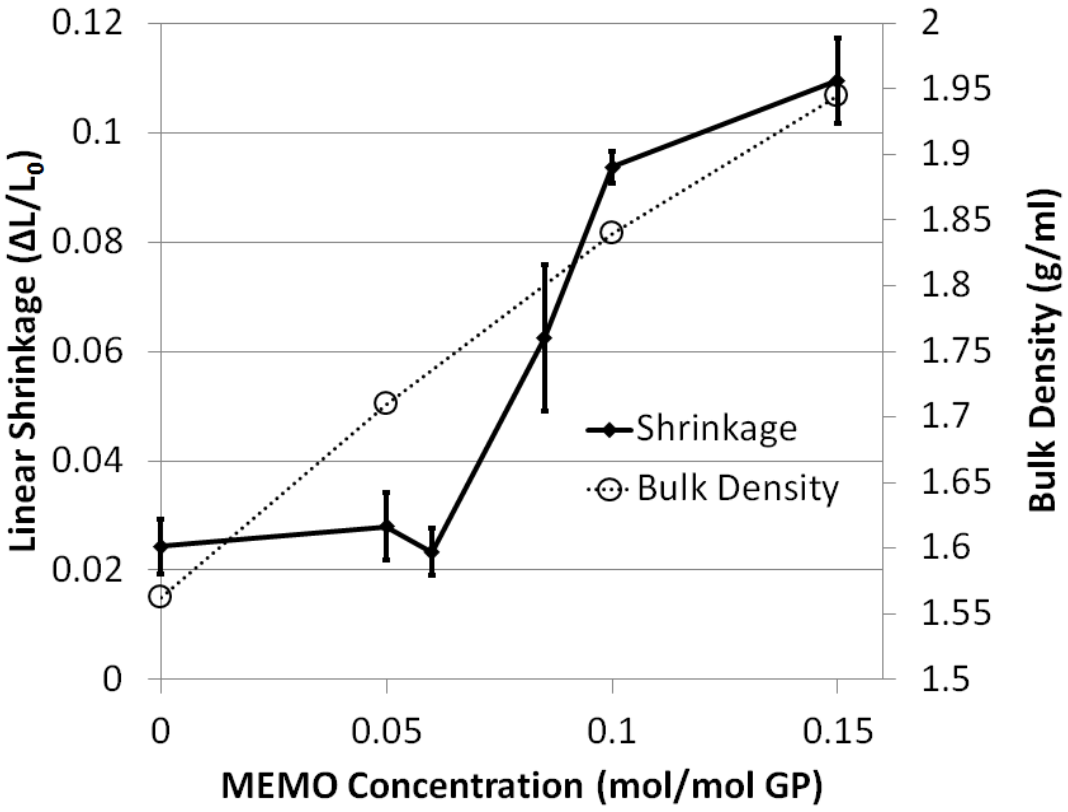

Figure 6.2. Linear shrinkage measurements of Formulation A geopolymers cured at 25 °C. After the addition of a critical amount of MEMO additive (approximately 0.06 mol/mol), further additive causes substantial linear shrinkage. Bulk density measurements using mercury intrusion porosimetry did not show such a critical change but instead increased smoothly with increased composition.

(3) Microstructure: Imaging and Composition

FTIR results showed clearly the interaction of the methacrylate groups with sodium cations, with the COONa asymmetric stretch at 1566 cm^{-1} and the symmetric stretch at 1394 cm^{-1} clearly visible[169], while the bare C=O stretch observed at 1717 cm^{-1} in MEMO[170] was not observed. It was impossible to exclude the possibility of MEMO polymerization at the carbon double bonds because its characteristic stretch at 1638 cm^{-1} overlaps the large, wide H_2O bend signal in the vicinity. Geopolymer reactivity, as measured by the Si-O-(Si, Al) stretch peak

movement[171], decreased with increasing MEMO concentration, as shown in Table 6.3. XRD diffraction results found substantially the same results.

Table 6.3. Reactivity data for Formulation A geopolymers

MEMO Concentration (mol/mol GP)	FTIR Si-O-(Si, Al) stretch peak maximum (cm^{-1})	Approximate XRD amorphous hump maximum (°2-Θ)
0	1008[171]	27.2
0.05	1020	27.0
0.10	1035	25.3
0.15	1043	24.6

SEM results revealed a dense microstructure with closed pores of μm to tens of μm in diameter interspersed amongst tightly bound precipitate aggregates. Some microcracking was evident amongst these pores, but the overall structure was quite dense by geopolymer standards. A direct comparison of the microstructures of Formulation A 25 °C GP with the addition of 0.1 mol MEMO/mol GP (Figure 6.3) showed substantially less porosity than is typical for sodium geopolymers alone[16,172]. Closer images of the higher-additive compositions illustrated the presence of curled organic films on a scale of 100s of nm to μm (Figure 6.4). These films were embedded into the bulk of the geopolymer as a separate phase and appeared to show no particular affinity for the pore surfaces. This strongly suggests that their formation occurred prior to the complete hardening of the geopolymer gel as otherwise a bulk organic phase such as the observed might be expected to be excluded by the growing geopolymer. From the images, it cannot be determined whether complete phase separation of the MEMO additive occurred, or alternatively whether the observed structures represented only the additive that was not strongly bound within the matrix.

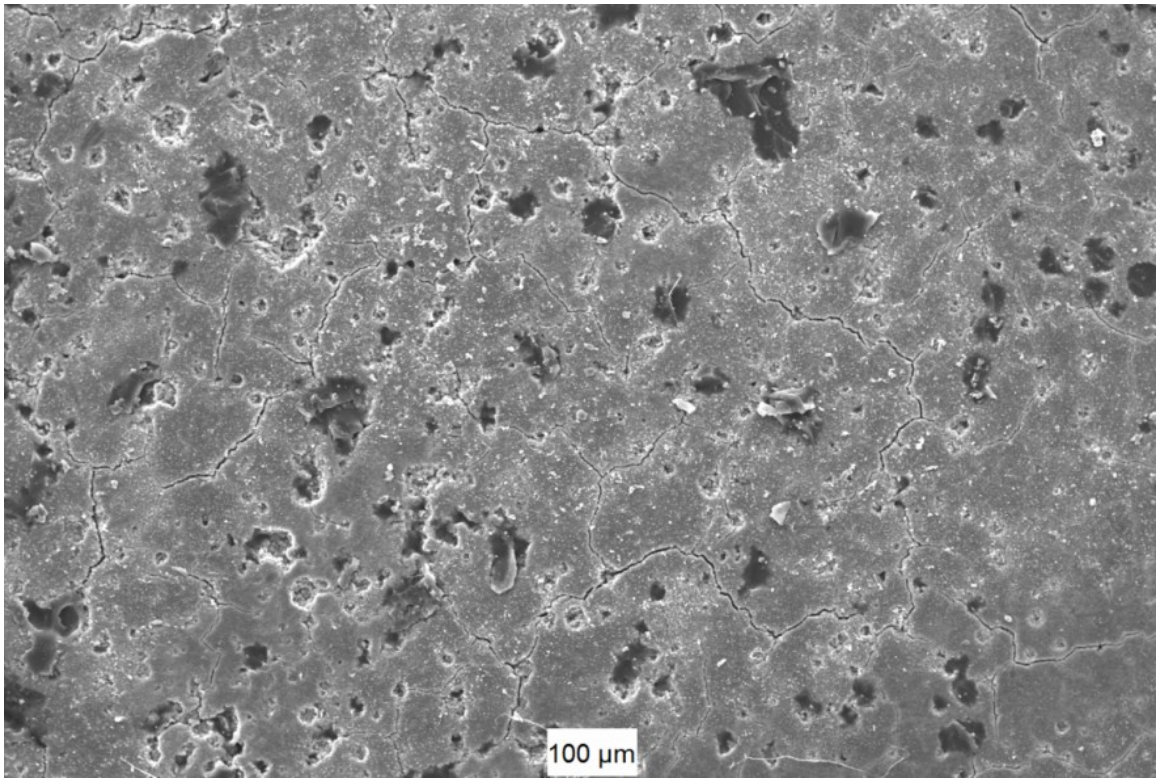

Figure 6.3. A scanning electron micrograph of a Formulation A geopolymer with 0.1 mol MEMO/mol GP. Macroporosity is sufficiently minimal that mercury intrusion results were not reliable.

(4) Nanostructure: Specific Surface Area, Precipitate Interaction and Organic Phase

Gas adsorption porosimetry indicated a marked decrease in specific surface area (SSA), as shown in Figure 6.5. From these data, it is clear that the extended propyl linker of MEMO allowed for greater nanostructural changes than did the methyl linker of MEMO-Me. The network modification capabilities of the methacrylate groups are likely individually quite short-range. Altering the alkoxysilane functionality of the additive or the acrylic nature of the functional group had an even more meaningful effect. Use of MEMO-2,1 as an additive rather than MEMO resulted in no meaningful SSA reduction. Use of PAMS also resulted in a smaller

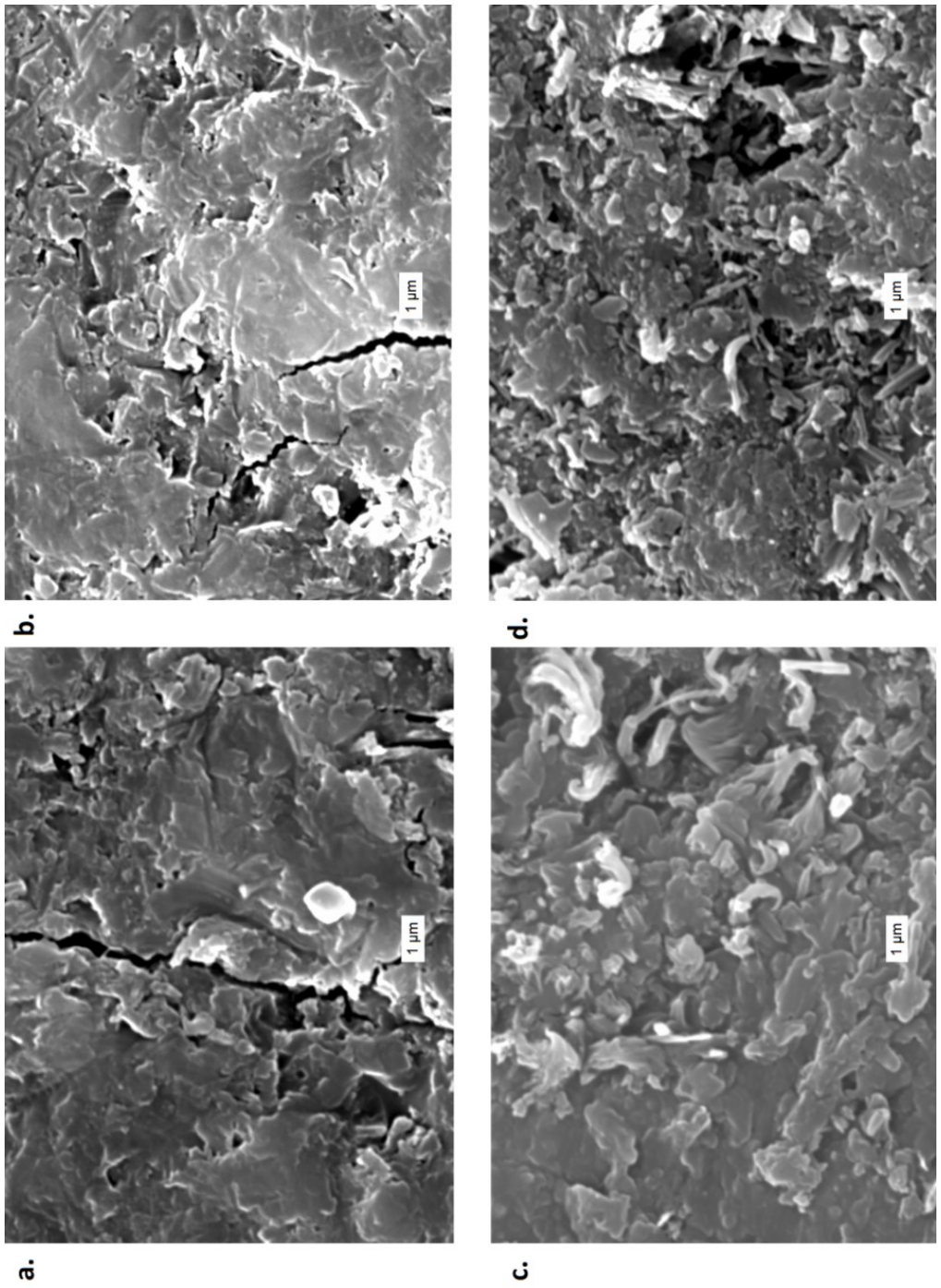

Figure 6.4. Scanning electron micrographs of Formulation A geopolymers with 0 (a), 0.05 (b), 0.10 (c) and 0.15 (d) mol MEMO/mol GP. As MEMO concentration increases, microstructural complexity and unreacted phases begin to appear. Membranes formed by the organic material are seen with high MEMO concentrations (c, d) where they appear curled up and bonded tightly into the geopolymer matrix.

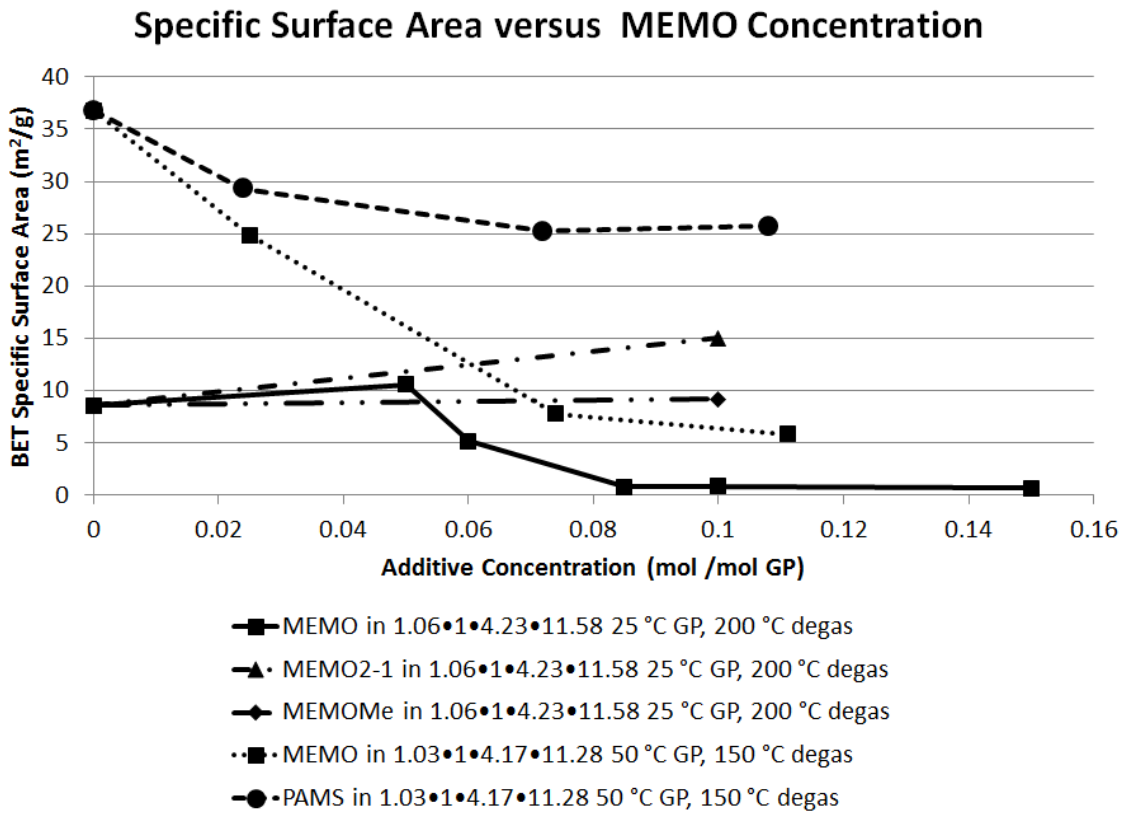

Figure 6.5. BET specific surface area as a function of alkoxysilane additive concentration in Formulation A geopolymers. The addition of MEMO clearly causes decreased specific surface area. After the addition of a critical amount of MEMO additive (approximately 0.06 mol/mol) further additive causes substantial microstructural change, echoing the shrinkage results.

change in SSA than did similar quantities of MEMO. NLDFT results shown in Figure 6.6 demonstrate that mesopores between 5 nm and 20 nm were reduced by approximately an order of magnitude above the critical concentration of 0.06 mol MEMO/mol GP.

This result suggests a substantial integration of precipitates, as pores of this size range are typically considered to be the voids that separate incompletely unified precipitates[55; 56], while smaller pores represent precipitate roughness. TEM micrographs of precipitate aggregates appear to reflect this hypothesis, showing a qualitatively smooth surface (Figure 6.7(a)) with

structural features of a much larger length scale (Figure 6.7(b)) than was observed in micrographs of controls observed here and elsewhere[16]. It is not clear from TEM imaging whether any organic material was bonded within precipitates and/or aggregates.

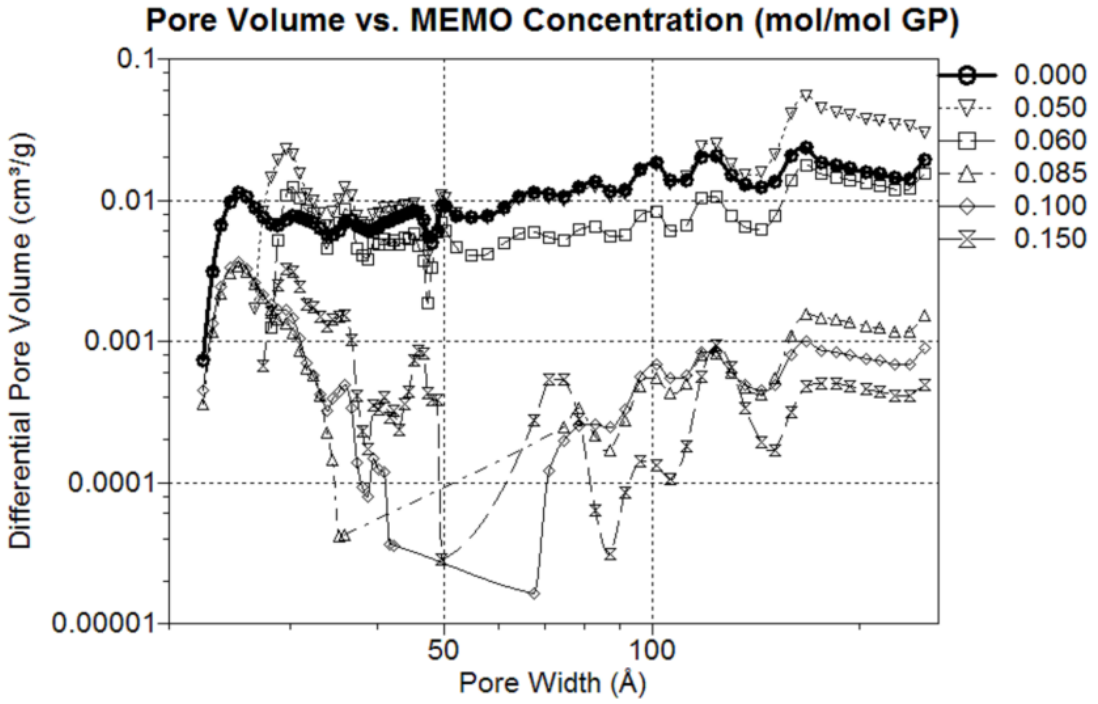

Figure 6.6. NLDFT modeling of mesoporosity from nitrogen adsorption results, as a function of MEMO concentration. Mesopores above approximately 5 nm are substantially eliminated when more than 0.06 mol MEMO/mol GP is added. The data are quite noisy due to the tiny amounts of porosity observed at this length scale.

Instead, the organic material formed a separate phase of tube-like structures on the order of 10s of nm in diameter and 100s of nm long (Figures 6.7(b-d)). These structures appear to be imbedded within the geopolymer aggregates and clearly bonded some geopolymer material strongly enough to survive drying and vacuum. A substantial number of tubes were found to be

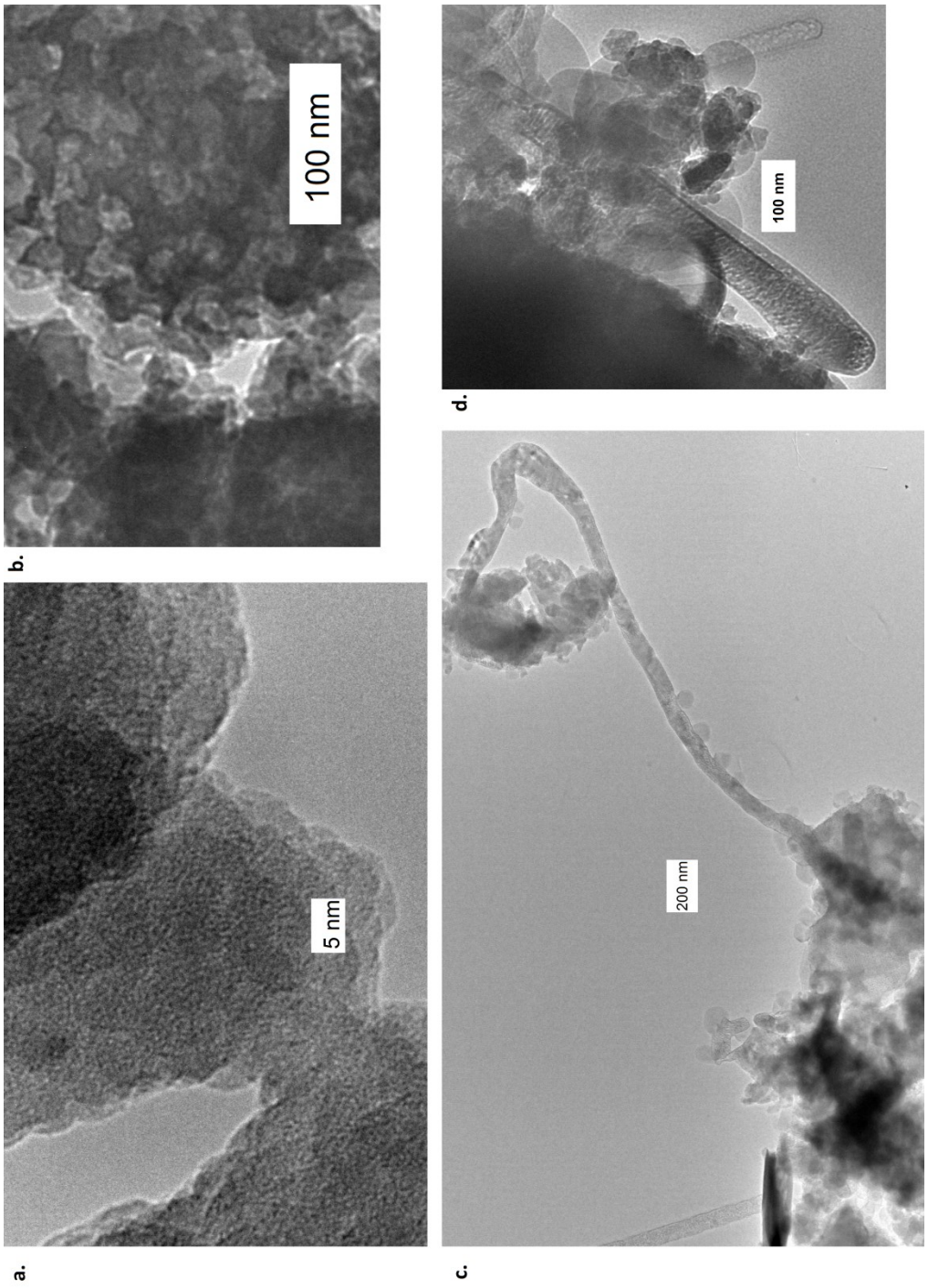

Figure 6.7. Transmission electron micrographs of a Formulation A geopolymer with 0.1 mol MEMO/mol GP. The precipitates are seen to be less jagged than unmodified geopolymers (a). Large mesopores are visible within some agglomerates (b). The organic material forms easily distinguishable tube structures that in some cases connect agglomerates (c) and are encapsulated within agglomerates (d).

completely detached from the geopolymer, either removed during grinding to powder or during evacuation of the sample.

(5) Mechanism

These microstructural and property alterations imply a significant modification of the geopolymer chemistry, which in turn suggests substantial room for manipulation and property improvement. In particular, there exist substantial similarities between this system and an organic hydrogel system, including the predominance of cross-linked sodium methacrylate as waterlocking agents. Previous investigations of these materials have demonstrated increased hydrogel-forming capability with increased structure size, as measured mass per mass[165]. In accordance with previous geopolymer research, the drying shrinkage results suggest a system in which insufficient water existed to preserve hydration spheres around the cations. In this case, the addition of the MEMO additive would be expected to greatly increase the hydration radius of the cations through the formation of sodium methacrylate groups within the geopolymer. The densification observed is then directly a result of this process.

Gas adsorption results suggest that the mesoporous water in these modified geopolymers was waterlocked into pores at a length scale of approximately 40-100 nm. In contrast, the silane coupling agent tube structures occurred on a length scale of hundreds of nm in width and μm in length, implying that each tube affected many pores rather than forming a single massive film encapsulating a single large pore. This is consistent with the TEM observation that some geopolymer material appeared to be trapped within the tubes, and that SEM images showed some curled structures at the surface of the cut cross-section. It is possible that within the geopolymer matrix some portion of the organic material formed membranes or films. These

might have rolled up during drying when allowed freedom of movement, due to being exposed when the sample was cut. Evidence of multi-walled tubes in some of the images supports this theory.

Thus, the available evidence suggests that during the condensation and gelling stage, the organic material existed in membranes, which both attached to some geopolymer precipitates and bound significant amounts of the free water. This in turn depleted much of the free water elsewhere, resulting in reduced 5-20 nm porosity. This is consistent with the observation that geopolymer mesoporosity is typically attributed to surplus free water[59,73,74]. The pores which did form in this system were observed to be only 1-5 nm in diameter, and could have been formed with water released from the geopolymerization condensation reaction itself. This water appeared very late in the reaction process, and was presumably isolated from the organic membranes by the geopolymer network. It was thus impractical to remove this water and its porosity, but the mesoporosity removed nevertheless increases the potential use of geopolymers considerably.

CHAPTER 7

DEVELOPMENT OF HIGHLY POROUS MONOLITHS

This chapter partially consists of material submitted for publication[††] and in preparation for publication[‡‡].

The value of porosity control in geopolymers is almost self-evident, as pore volume and pore size distribution dictate the mechanical properties of cementitious materials more than does perhaps any other microstructural feature. The previous chapter considered using hydrophilic alkoxysilanes to decrease porosity without sacrificing workability, using a different mechanism than cementitious water reducers such as polycarboxylate ether (ADVA series, W. R. Grace and Co., Colombia, MD). There are also benefits to maximizing porosity. Highly porous materials provide value in such uses as insulation, catalysis and filtration. Each of these products demands different pore characteristics, including varying pore size and pore interconnectivity.

While numerous methods of synthesizing porous ceramics exist, only minimal investigation has been conducted for porous geopolymers, and the methods attempted did not create an open porous network suitable for filtration. Here is presented one method of creating a percolating geopolymer network with pores in the size range of 100 nm-1 μm.

7.1. Background Information

For these purposes, a 'pore' is defined as a gas-filled, liquid-filled or fully drainable volume within a monolith ceramic sample from which the ceramic material is ultimately

[††] B. E. Glad and W. M. Kriven, "Geopolymer Porosity Control Using Surface Modification and Templating," The 10th Pacific Rim Conference on Ceramic and Glass Technology, San Diego, CA, (June 3, 2013).

[‡‡] B. E. Glad and W. M. Kriven, "Geopolymer Porosity Control Using Surface Modification and Templating," J. Am. Ceram. Soc., (2013), in preparation.

excluded. It can be open to the exterior of the monolith, or closed and sealed completely from the exterior. It can be connected through 'throats' to other pores to create a 'porous network', or fully encased by ceramic as an isolated pore.

Obviously, for a filter, a porous network of open pores of precise sizes (chosen for efficient flow of filtrate and retention of filtrand) is mandatory. For a catalyst support, issues of pore size dominate, as the open surface area is roughly proportional to the amount of accessible catalyst. Smaller pores offer the greatest possible surface area, up to 1000-3000 m^2/g or more for some microporous materials[173]. For an insulating ceramic, closed and isolated 'cellular' pores are best, inhibiting convection.

7.1.1. Theory of Pore Creation and Survival

In ceramics, the concept of pore synthesis is quite straightforward and ultimately occurs from two distinct sources. The first occurs during sintering, where grain growth and prohibition of densification can combine to produce pores at grain boundaries. The second source is the presence of a removable second phase in the ceramic during curing or sintering. This latter method of pore formation through a removable template is the only one available for non-sintered materials such as geopolymers and cements. In geopolymers, one useful second phase available by default is free water[59,73,74], which is responsible for porosity in existing geopolymers.

For fired ceramics, a variety of templates can be used, including polymer foams, which are burned off along with the binder, where the material leaves in the gaseous phase. In addition to the obvious negative image that can be made through burning off the second phase, a positive can be formed through this method[174]. Through use of a polymer readily wetted by the slurry, a

thin green body coating on the polymer foam struts can be created that, when fired, preserves a positive image of the foam.

For geopolymers, heating to high temperatures produces either a crystal or a glass depending on the formulation. The intrinsic value in this conversion will be discussed later in the chapter. However, it was a priority to develop porous unfired geopolymer structures. Thus, candidate materials included liquid polymers, other liquids and gasses. Equation 7-1 highlights that the typical geopolymer mesoporosity is too small[14,41,59,73,74] to be easily drained without damaging the sample with Young-Laplace capillary forces. These forces could be sufficient to affect the microstructure (where ΔP represents the additional pressure caused by the capillary forces, γ the surface energy and $R_{1,2}$ the principal pore radii of curvature):

$$\Delta P = \gamma\left(\frac{1}{R_1}+\frac{1}{R_2}\right), R_{1,2} \approx 10\ nm$$
$$\Delta P_{water} \approx 14\ MPa \tag{7-1}$$

Recent work has explored intensively the effect of water content on porosity, and demonstrated porosity control over a limited range[14] using water content manipulation.

Non-wetting liquids, such as many short-chain polymers, should leave an open pore network spontaneously according to the Washburn equation[129], although such departure is usually incomplete due to liquid being trapped at sudden constrictions[125]. However, in a geopolymer system, such non-wetting liquids are inevitably displaced by the water required for synthesis, due to the hydrophilic nature of the geopolymer surface. Gas-filled pores at ambient pressure can be considered empty for practical purposes even if fully closed, but gasses at elevated pressures (such as during supercritical drying) still require an open pore network to

equilibrate with ambient pressures. Gaseous templating eliminates the difficulty of capillary forces, but introduces its own complications (see below).

7.1.2. Comparative Systems

A number of widely used existing systems for the manufacture of porous ceramic structures exist, but none is fully applicable to this work. However, their consideration provides context for the investigation. For reasons mentioned above, open macropores on the scale of tens of micrometers or larger are easier to synthesize than smaller open pores. In particular, two very simple methods of producing porosity are commonly used in cements and have been duplicated in geopolymers.

A successful porous structure was created through hydrogen evolution[9,10,12,25,75] via the addition of elemental aluminum (resulting in the formation of alkali aluminum hydroxides and hydrogen in the presence of strong base), although pressure in closed pores was a concern. Oxygen evolution was also found to be possible, starting from liquid peroxide[9]. This lab's initial investigation of carbon dioxide evolution from carbonates did not produce a highly porous monolith, however. Air entrainment of geopolymer proves to be quite straightforward due to the precursor being a viscous slurry, and has been demonstrated elsewhere[45] and in this lab using a variety of surfactants. However, these two methods rely on gas bubbles to form and thus cannot produce pores smaller than a minimum diameter (see below).

For smaller diameter pores, creation of the aerogel[175] through sol-gel synthesis is well-known. In that synthesis, the wet gel is brought to a temperature and pressure where the liquid (or solvent-exchanged liquid) is supercritical, allowing it to change to a gas without evaporation.

This supercritical drying avoids both damage from capillary forces and damage from evaporating liquid.

Much effort has been invested in finding an alternative route to aerogel structures without the expensive supercritical drying. Upon drying, gels collapse, fracture or have methods to prevent capillary forces from destroying them. In the latter case, the resultant xerogel monolith both utilizes solvent exchange and hydrophobic surface modification[176]. Thus, the surface tension driving force then acts in favor of drying, resulting in a system where fluid is expelled rather than dried, with minimal resulting drying failure.

7.2. Entrainment-Based Porosity

Based on well-known techniques for cementitious materials (such as described in ASTM C260), air entrainment of geopolymers is a simple and practical method of making highly macroporous monoliths[45]. Surfactants or 'air entrainment agents' can be easily added to the hydrophilic slurry, and then the geopolymer has air mechanically introduced in exactly the same matter as for a freeze-thaw resistant concrete. The microstructure of such entrained geopolymers has been investigated elsewhere[7].

7.2.1. Entrainment Results

With a standard geopolymer (Formulation B), and the addition of reasonable amounts (1.0 wt%) of a straightforward surfactant such as sodium dodecanoate (CH_3-$(CH_2)_{10}$-COONa, (Sigma-Aldrich Co., LLC, St. Louis, MO), it was verified here that a highly porous geopolymer could be made, using a high-shear mixer as the mechanical driver for entrainment. The pores were approximately 2 mm in diameter, and could thus be observed by eye. Far more surfactant

was used in these syntheses than is typical for an equivalent concrete system[177], possibly contributing to the abnormally large pore sizes observed.

7.2.2. Minimum Pore Size Theory

The minimum pore size created through air entrainment is effectively the size of the smallest air bubbles trapped in the slurry. Unfortunately, the time-dependent dynamics of bubble size are quite complex and the literature is littered with attempts to fully analyze air-fluid bubble systems. It is well understood that bubble sizes change over time due to a combination of coalescence and pressure-driven gas diffusion[178,179].

In general, for a stagnant, viscous system such as the geopolymer slurry, coalescence effects will be minimal due to the relative absence of either turbulent or buoyancy-driven bubble movement[178]. A coalescence event requires increasing the proximity of a given pair of bubbles over time, and movement after mixing is limited in a setting geopolymer. Thus, the minimum pore size can be inferred from consideration of the kinetics of pressure-driven gas diffusion. The pressure difference ΔP between a bubble and its surroundings can be related to interfacial energy γ and diameter d with a free energy balance[152], as shown in Equations 7.2 and 7.3. E_b is the free energy of the bubble system.

$$-\Delta P * \frac{\pi d^3}{6} + \gamma \pi d^2 = E_b \tag{7.2}$$

$$\frac{dE_b}{dd} = 0 \rightarrow \frac{4\gamma}{d} = \Delta P \tag{7.3}$$

However, as this pressure gradient increases, the diffusion rate of the gas out of the bubble must increase. For the bubble to survive, it must receive gas from the environment at the

same rate or more than the amount it emits. Net flow can be approximated by Equation 7.4 (neglecting buoyancy effects, and where K is a constant of proportionality, n is the quantity of gas in moles, R is the gas constant, T is the system temperature and t is in units of time).

$$\frac{-dn}{dt} = K\Delta P * \pi d^2 - G(t) = K * \frac{6nRT}{d} - g(t), \qquad g(t) \approx G \tag{7.4}$$

Here g(t) represents the gas gain from the environment, and over short timescales is approximately a constant G, relating to the overall loss of gas from all the bubbles in the sample. This analysis is sufficient to show the equilibrium bubble diameter's dependence on enclosed mass, but the differential equation in total gas mass n illustrates clearly that bubbles of smaller than equilibrium radius will preferentially lose mass until they disappear[77]. It is thus qualitatively observable that the minimum bubble diameter depends ultimately on liquid-vapor interfacial energy, which can be reduced but not eliminated using surfactants.

7.3. Titration-Driven Precipitation

It is not practical to reduce liquid-vapor surface energy to near zero. However, reducing the surface energy of a liquid-liquid interface is possible[101,180], and drying such a system can produce a xerogel (gel dried under ambient conditions) or aerogel (gel dried under supercritical conditions). Many acid-based aluminosilicate xerogels and aerogels have been synthesized[181]. Such work was reproduced here in a system using metakaolin (22.80 g), sodium hydroxide (8.00 g) and DI water (18.00 g). The addition of silica fume (12.0 g) along with nitric acid (12.6 g) and excess hexane resulted in a mesoporous solid precipitate. This 1•1•4•41 geopolymer system demonstrated increased mesoporosity versus a traditional geopolymer (BJH desorption pore volume increased to 0.196 cm^3/g, BET specific surface area increased to 90.5 m^2/g) but the

system was not suitable for an insulating monolith as the material was extremely friable. This method was not investigated in detail due to the comparative resilience of the emulsion-template systems discussed below, and the significantly higher porosities achieved by them.

7.4. Emulsion-Template Systems

As discussed above, it is very difficult to extend the mesoporous system to extremely high porosities. Furthermore, the synthesis of macropores of the size 100 nm to 1 μm has not been extensively explored in geopolymeric materials or indeed many inorganic, non-crystalline materials in general. At that length scale, it is likely that interface interactions dominate templating, rather than the charge-driven templating of traditional geopolymers and zeolites. It is well-known that interface-driven porous structures are trivial to synthesize in geopolymers through volume exclusion, using air entrainment or gas evolution, but the problem is that these excluded volumes are unstable and ripen to a size of many micrometers on timescales orders of magnitude shorter than the hours required to cure a geopolymer even at elevated temperature.

This observation has driven this investigation toward the use of highly stabilized oil-in-water emulsions. Aluminosilicate condensation appears to occur in these systems as readily as in typical geopolymer systems. However, like a normal geopolymer, it is difficult to maintain pores of a micrometer or less during drying and rewetting due to capillary forces. The solution to this difficulty has been to produce a hydrophobic organic covering or veil on the pore interiors using a chemical such as dimethyldiethoxysilane (DIDE) [$(CH_3)_2(OCH_2CH_3)_2Si$] capable of condensing both as a polymer chain and with the growing geopolymer network (as shown in Figure 7.1).

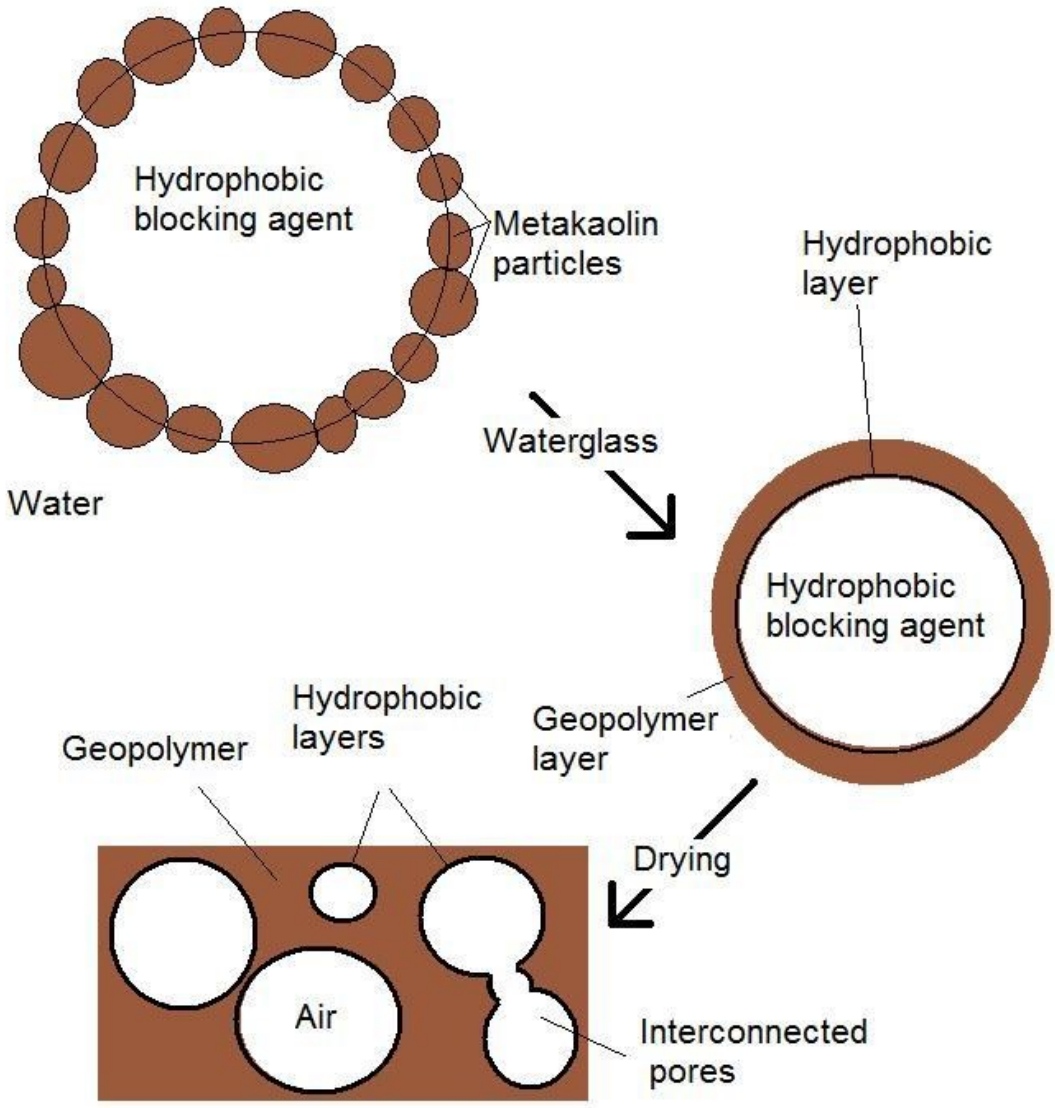

Figure 7.1. The mechanism used for creation of highly porous, 1 μm diameter pore geopolymers. Pore interconnectivity results from the draining of these pores, when water must find a route to the surface.

7.4.1. Experimental

The objective of this effort was to combine the sol-gel synthesis of the hydrophobic alkoxysilane with the straightforward precipitation of geopolymers. The ability for geopolymers to react around a range of organic materials makes this approach especially attractive. As a

hydrophobic coating reduces but does not eliminate drying stresses, a relatively gentle, slow geopolymer curing method was expected to be necessary. Accordingly, the evaporative method described in Chapter 4 was developed for this purpose.

(1) Synthesis

Sodium silicate solution (waterglass) was prepared as follows: 160.0 g sodium hydroxide (Sigma-Aldrich Co., LLC, St. Louis, MO) was added to 360.0 g DI water in a stainless steel container and stirred using a polytetrafluoroethane stir bar with a magnetic stir plate until fully dissolved. The container was then sealed with polyethylene terephthalate plastic film, and the temperature of the stir plate was set to approximately 45 ºC. A total of 240.0 g fumed silica (Cab-o-sil LM-150D, Cabot Corp., Boston, MA) was then added in small batches of approximately 10 g, each time allowing for complete or almost complete dissolution of the silica before adding the next batch, with the container remaining sealed when not adding silica. After all silica was added, the container was resealed and the contents were allowed to stir at the elevated temperature for 24 hours. After 24 hours, the solution of sodium silicate was poured into a polyethylene container, and allowed to equilibrate at ambient conditions for at least two weeks.

A mixture of 2.78 g metakaolin (Metamax EF, median particle size[117] 2.7 μm, Engelhard Corp., Iselin, NJ), 4.75 g waterglass, and a great excess of water (typically 197 mol/mol GP) was used to make each sample. Various hydrophobic monomer additives (Table 7.1) provided the excluded volume to template porosity. Formulations D and E were used as described below. Unless specified otherwise below, 4.94 g DIDE was used in each experiment, equivalent to 2.67 mol of additive per mol geopolymer. For the other reagents, the same molar ratio was used.

For Formulation D (non-premixed samples), the mass of 2.78 g Metamax EF was placed in a polypropylene container (Solo Cup Co., Lake Forest, IL) with a quantity of water (usually 40.0 g or as specified) and some additives. This mixture was then ultrasonicated for 9 minutes at 240 watts while being stirred on a stir plate. Then 4.75 g waterglass was added dropwise as quickly as possible, while ultrasonication continued for a further 6 minutes (a total of 15 minutes). This resulting dilute slurry had nominal composition 1•1•4.0•z before additives (z=197 for 40.0 g, or as specified), but some water and some additives evaporated during the mixing. The resulting mixture was placed in the controlled humidity chamber (at a specified humidity) or in a sealed container with a large excess of calcium sulfate (Drierite, W. A. Hammond Co., Xenia, OH), and maintained at 25 ºC until weighing indicated substantially no mass loss over a period of hours. Depending primarily on initial water content and humidity, this process required between 3 days and 3 weeks, but in most cases drying was completed in approximately 1 week or less.

For Formulation E (premixed samples), a mass of 10.00 g Metamax EF was placed in a high density polyethylene container (Thinky Corp., Tokyo) with 30.0 g water and 0.40 ± 0.03 g 40 wt% poly(ammonium methyl acrylate) solution (Darvan 821A, R. T. Vanderbilt Co., St. Norwalk, CN) and 16.67 g waterglass. The resulting thick slurry (of composition 1•1•3.9•50.0 before additives) was sealed, and stirred with a magnetic stir bar for seven days to create the premix. After seven days had passed, an amount of premix equivalent to 0.012 mol geopolymer was removed from the premix (15.72 g), placed in a polypropylene container (Solo Cup. Co.), diluted to 1•1•3.9•197, and any additives were included at this time. The mixture was then ultrasonicated for 8 minutes at 240 watts while being stirred on a stir plate, and placed in the controlled humidity chamber or in a sealed container with a large excess of calcium sulfate

(Drierite) and maintained at 25 °C until weighing indicated substantially no mass loss over a period of hours. Depending primarily on initial water content and humidity, this process required between 3 days and 3 weeks, but in most cases drying was completed in approximately 1 week or less.

Powdered samples for characterization were generated by dry grinding in an alumina mortar, and were collected after being passed through a 44 μm mesh.

(2) Microstructural Characterization

Electron microscopy was used to provide a qualitative description of the microstructure. SEM micrographs were captured on a JEOL 6060LV (JEOL USA, Inc., Peabody, MA) with a beam energy of 25 kV. Samples were cut with a diamond-edged wafering blade with cutting oil and sputter-coated with a gold-palladium target to a depth of 10 nm. TEM micrographs were obtained on powder samples placed on a carbon film. Samples were imaged at room temperature using an excitation voltage of 200 kV and a lanthanum hexaboride filament (JEOL 2010, JEOL USA, Inc., Peabody, MA). Care was taken to minimize TEM beam exposure until immediately prior to image capture.

(3) Reactivity Characterization

Cu-Kα X-ray powder diffraction (XRD) testing was conducted with a Siemens-Bruker D5000 diffractometer. Tests were conducted at 40 kV, 30 mA, a step size of 0.025° 2-theta, and a measurement time of 6 seconds/step. Diffusion reflection infrared spectra were taken using a Nicolet Nexus 670 spectrometer on powdered samples mixed with KBr (1:19 wt ratio).

Differential scanning calorimetry data were acquired at a rate of 1 °C/min from room temperature to 400 °C, and then immediately continued from 400 °C to 1100 °C at 5 °C/min. The testing chamber (STA 409 CD, Netzsch Group, Burlington, MA) was a continuous airflow chamber and the gasses used were Ultra Zero Air and UHP Helium at a 15:8 volume ratio, which is a typical ratio with helium used to prevent damage to the instrument.

(4) Porosity Characterization

Nitrogen adsorption porosimetry was conducted on powder samples using a ASAP 2020 porosimeter (Micromeritics Instrument Corp., Norcross, GA). The samples were evacuated at 90 ºC, and then degassed at 150 ºC for 4 hours. If mass loss during analysis or other anomalies were observed, then the samples would subsequently be degassed at 250 ºC or even 350 ºC. In such cases, Chapter 5 results showed that nitrogen porosimetry results reflect phase morphology changes due to degassing at the elevated temperature, and consequently the results have reduced value. This heating was necessary as the samples produced with DIDE and/or some alkane (hexane or dodecane) were not easily prepared using gentler methods. For these samples, degassing at 150 ºC for 4 hours up to several days did not result in satisfactory removal of volatiles. Thus, it was found that increased temperature was required to accurately take measurements, with the result that microstructural changes were inevitable.

Mercury intrusion porosimetry was conducted using a porosimeter (Autopore II 9220, Micromeritics Instrument Corp., Norcross, GA) and quadruple-distilled mercury (Bethlehem Apparatus, Hellertown, PA). Data were collected at a 0.001 $\mu Lg^{-1}s^{-1}$ equilibrium. Single-intrusion data was measured to provide information on the total porosity and the critical intrusion diameter. The modified PDC-MIP method (Chapter 5) was also used to gain additional

information about pore size distribution. The contact angle of geopolymer was estimated using mercury intrusion porosimetry on a Formulation A geopolymer prepared with slits cut with a diamond-edge wafering blade and optically measured. This technique was used to verify that the contact angle of 130º previously referenced in the literature[182,183] was appropriate. Using that method, a Tadmor equilibrium contact angle[184] of 135° was calculated, which was considered close enough to the literature value that the convention of 130° was used.

7.4.2. Results

Formulations D and E were able to create highly porous monoliths when a dialkoxysilane was an additive, but other alkoxysilane additives either phase separated or produced only dense geopolymer (Table 7.1). DIDE was found to be the most successful additive, and further characterization was conducted on DIDE-based systems.

(1) Porosity

The use of the silicone additives clearly allows for the creation of highly porous bodies. Unfortunately the pore size, as measured using the theoretical 16% percolation critical value[112], increased dramatically with increasing porosity. Over the range of 70-90% porosity, the critical pore size would increase from ≈1 μm to ≈30 μm or more. Beyond the addition of the DIDE silane and hydrophobic phase (Table 7.2), porosity volume was largely controlled by a combination of initial water concentration (Table 7.3) and humidity conditions (Table 7.4). Assuming an approximately constant evaporation rate for a given humidity, the results suggest that water residence time greatly affected both total pore volume and pore size.

Table 7.1. List of hydrophobic reagents considered	
Name	Result
Tetraethoxysilane	Phase separation into translucent sol-gel solid
Methyltriethoxysilane	Phase separation into translucent sol-gel solid
Dimethyldiethoxysilane (DIDE)	Useful template
Trimethylethoxysilane	Dense solid with minimal additional porosity
Tetramethylsilane	Dense solid with minimal additional porosity, used as control
Hexane	Dense solid with minimal additional porosity
Dodecane	Dense solid with minimal additional porosity, with persistent oil film prohibiting evaporative drying
Dimethyldimethoxysilane	Similar results to DIDE
Diphenyldimethoxysilane	Similar results to DIDE

Table 7.2. Effect of hydrophobe content on Formulation D GP, composition 1•1•4•x, with molar ratio 1 Na_2O•y $C_{12}H_{26}$•2.67 $Me_2Si(OEt)_2$						
Sample (mol dodecane/ mol GP) [y]	244 mol water/mol GP [x]			476 mol water/mol GP [x]		
	Critical Percolation Pore Size ($D_{16\%}$) (μm)	Density (g/cm^3)	Porosity (cm^3/cm^3)	Critical Percolation Pore Size ($D_{16\%}$) (μm)	Density (g/cm^3)	Porosity (cm^3/cm^3)
0.00	2.29	0.85	0.553	---		
1.00	7.26	0.38	(Saturation)	38.29	0.14	(Saturation)
2.00	---			33.20	0.15	0.8491

This systematic relationship between drying time and observed pore size suggests that phase ripening of the unstable colloid is likely to be the cause of this observation. Ethanol added specifically to destabilize the emulsion (Table 7.5) resulted in much larger pore sizes. Notably, the pore volume in the ethanol investigation was approximately stable, as expected with ethanol added immediately, but the density showed a marked decrease. This result implies that the ethanol had partially replaced water in the pores.

Table 7.3. Effect of initial water content on Formulation D GP, composition 1•1•4•x, with molar ratio 1 Na_2O•1 $C_{12}H_{26}$•2.67 $Me_2Si(OEt)_2$			
Sample (mol water/mol GP) [x]	Critical Percolation Pore Size ($D_{16\%}$) (μm)	Density (g/cm^3)	Porosity (cm^3/cm^3)
151	1.82	0.64	0.645
197	1.81	0.59	0.723
244	7.26	0.38	(Saturation)
476	38.29	0.14	(Saturation)

Table 7.4. Effect of humidity on Formulation D GP, composition 1•1•4•197, with molar ratio 1 Na_2O•1 $C_{12}H_{26}$•2.67 $Me_2Si(OEt)_2$)			
Relative humidity	Critical Percolation Pore Size ($D_{16\%}$) (μm)	Density (g/cm^3)	Porosity (cm^3/cm^3)
30%	0.623	1.00	0.319
70%	1.81	0.59	0.723
2 days 95%, then 25%	6.72	0.47	0.769

Table 7.5. Effect of destabilizing co-surfactant on Formulation D GP, composition 1•1•4•197, with molar ratio 1 Na_2O•1 $C_{12}H_{26}$•2.67 $Me_2Si(OEt)_2$)			
Sample (mol ethanol added/mol GP)	Critical Percolation Pore Size ($D_{16\%}$) (μm)	Density (g/cm^3)	Porosity (cm^3/cm^3)
None	1.81	0.59	0.723
1.75 immediately	17.31	0.44	0.743
1.75 after 24 hours	9.31	0.58	0.657

(2) Microstructure

Additional evidence for emulsion instability causing an increased pore size with drying time is visible in Figure 7.2. These approximately spherical macropores on the order of hundreds of μm appear only in samples with an extremely long drying time (19 days) due to curing at 95% humidity. Needle-like precipitates began to be visible with this drying time (Figure 7.3) while shorter drying times showed evidence of a uniform organic 'veil' or film over

the microstructure (Figures 7.4, 7.5). This contrast may indicate the formation of an organized zeolitic phase. Due to the inherent flexibility of the Si-O bond in the polymerized DIDE (polydimethylsiloxane) it is unlikely that the needle structure was composed of ordered organic material.

Surprisingly, TEM images showed results not dissimilar to a typical geopolymer, and no definite organic material could be identified. The premix geopolymer had loose tube structures reminiscent of those in Chapter 6, which were almost certainly the polyacrylate dispersant added to the premix. Nitrogen adsorption porosimetry results tended to suggest that mesoporosity was being reduced somewhat by the addition of the organic veil, although the considerable degassing required for these samples makes a quantitative interpretation questionable. This qualitative result was consistent with the SEM 'veil' or film observations creating a smoother nanostructure, but could also be the result of the high-temperature degassing artifacts discussed in Chapter 5.

Microstructural SEM analysis revealed that the addition of only hydrophobic material with no silicone blocking agent resulted in the formulation of a solid with small, tortuous pores (with templated porosity of only a few percent) as shown in Figure 7.6, while the samples with both a blocking agent and hydrophobic material possessed agglomerated structures on the scale of micrometers to hundreds of nanometers, surrounded by pores (Figures 7.4 and 7.5). Based on these observations, it is reasonable to conclude that the blocking agent DIDE successfully segregated the aqueous aluminosilicate phase from the hydrophobic phase, allowing drainage, and a high porosity.

Figure 7.7 and Table 7.6 show the aggregate composition-formulation-porosity data for DIDE samples. It appears that 0.8 mol DIDE/mol GP is sufficient to create a full hydrophobic film, and that additional DIDE has minimal effect on Formulation D samples. At higher

concentrations, total porosity decreased significantly while pore size decreases slightly. This suggests that the organic film on the interior pore surfaces is simply thickening. The trend is removed through calcination, which removes the organic film. The premixed Formulation E samples show a clearer trend than does the regular D samples, suggesting that the premixing more readily allows for thick hydrophobic film formation than does the regular Formulation D processing.

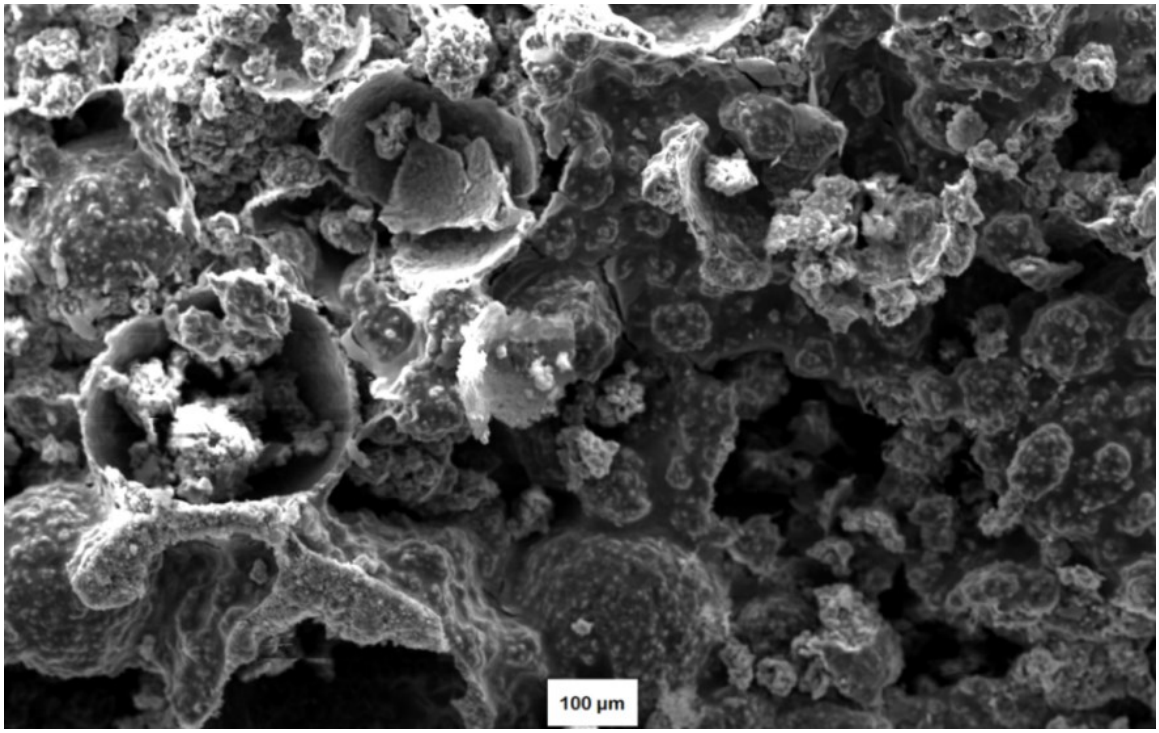

Figure 7.2. Scanning electron micrograph of Formulation D GP, composition 1•1•4•244, with molar ratio 1 Na_2O•2.67 $Me_2Si(OEt)_2$, cured at 95% relative humidity. Clearly visible are many large, hollow spherical structures, which are suspected to be the largest and most stable of the particle-stabilized emulsion beads.

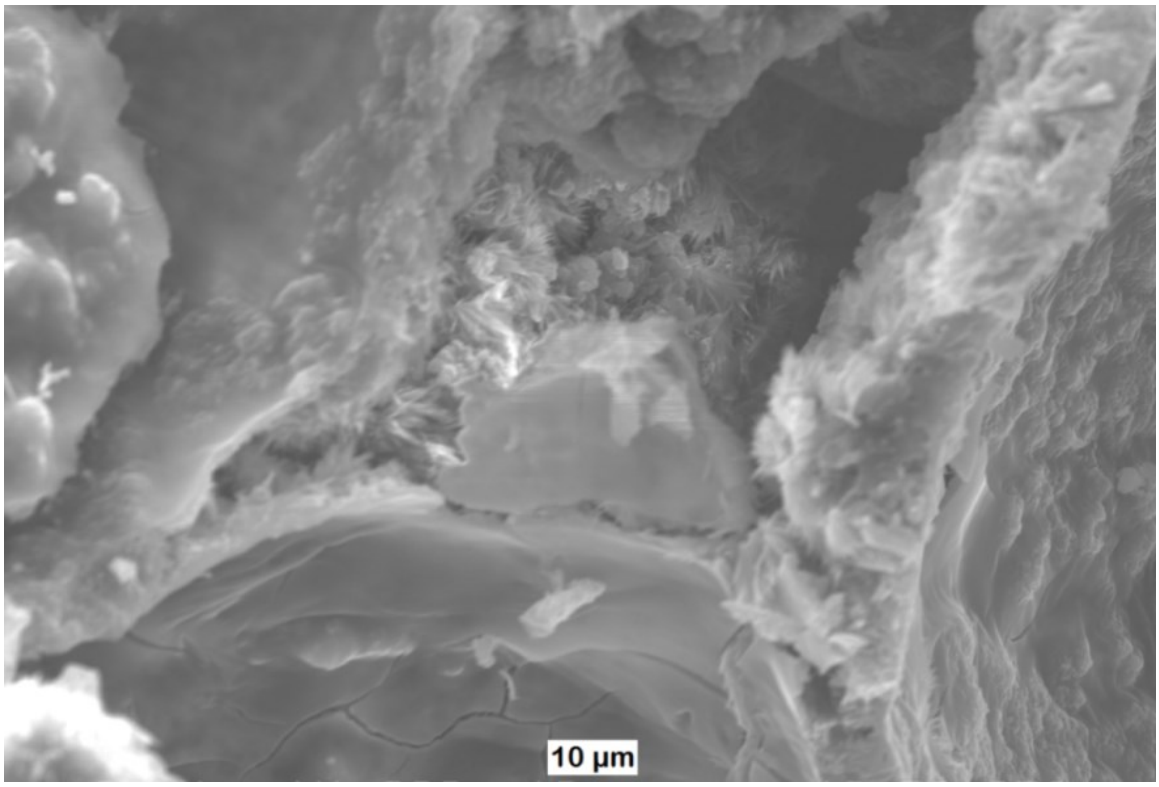

Figure 7.3. Scanning electron micrograph of Formulation D GP, composition 1•1•4•244, with molar ratio 1 Na_2O•2.67 $Me_2Si(OEt)_2$, cured at 95% relative humidity. The needle-like precipitates were not found in lower-humidity samples.

(3) Reactivity

The signature X-ray diffraction geopolymer shift from 22º 2-Θ to 28º 2-Θ was not in evidence. Although the very broad hump inherent in geopolymer samples makes precise evaluation difficult (see Chapter 4 for examples), it is likely that very little if any geopolymerization occurred in these samples. Based on the observation of the organic 'veils' or film coating the sample as well as the noticeable hydrophobicity of the dried monoliths, it is possible that the various hydrophobic phases (DIDE, dodecane) inhibited the interaction of the silicate and the metakaolin precursor. Using the premixing method described in Part 4, with the

organic second phase added along with the dilution, a shift to approximately 24º 2-Θ occurred. The evidence in Part 4 suggests that a more concentrated premix would cause a larger shift.

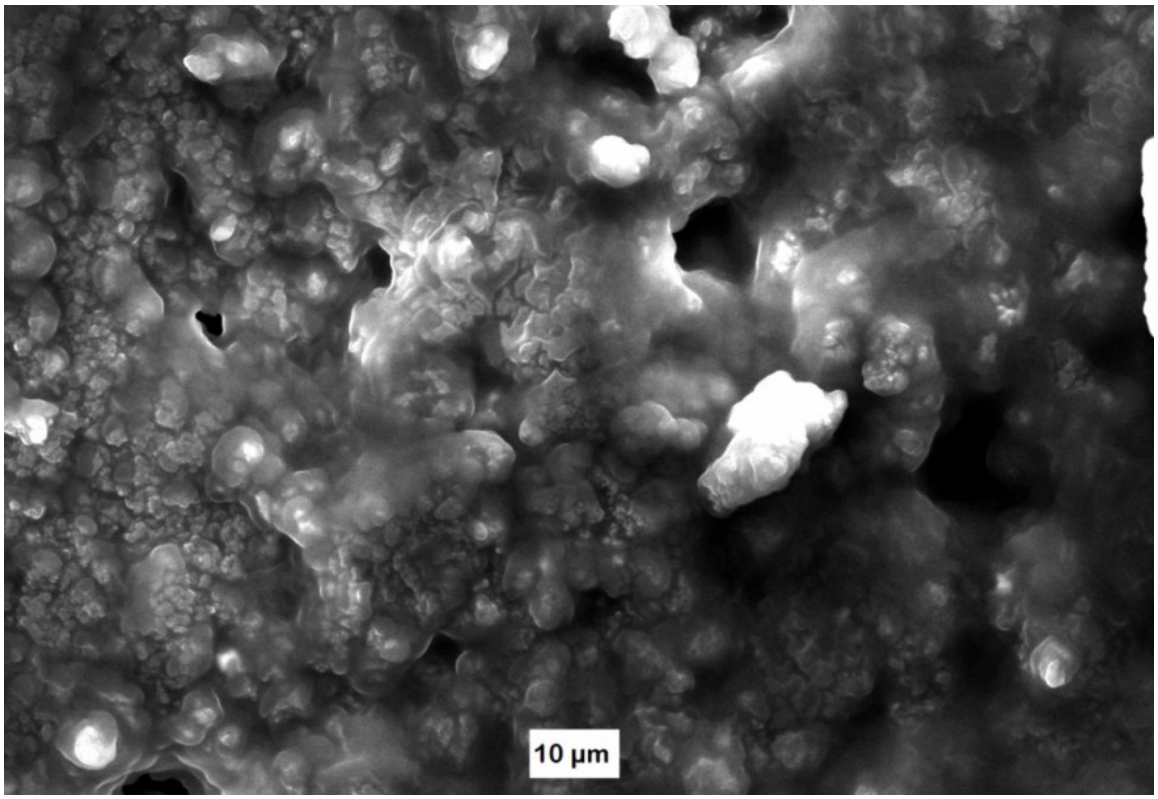

Figure 7.4. Scanning electron micrograph of Formulation D GP, composition 1•1•4•197, with molar ratio 1 Na_2O•1.00 $C_{12}H_{26}$•2.67 $Me_2Si(OEt)_2$, illustrating aluminosilicate structures coated with organic 'veils' or films.

Differential scanning calorimetry results showed the samples to lack the departure of free water over the range of 75 °C- 150 °C that is characteristic of geopolymers. Instead, a significant endotherm beginning at ≈280 °C was observed, and concurrent mass loss from that temperature up to ≈700 °C implies the loss of the organic material within that range. It would seem that while the efforts to exclude water from the porous structure were successful, the results

were marred by the lack of reactivity of the geopolymer and apparently substantial unreacted organic phase as well.

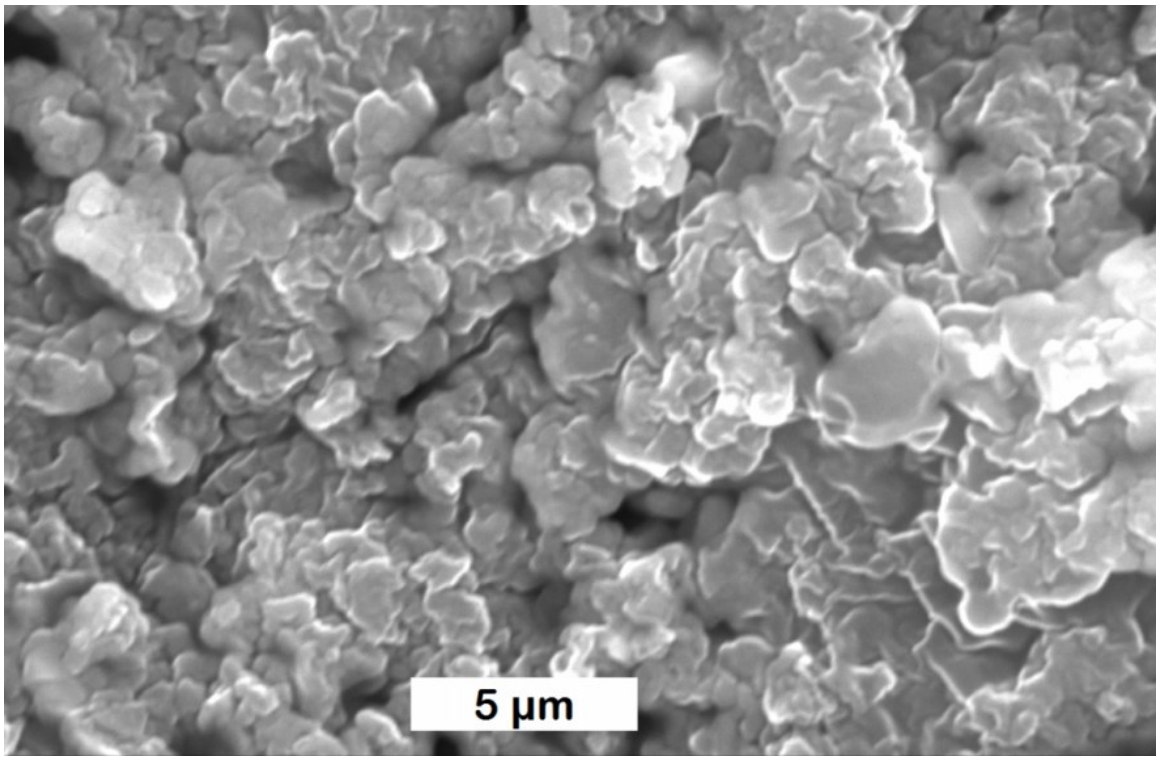

Figure 7.5. Scanning electron micrograph of Formulation D GP, composition 1•1•4•151, with molar ratio 1 Na_2O•1.00 $C_{12}H_{26}$•2.67 $Me_2Si(OEt)_2$). A moderately porous structure is evident, with the pores consisting of spaces between the aluminosilicate structures.

(4) Efficiency

A variety of samples with varying amounts of DIDE and a constant 2.15 g dodecane were calcined to 800 °C for 4 hours (with a 5 °C/min heating ramp) in a tube furnace using a continuous flow of argon as an inert gas, and the mass loss was recorded. By assuming that all of the organic material was destroyed in this calcination, it was possible to derive the amount of organic material lost prior to the calcination. From Figure 7.8, the high linear correlation implies that a proportion of DIDE (the slope) was lost before calcination, as was a constant amount of

material (the intercept, presumably dodecane lost before calcination). These data suggest that roughly half the DIDE and 80% of the dodecane were lost during evaporation. Hence, there is substantial room for efficiency gains and processing improvement.

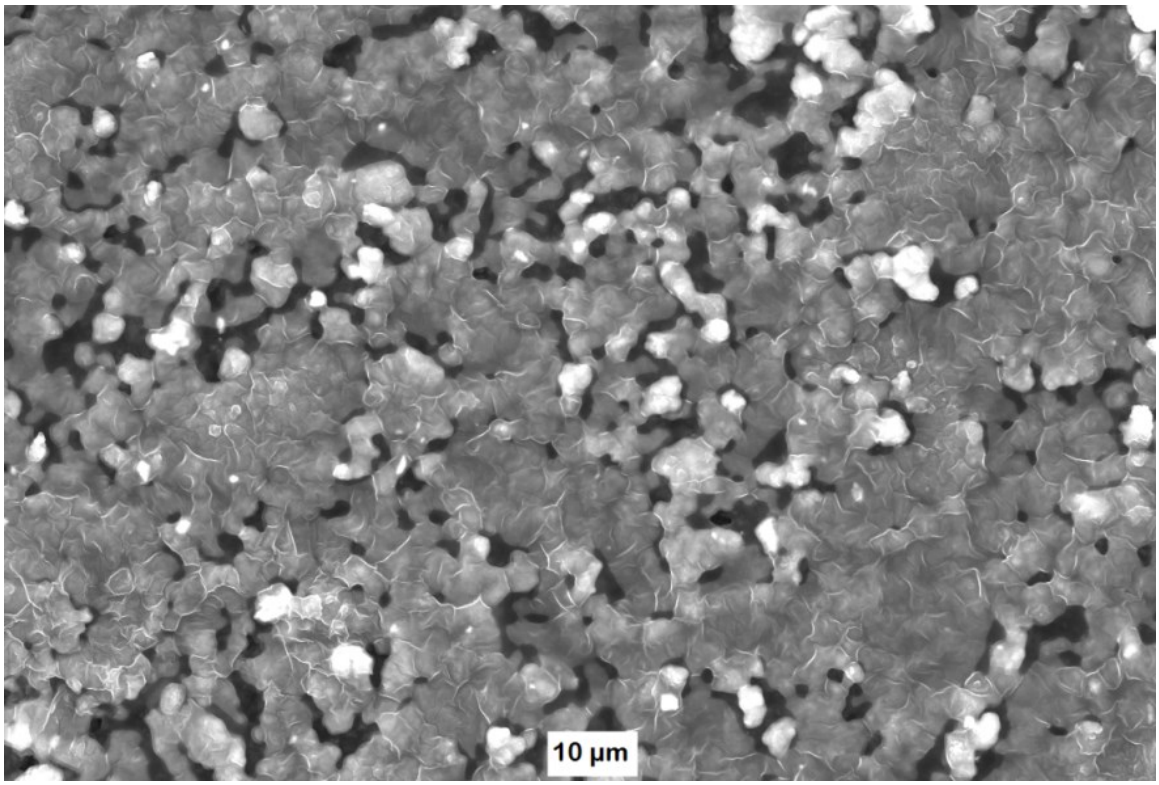

Figure 7.6. Scanning electron micrograph of Formulation D GP, composition 1•1•3.9•316, with molar ratio 1 Na_2O•3.63 C_6H_{14}. The sample was a solid with a network of tortuous pores on the scale of micrometers. MIP results demonstrate the interconnectivity of these pores, despite their discrete appearance.

7.5. Calcination of Monoliths

It was observed that porous samples approaching 80% porosity had weak mechanical strength and were friable. Thus, the possibility of calcining the geopolymer monolith to improve mechanical properties was investigated. It was found that calcination above approximately 500 ºC in an atmospheric environment resulted in the destruction of the monolith and a chaotic

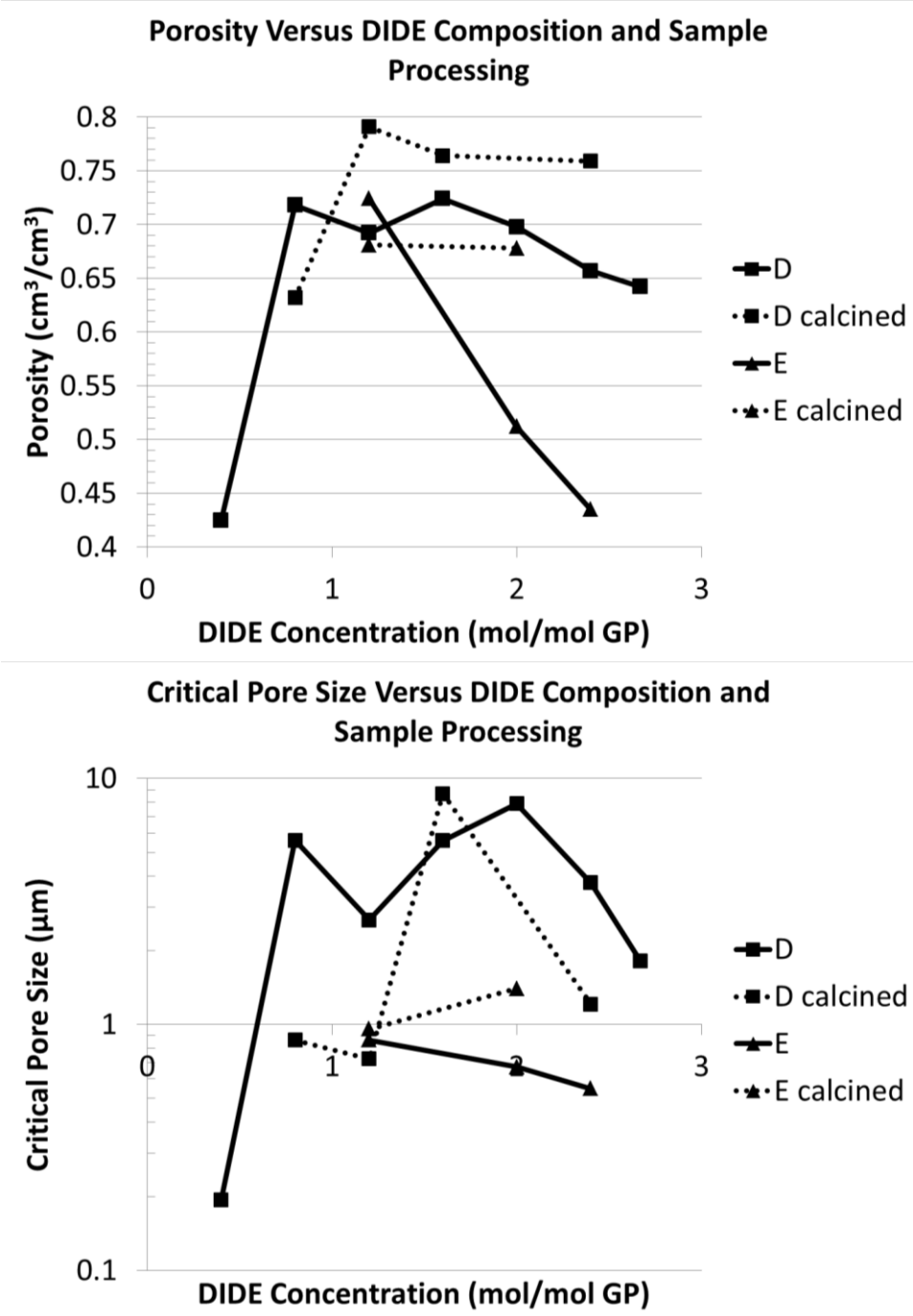

Figure 7.7. Porosity results as a function of initial DIDE content. After 0.8 mol DIDE/mol, further additive fails to increase porosity meaningfully. At higher concentrations, greatly reduced porosity and slightly reduced pore size suggests that the organic film is thickening on the interior surface of the pores, especially as the trend is reduced for calcined samples (800 °C, 4 h in Ar, 5°/min ramps).

organic mixture of polymer and char. Thus, failure appeared driven by combustion of the organic material.

Table 7.6. Effect of varying DIDE concentration. GP composition 1•1•4•197, with molar ratio 1 Na_2O•1 $C_{12}H_{26}$•z $Me_2Si(OEt)_2$. Cured at 70% humidity. Calcination conducted 800 °C, 4 h in Ar, 5°/min ramps.

DIDE Concentration (z mol/mol GP), Formulation	Critical Percolation Pore Size ($D_{16\%}$) (μm)	Density (g/cm^3)	Porosity (cm^3/cm^3)
0.40 D	0.194	1.36	0.425
0.80 D	5.61	0.65	0.718
0.80 D calcined	0.865	0.59	0.632
1.20 D	2.66	0.58	0.692
1.20 D calcined	0.725	0.51	0.791
1.60 D	5.59	0.76	0.724
1.60 D calcined	8.66	0.69	0.764
2.00 D	7.90	0.50	0.698
2.40 D	3.77	0.71	0.657
2.40 D calcined	1.21	0.62	0.759
2.67 D	1.81	0.71	0.642
1.20 E	0.864	0.60	0.724
1.20 E calcined	0.958	0.63	0.681
2.00 E	0.672	0.91	0.512
2.00 E calcined	1.40	0.69	0.678
2.40 E	0.548	1.10	0.435

This was confirmed with a sample calcined in a tube furnace, with a continuous flow of N_2. This calcination at 800 ºC for 4 hours (with a 5 ºC/min heating ramp) of a Formulation E sample (premix w=37.4, with 1 Na_2O•2.67 $Me_2Si(OEt)_2$) resulted in the preservation of the monolith. The calcination process was found to increase the porosity of the material substantially without greatly increasing the critical pore size, as shown in Figure 7.9. This glassy solid possessed much greater strength than did unfired monoliths of similar porosity. Similar

results were observed with the various samples calcined in argon at 800 ºC for 4 hours with a 5 ºC/min heating ramp (Figure 7.7, Table 7.6).

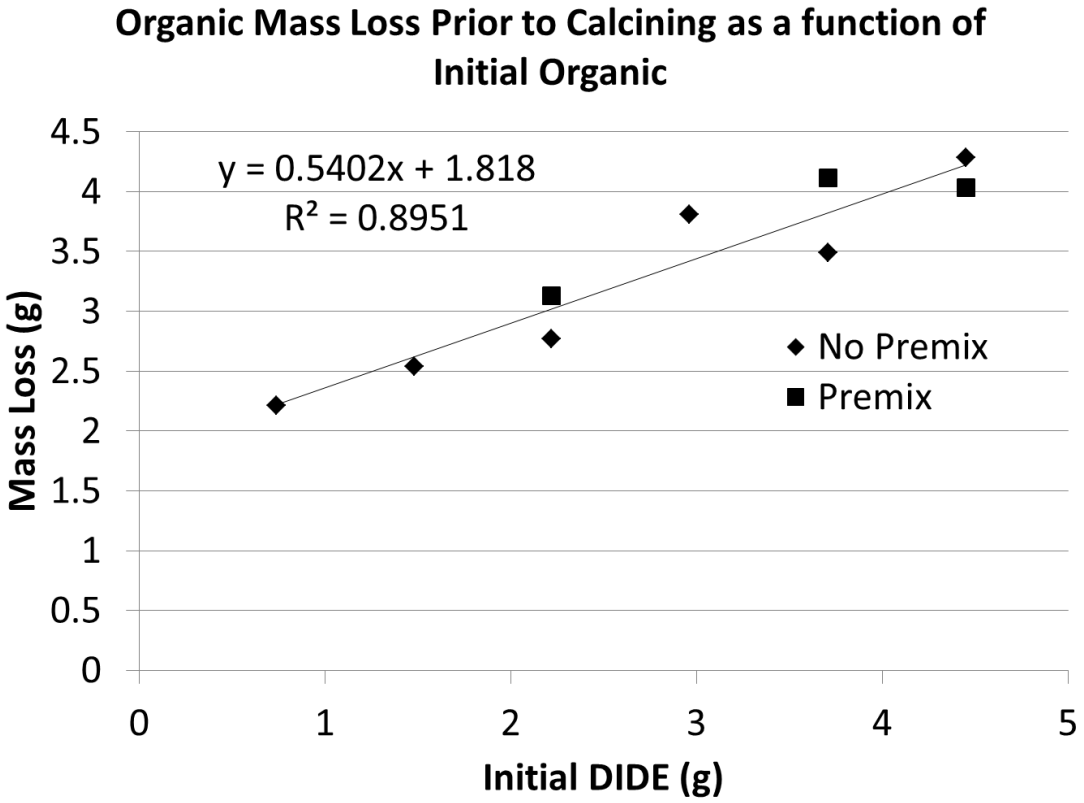

Figure 7.8. Plot of organic mass lost during processing as a function of initial DIDE concentration. A significant portion (≈54%) of the DIDE is not lost during calcination and is thus presumably lost at some earlier step. The intercept is presumed to be the amount of dodecane lost during processing and represents more than 80% of the original 2.15 g.

SEM imaging of the calcined sample revealed a chaotic structure of discrete domains, as seen in Figure 7.10. XRD data demonstrated that amorphous peak at 24º 2-Θ had been converted to a peak centered around ≈15º 2-Θ (Figure 7.11), implying the formulation of amorphous glass consistent with previous investigations of sodium geopolymer[15]. Nitrogen

adsorption porosimetry was complicated by the inability to reduce the monolith to an uncontaminated powder. It was observed that grains of the material easily scratched the dense alumina mortar and pestle, suggesting that some Si-CH_3 groups had been converted to a secondary phase of SiC. The presence of crystalline SiC was not observable with conventional X-ray diffraction but the (111), (220), (311), (222) and (400) ß-SiC peaks were clearly evident with synchrotron radiation diffraction. The absence of the (200) peak is common and suggests significant stacking faults[185].

The conversion of $SiCH_3$ structures to SiC upon calcination in inert atmosphere has been previously observed[186] and suggests increased mechanical properties as compared to porous aluminosilicates manufactured by other methods. This offers a variety of potential higher-value-added applications.

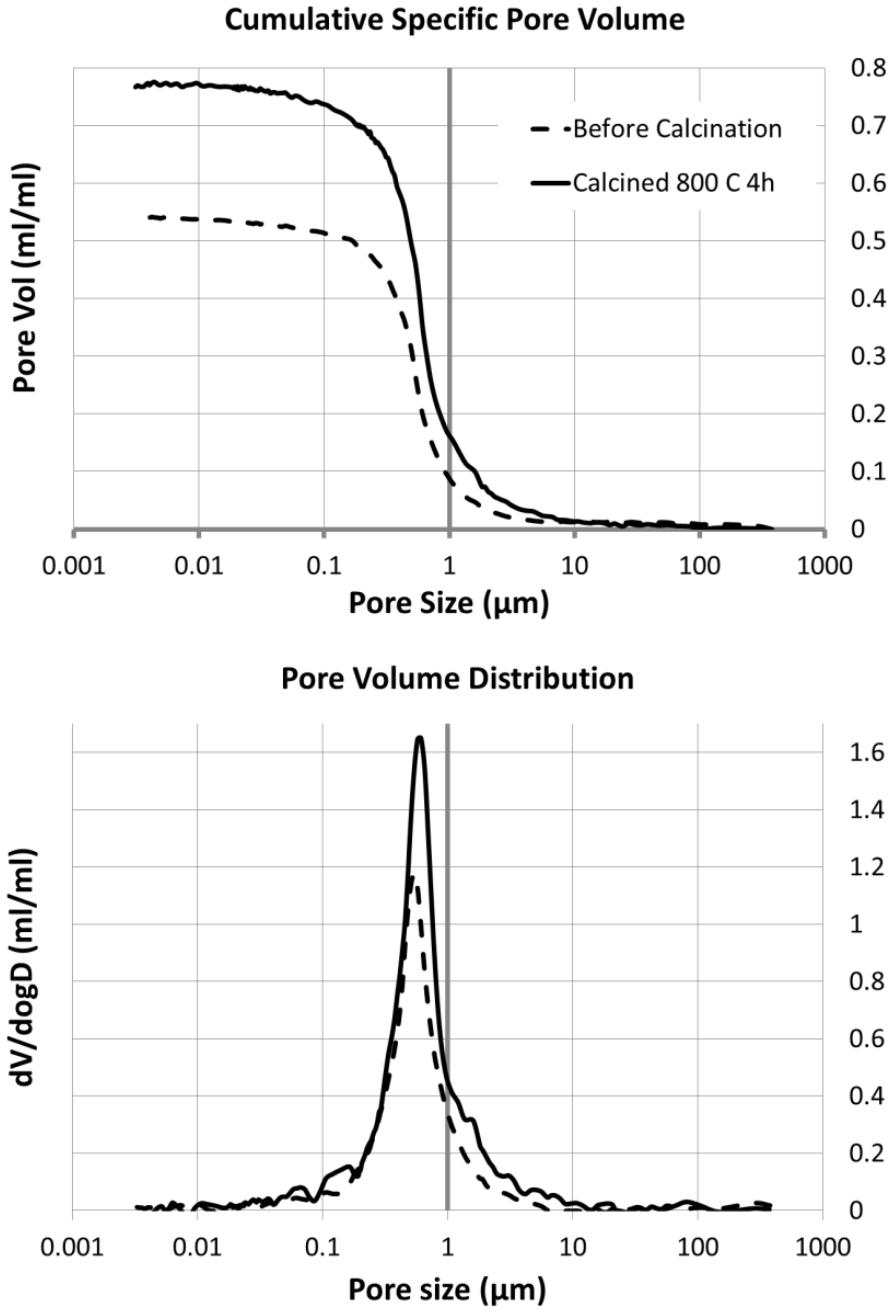

Figure 7.9. MIP results (first intrusion) of a Formulation E GP, composition 1•1•4•197, with 1 molar ratio 1 Na_2O•2.67 $Me_2Si(OEt)_2$, illustrating porosity before and after calcination (800 °C, 4 h in N_2, 5°/min ramps).

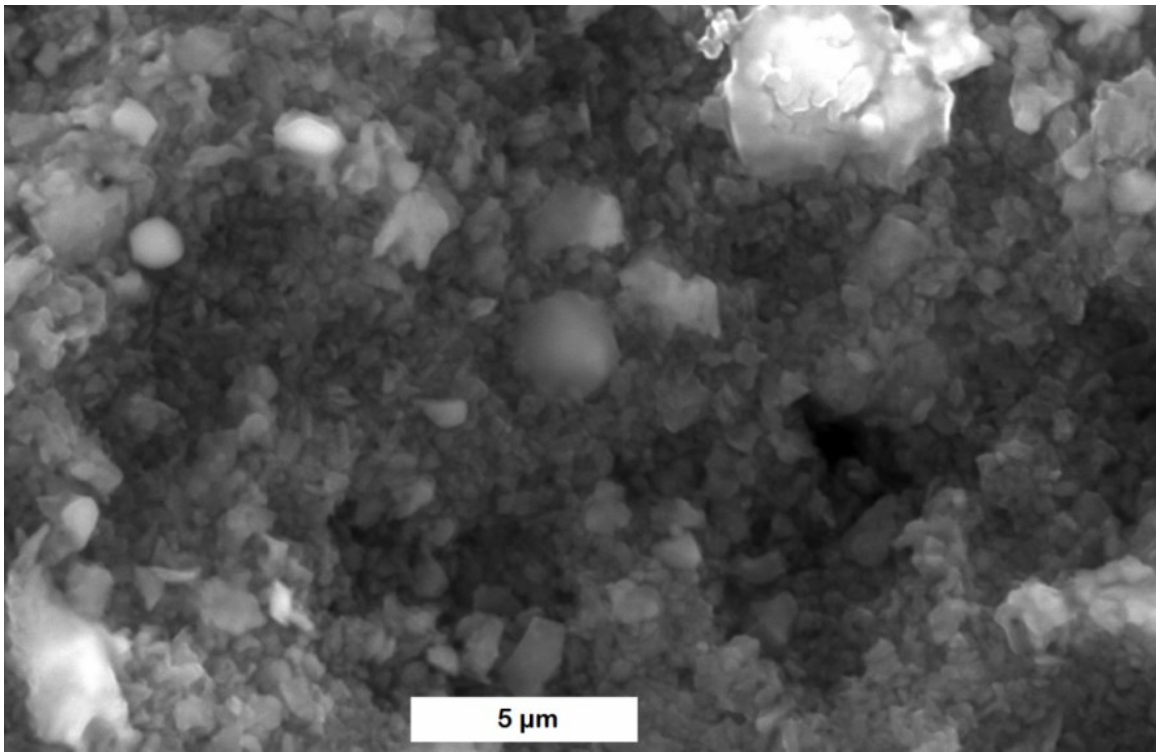

Figure 7.10. Scanning electron micrograph, showing the chaotic glass microstructure produced by calcination (800 °C, 4 h in N_2, 5°/min ramps) of a Formulation E GP, composition 1•1•4•197, with 1 Na_2O•2.67 $Me_2Si(OEt)_2$).

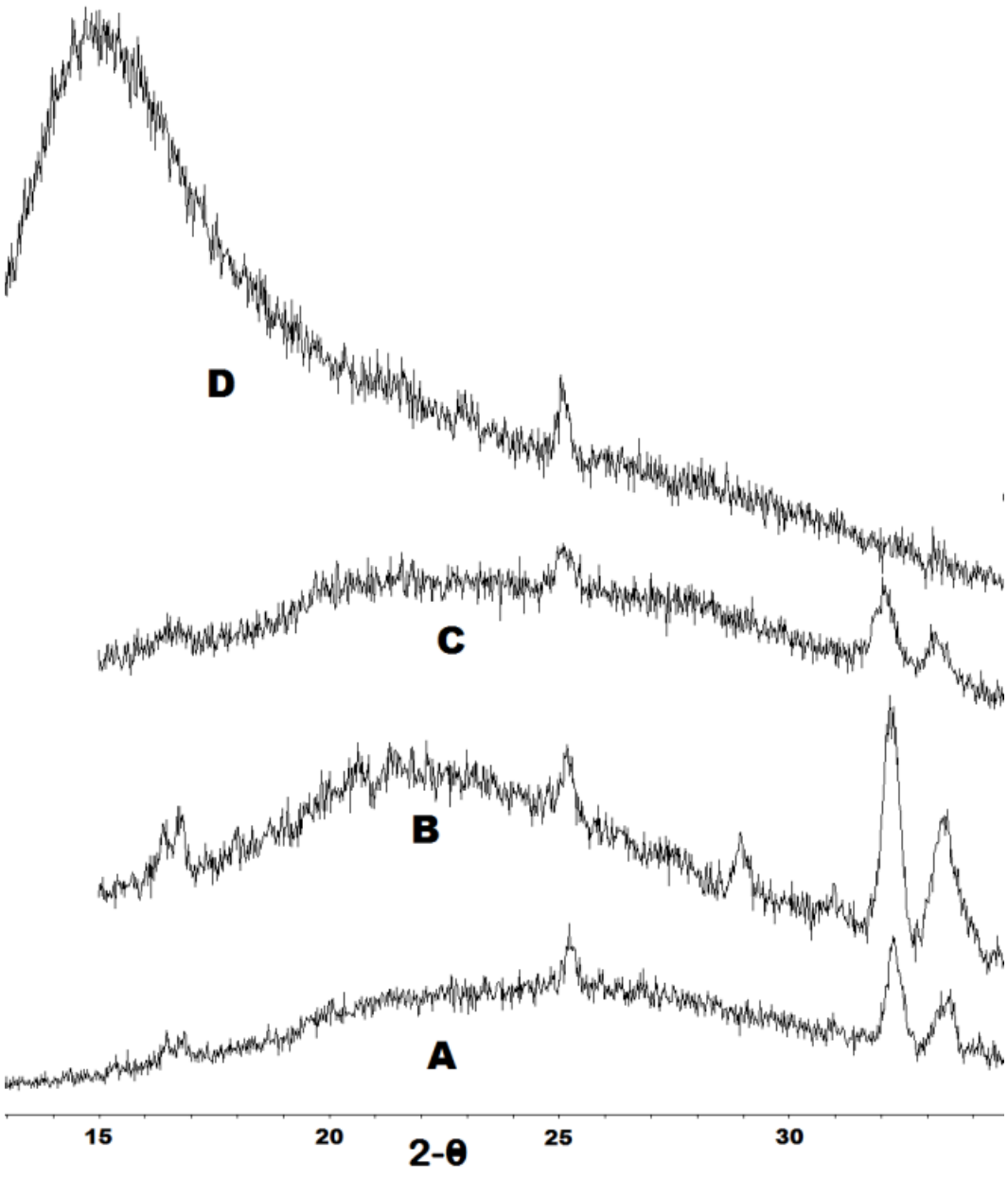

Figure 7.11. X-ray diffraction data of a Formulation C GP from Chapter 4 (A), a Formulation D GP with DIDE (B), and a Formulation E GP with DIDE before (C) and after (D) calcination (800 °C, 4 h in N_2, 5°/min ramps). After calcination, the pattern resembles an amorphous glass rather than a geopolymer.

CHAPTER 8

CONCLUSIONS

Both geopolymer understanding and control of geopolymer porosity have been improved. Initially, it was shown that functional alkoxysilanes could be incorporated directly into geopolymer slurry to meaningfully affect various geopolymer properties. The use of 0.072 mol phenylaminopropyltrimethoxysilane/mol geopolymer allowed for tensile adhesion strength (>0.09 MPa) to extruded polystyrene foams that surpassed the cohesive strength of the foam. Similarly, the addition of 0.10 mol methacryloxypropyltrimethoxysilane/mol geopolymer improved the Weibull modulus of compressive strength (>48%), and water retention (drying time extended from days to weeks). Alkoxysilane was found to reduce the degree of reactivity of geopolymers but not to totally prevent geopolymerization.

Geopolymer densification (up to a 24% increase in bulk density) and mesoporosity reduction (up to a tenfold decrease in mesoporosity volume) was achieved through the addition of the hydrogel-forming alkoxysilanes methacryloxypropyltrimethoxysilane. The gradual formation of sodium acrylate species within the geopolymer during curing allowed for meaningful property modification with amounts greater than at least 0.06 mol additive/mol geopolymer. Organic tube structures with a length of a few μm and a diameter of hundreds of nm were formed above this concentration, suggesting a saturation amount of alkoxysilane monomer incorporated into the geopolymer matrix. The addition of this hydrogel-forming additive caused the geopolymer to dry significantly slower in ambient conditions than a regular geopolymer.

Additionally, gas adsorption porosimetry techniques used in the mesoporosity analysis were intensively investigated and it was found that structural changes to a regular geopolymer

during sample evacuation were significant, but could be mitigated by evacuation at a temperature of less than 100 °C. With such treatment, expected trends in adsorption as a function of composition and curing temperature were observed.

Geopolymer macroporosity was investigated using mercury intrusion porosimetry, and a novel method of data analysis was developed to aid in the investigation. This method allowed for use of some depressurization data without independent measurement of the receding contact angle. Tests on an alumina filter showed that the pore size distribution obtained did not resemble the pore size distribution obtained using electron microscopy cross sections, but the discrepancies observed resembled those found using traditional data analysis.

Geopolymer macroporosity was controlled through an oil-in-water emulsion template method utilizing a dilute evaporative slurry as the water phase. The extent of geopolymerization was found to be limited, and this reduced geopolymerization was investigated using dilute slurries without emulsion additives. It was found that a significant cause of decreased reactivity was the formation of sodium carbonates, which deprived the geopolymer of necessary charge-balancing cations. Reactivity was increased by premixing a concentrated, sealed geopolymer slurry under constant agitation, and then diluting it to produce the dilute evaporative slurry. This technique mitigated reactivity issues for both regular evaporated geopolymers and the emulsion-template geopolymers.

Nonfunctional dialkoxysilanes such as dimethyldethoxysilane were instrumental in the synthesis of >70% porous, <1 μm critical percolation diameter, near-net-shape geopolymer monoliths. These compounds functioned both as a surfactant in the slurry and created a hydrophobic coating on pore interiors after gelation, decreasing drying stresses. Manipulation of total water content and emulsion stability allowed for independent control of porosity volume

and pore size. These monoliths could be calcined in inert atmosphere to 800 °C for conversion to a glass ceramic. The glass ceramic had increased porosity compared to the unfired monolith, and a slightly larger critical percolation diameter. Synchrotron radiation identified the conversion of a portion of the organic pore coating to ß-SiC.

CHAPTER 9

SUGGESTIONS FOR FUTURE WORK

This project began as a practical investigation into improved geopolymer porosity control at a practical cost for either insulation or bulk cement uses. It became evident that so little investigation had been conducted in this area that necessity required a change in focus to investigating the mechanisms involved in the synthesis of porous and nonporous geopolymers and examining the processing parameters involved in changing them.

The results of such investigations are described in detail in this document, particularly Chapters 6 and 7. However, the use of alkoxysilanes is not a practical method of achieving the original aims of the project, although they make for a terrific model system. Furthermore, the efficiencies observed through our methods are not high. For a commercial product, it is necessary both to improve efficiency and to identify additives which can be acquired cheaply and processed quickly.

9.1. System Optimization

Rather than investigate a variety of additives and processing routes blindly in the hope of producing a marketable product, this project concentrated on finding a workable solution to each of the two major project goals, and then varying systems and parameters to determine what aspects of microstructure and processing were important for porosity and other properties. As a consequence, some of the most promising aspects of design space have not been investigated.

For the nonporous geopolymer, investigating the three-phase system of geopolymer, hydrogel additive and filler phase is likely to result in a more efficient use of organic material, especially as potential synergic effects between filler and additive are conceivable. Additionally,

any commercial product is likely to utilize multiple different hydrogel additives, in the interest of eliminating the requisite 0.06 mol acrylate/mol GP that was observed for property benefit. It is likely that the substantial amount of design space between these two possibilities could produce an effective high-strength, high-Weibull-modulus geopolymer for practical use.

The advancements shown in developing the porous geopolymer are more incremental in a long history of porous silicate research. In this system, optimization depends on efficient control of the interfacial characteristics of the emulsion phase, along with the processing parameters to dry the material as rapidly as possible while still ensuring reactivity. In addition, preliminary work suggests that a valid, though imperfect, substitute for the DIDE additive is a much more limited amount of non-ionic surfactant. Otherwise, the porous geopolymer sits comfortably within the realm of xerogels and related structures, but the fired porous geopolymer potentially occupies a rather less populated space due to the easy synthesis of silicon carbide from the organic additive. Further investigation of practical applications for this material has some merit.

9.2. Characterization Modifications

This exploration identified serious concerns with the conventional ways of exploring geopolymer porosity, particularly with regards to accurately determining a pore size distribution. The focus of Chapter 5 was addressing these concerns, and some novel ideas have been explored. Augmenting this analysis can take numerous different directions. Increasing precision with techniques such as tomography to more closely examine geopolymer pore morphology would be valuable, especially as Chapter 7 describes a technique that brings extensive porosity into the 100s of nm range, which is substantially easier to image. Another possibility is to

consider the kinetics of pore formation in much greater detail through various in situ methods as well as computer modeling and theoretical work.

REFERENCES

[1]J. Davidovits, "Inorganic Polymeric New Materials," *J. Therm. Anal. Calorim.,* **37** 1633-56 (1991).

[2]J. G. S. van Jaarsveld, J. S. J. van Deventer, and G. C. Lukey, "The Effect of Composition and Temperature on the Properties of Fly Ash- and Kaolinite-Based Geopolymers," *Chem. Eng. J.,* **89**[1-3] 63-73 (2002).

[3]S. A. Bernal, J. L. Provis, V. Rose, and R. Mejía de Gutierrez, "Evolution of Binder Structure in Sodium Silicate-Activated Slag-Metakaolin Blends," *Cem. Concr. Compos.,* **33**[1] 46-54 (2011).

[4]S. Detphan and P. Chindaprasirt, "Preparation of Fly Ash and Rice Husk Ash Geopolymer," *Int. J. Min. Met. Mater.,* **16**[6] 720-26 (2009).

[5]P. Duxson, A. Fernandez-Jimenez, J. L. Provis, G. C. Lukey, A. Palomo, and J. S. J. van Deventer, "Geopolymer Technology: The Current State of the Art," *J. Mater. Sci.,* **42**[9] 2917-33 (2007).

[6]J. L. Provis, "Geopolymers: Structures, Processing, Properties and Industrial Applications.″ Taylor and Francis (CRC Press): London, (2009).

[7]J. Davidovits, "Geopolymer Chemistry and Applications.″ Institut Geopolymere: St. Quentin, France, (2008).

[8]J. L. Provis, G. C. Lukey, and J. S. J. van Deventer, "Do Geopolymers Actually Contain Nanocrystalline Zeolites? A Reexamination of Existing Results," *Chem. Mater.,* **17**[12] 3075-85 (2005).

[9]J. L. Bell and W. M. Kriven, "Preparation of Ceramic Foams from Metakaolin-Based Geopolymer Gels," pp. 96-111. in Developments in Strategic Materials: Ceramic Engineering and Science Proceedings, Volume 29, Issue 10**.** John Wiley & Sons, Inc., 2008.

[10]E. Prud'homme, P. Michaud, E. Joussein, C. Peyratout, A. Smith, and S. Rossignol, "In Situ Inorganic Foams Prepared from Various Clays at Low Temperature," *Appl. Clay Sci.,* **51**[1-2] 15-22 (2011).

[11]J. L. Bell and W. M. Kriven, "Nanoporosity in Aluminosilicate, Geopolymeric Cements," *Microsc. Microanal.,* **10**[S02] (2004).

[12]J. Henon, A. Alzina, J. Absi, D. S. Smith, and S. Rossignol, "Porosity Control of Cold Consolidated Geomaterial Foam: Temperature Effect," *Ceram. Int.,* **38**[1] 77-84 (2012).

[13]K. Okada, A. Ooyama, T. Isobe, Y. Kameshima, A. Nakajima, and K. J. D. MacKenzie, "Water Retention Properties of Porous Geopolymers for Use in Cooling Applications," *J. Eur. Ceram. Soc.,* **29**[10] 1917-23 (2009).

[14]T. L. Metroke, M. V. Henley, and M. I. Hammons, "Effect of Curing Conditions on the Porosity Characteristics of Metakaolin–Fly Ash Geopolymers," pp. 11-15. in Strategic Materials and Computational Design: Ceramic Engineering and Science Proceedings, Volume 31, Issue 10**.** John Wiley & Sons, Inc., 2010.

[15]J. Bell, "Structural Evolution and Ceramic Formation in Metakaolin-Based Geopolymers," Ph. D. Thesis, University of Illinois at Urbana-Champaign (2008).

[16]P. Duxson, J. L. Provis, G. C. Lukey, S. W. Mallicoat, W. M. Kriven, and J. S. J. van Deventer, "Understanding the Relationship between Geopolymer Composition, Microstructure and Mechanical Properties," *Colloid. Surface. A,* **269**[1-3] 47-58 (2005).

[17]W. M. Kriven and J. Bell, "Effect of Alkali Choice of Geopolymer Properties," pp. 99-104. in The 28th International Conference on Advanced Ceramics and Composites B: Ceramic Engineering and Science Proceedings, Volume 25, Issue 4, **Vol. 25.** *Ceramic Engineering and Science Proceedings.* Edited by E. Lara-Curzio and J. M. Readey. The American Ceramic Society, 2004.

[18]Sindhunata, J. S. J. van Deventer, G. C. Lukey, and H. Xu, "Effect of Curing Temperature and Silicate Concentration on Fly-Ash-Based Geopolymerization," *Ind. Eng. Chem. Res.,* **45**[10] 3559-68 (2006).

[19]D. C. Comrie and W. M. Kriven, "Composite Cold Ceramic Geopolymer in a Refractory Application," *Ceram. Trans.,* **153** 211-25 (2003).

[20]T. Lin, D. Jia, P. He, M. Wang, and D. Liang, "Effects of Fiber Length on Mechanical Properties and Fracture Behavior of Short Carbon Fiber Reinforced Geopolymer Matrix Composites," *Mater. Sci. Eng., A,* **497**[1-2] 181-85 (2008).

[21]Z. J. Li, Y. S. Zhang, and X. M. Zhou, "Short Fiber Reinforced Geopolymer Composites Manufactured by Extrusion," *J. Mater. Civ. Eng.,* **17**[6] 624-31 (2005).

[22]Q. Zhao, B. Nair, T. Rahimian, and P. Balaguru, "Novel Geopolymer Based Composites with Enhanced Ductility," *J. Mater. Sci.,* **42**[9] 3131-37 (2007).

[23]H. Wang, H. Li, and F. Yan, "Synthesis and Tribological Behavior of Metakaolinite-Based Geopolymer Composites," *Mater. Lett.,* **59**[29-30] 3976-81 (2005).

[24]W. K. W. Lee and J. S. J. van Deventer, "The Interface between Natural Siliceous Aggregates and Geopolymers," *Cem. Concr. Res.,* **34**[2] 195-206 (2004).

[25]E. Prud'homme, P. Michaud, E. Joussein, J. M. Clacens, and S. Rossignol, "Role of Alkaline Cations and Water Content on Geomaterial Foams: Monitoring During Formation," *J. Non-Cryst. Solids,* **357**[4] 1270-78 (2011).

[26]P. Duxson, G. C. Lukey, and J. S. J. van Deventer, "Thermal Conductivity of Metakaolin Geopolymers Used as a First Approximation for Determining Gel Interconnectivity," *Ind. Eng. Chem. Res.,* **45**[23] 7781-88 (2006).

[27]K. Sagoe-Crenstil, L. Weng, and A. H. Taylor, "Hybrid Inorganic Polymer Systems," Patent US 7771686 (2010).

[28]C. Han, A. J. Pyzik, and J. Liu, "Modified Geopolymer Compositions, Processes and Uses," Patent US 2010/0304165 (2010).

[29]Y. J. Zhang, S. Li, D. L. Xu, B. Q. Wang, G. M. Xu, D. F. Yang, N. Wang, H. C. Liu, and Y. C. Wang, "A Novel Method for Preparation of Organic Resins Reinforced Geopolymer Composites," *J. Mater. Sci.,* **45**[5] 1189-92 (2010).

[30]H. Wang, H. Li, and F. Yan, "Reduction in Wear of Metakaolinite-Based Geopolymer Composite through Filling of PTFE," *Wear,* **258**[10] 1562-66 (2005).

[31]M. Choi, H. S. Cho, R. Srivastava, C. Venkatesan, D. H. Choi, and R. Ryoo, "Amphiphilic Organosilane-Directed Synthesis of Crystalline Zeolite with Tunable Mesoporosity," *Nat. Mater.,* **5**[9] 718-23 (2006).

[32]F. Schwertfeger, D. Frank, and M. Schmidt, "Hydrophobic Waterglass Based Aerogels without Solvent Exchange or Supercritical Drying," *J. Non-Cryst. Solids,* **225**[0] 24-29 (1998).

[33]H. Xu and J. S. J. Van Deventer, "Microstructural Characterisation of Geopolymers Synthesised from Kaolinite/Stilbite Mixtures Using XRD, MAS-NMR, SEM/EDX, TEM/EDX, and HREM," *Cem. Concr. Res.,* **32**[11] 1705-16 (2002).

[34]E. Alvarez-Ayuso, X. Querol, F. Plana, A. Alastuey, N. Moreno, M. Izquierdo, O. Font, T. Moreno, S. Diez, E. Vazquez, and M. Barra, "Environmental, Physical and Structural Characterisation of Geopolymer Matrixes Synthesised from Coal (Co-)Combustion Fly Ashes," *J Hazard Mater,* **154**[1-3] 175-83 (2008).
[35]A. Fernández-Jiménez, A. Palomo, I. Sobrados, and J. Sanz, "The Role Played by the Reactive Alumina Content in the Alkaline Activation of Fly Ashes," *Microporous Mesoporous Mater.,* **91**[1-3] 111-19 (2006).
[36]Z. Zhang, X. Yao, and H. Zhu, "Effects of Modulus of Sodium Silicate Solution on Mechanical Properties and Microstructure of Geopolymer," *Journal of the Nanjing University of Technology,* **33** 52-56 (2011).
[37]H. Wang, H. Li, and F. Yan, "Synthesis and Mechanical Properties of Metakaolinite-Based Geopolymer," *Colloid. Surface. A,* **268**[1–3] 1-6 (2005).
[38]M. Sofi, J. S. J. van Deventer, P. A. Mendis, and G. C. Lukey, "Engineering Properties of Inorganic Polymer Concretes (Ipcs)," *Cem. Concr. Res.,* **37**[2] 251-57 (2007).
[39]K. J. D. MacKenzie, N. Rahner, M. E. Smith, and A. Wong, "Calcium-Containing Inorganic Polymers as Potential Bioactive Materials," *J. Mater. Sci.,* **45**[4] 999-1007 (2009).
[40]D. R. Lowry and W. M. Kriven, "Effect of High Tensile Strength Polypropylene Chopped Fiber Reinforcements on the Mechanical Properties of Sodium Based Geopolymer Composites," pp. 47-56. in Strategic Materials and Computational Design: Ceramic Engineering and Science Proceedings, Volume 31, Issue 10**.** John Wiley & Sons, Inc., 2010.
[41]W. M. Kriven, J. L. Bell, and M. Gordon, "Microstructure and Microchemistry of Fully-Reacted Geopolymers and Geopolymer Matrix Composites," *Ceram. Trans.,* **153** 227-50 (2004).
[42]J. Bell, M. Gordon, and W. Kriven, "Use of Geopolymeric Cements as a Refractory Adhesive for Metal and Ceramic Joins," pp. 407-13. in Advances in Ceramic Coatings and Ceramic-Metal Systems: Ceramic Engineering and Science Proceedings**.** Edited by D. Zhu and K. Plucknett. John Wiley & Sons, Inc., Hoboken, NJ, 2005.
[43]J. G. S. Van Jaarsveld, J. S. J. Van Deventer, and L. Lorenzen, "The Potential Use of Geopolymeric Materials to Immobilise Toxic Metals: Part I. Theory and Applications," *Miner. Eng.,* **10**[7] 659-69 (1997).
[44]J. G. S. Van Jaarsveld, J. S. J. Van Deventer, and A. Schwartzman, "The Potential Use of Geopolymeric Materials to Immobilise Toxic Metals: Part II. Material and Leaching Characteristics," *Miner. Eng.,* **12**[1] 75-91 (1999).
[45]B. E. Laney, F. T. Williams, R. L. Rutherford, and D. T. Bailey, "Advanced Geopolymer Composites," US Patent 5244726 (1993).
[46]F. Frizon and C. J. Dubien, "Method of Preparing a Controlled Porosity Geopolymer, the Resulting Geopolymer and the Various Applications Thereof," US Patent Application 2010-0222204 (2010).
[47]J. Davidovits, "Structural Characterization of Geopolymeric Materials with X-Ray Diffractometry and MAS-NMR Spectroscopy,″ pp. 149-66 in Geopolymers '88. Edited by J. Davidovits and J. Orlinsky. St. Quentin, France.
[48]K. J. D. MacKenzie and M. E. Smith, "Multinuclear Solid-State NMR of Inorganic Materials.″ Pergamon, (2002).

[49]E. Lippmaa, M. Maegi, A. Samoson, G. Engelhardt, and A. R. Grimmer, "Structural Studies of Silicates by Solid-State High-Resolution Silicon-29 NMR," *J. Am. Chem. Soc.,* **102**[15] 4889-93 (1980).
[50]C. Xiaotang, X. Jun, Z. Juanrong, C. Yiliang, G. Shiling, and Q. Jianzhao, "Study on the Synthesis of Zeolite 4a and Geopolymer and Ion-Exchange," *New Chemical Materials,* **8** 729-46 (2007).
[51]D. Khale and R. Chaudhary, "Mechanism of Geopolymerization and Factors Influencing Its Development: A Review," *J. Mater. Sci.,* **42**[3] 729-46 (2007).
[52]W. Loewenstein, "The Distribution of Aluminum in the Tetrahedra of Silicates and Aluminates," *Am. Mineral.,* **39** 92-96 (1954).
[53]J. L. Bell, P. Sarin, J. L. Provis, R. P. Haggerty, P. E. Driemeyer, P. J. Chupas, J. S. J. van Deventer, and W. M. Kriven, "Atomic Structure of a Cesium Aluminosilicate Geopolymer: A Pair Distribution Function Study," *Chem. Mater.,* **20**[14] 4768-76 (2008).
[54]J. L. Bell, P. Sarin, P. E. Driemeyer, R. P. Haggerty, P. J. Chupas, and W. M. Kriven, "X-Ray Pair Distribution Function Analysis of a Metakaolin-Based, $KAlSi_2O_6 \cdot 5.5H_2O$ Inorganic Polymer (Geopolymer)," *J. Mater. Chem.,* **18**[48] 5974-81 (2008).
[55]W. M. Kriven, J. L. Bell, and M. Gordon, "Microstructure and Nanoporosity of as-Set Geopolymers," pp. 491-503. in Mechanical Properties and Performance of Engineering Ceramics II: Ceramic Engineering and Science Proceedings, Volume 27, Issue 2**.** Edited by R. Tandon, A. Wereszczak, andE. Lara-Curzio. John Wiley & Sons, Inc., 2006.
[56]W. M. Kriven, J. Bell, S. W. Mallicoat, and M. Gordon, "Intrinsic Microstructure and Properties of Metakaolin-Based Geopolymers," pp. 71-86. in Proceedings of the International Workshop on Geopolymer Binders - Interdependence of Composition, Structure and Properties**.** Bauhaus-Universität, Weimar, Germany, 2007.
[57]A. Hajimohammadi, J. L. Provis, and J. S. J. van Deventer, "Effect of Alumina Release Rate on the Mechanism of Geopolymer Gel Formation," *Chem. Mater.,* **22**[18] 5199-208 (2010).
[58]D. R. M. Brew and K. J. D. MacKenzie, "Geopolymer Synthesis Using Silica Fume and Sodium Aluminate," *J. Mater. Sci.,* **42**[11] 3990-93 (2007).
[59]J. L. Bell, P. E. Driemeyer, and W. M. Kriven, "Formation of Ceramics from Metakaolin-Based Geopolymers: Part I-Cs-Based Geopolymer," *J. Am. Ceram. Soc.,* **92**[1] 1-8 (2009).
[60]J. Rocha and J. Klinowski, "Solid-State NMR Studies of the Structure and Reactivity of Metakaolinite," *Angew. Chem. Int. Ed.,* **29**[5] 553-54 (1990).
[61]H. J. Zhu, X. Yao, and Z. H. Zhang, "Optimum Activated Temperature of Kaolin," *J. Cent. South Univ. T.,* **14** 131-34 (2007).
[62]A. Elimbi, H. K. Tchakoute, and D. Njopwouo, "Effects of Calcination Temperature of Kaolinite Clays on the Properties of Geopolymer Cements," *Constr. Build. Mater.,* **25**[6] 2805-12 (2011).
[63]J. L. Bell, W. M. Kriven, A. P. R. Johnson, and F. Caruso, "Laser Scanning Confocal Microscopic Analysis of Metakaolin-Based Geopolymers," pp. 273-82. in Developments in Porous, Biological and Geopolymer Ceramics: Ceramic Engineering and Science Proceedings, Volume 28, Issue 9**.** John Wiley & Sons, Inc., 2007.
[64]J. G. S. van Jaarsveld and J. S. J. van Deventer, "Effect of the Alkali Metal Activator on the Properties of Fly Ash-Based Geopolymers," *Ind. Eng. Chem. Res.,* **38**[10] 3932-41 (1999).

[65]C. Kuenzel, L. J. Vandeperre, S. Donatello, A. R. Boccaccini, and C. Cheeseman, "Ambient Temperature Drying Shrinkage and Cracking in Metakaolin-Based Geopolymers," *J. Am. Ceram. Soc.,* **95**[10] 3270-77 (2012).
[66]S. O'Connor and K. MacKenzie, "Synthesis, Characterisation and Thermal Behaviour of Lithium Aluminosilicate Inorganic Polymers," *J. Mater. Sci.,* **45**[14] 3707-13 (2010).
[67]J. L. Provis and J. S. J. van Deventer, "Geopolymerisation Kinetics. 2. Reaction Kinetic Modelling," *Chem. Eng. Sci.,* **62**[9] 2318-29 (2007).
[68]P. Rovnanik, "Effect of Curing Temperature on the Development of Hard Structure of Metakaolin-Based Geopolymer," *Constr. Build. Mater.,* **24**[7] 1176-83 (2010).
[69]J. W. Phair, J. D. Smith, and J. S. J. Van Deventer, "Characteristics of Aluminosilicate Hydrogels Related to Commercial "Geopolymers"," *Mater. Lett.,* **57**[28] 4356-67 (2003).
[70]D. S. Perera, O. Uchida, E. R. Vance, and K. S. Finnie, "Influence of Curing Schedule on the Integrity of Geopolymers," *J. Mater. Sci.,* **42**[9] 3099-106 (2007).
[71]M. F. Nuruddin, S. Demie, and N. Shafiq, "Effect of Mix Composition on Workability and Compressive Strength of Self-Compacting Geopolymer Concrete," *Can. J. Civil Eng.,* **38**[11] 1196-203 (2011).
[72]Q. Wang, X. Tu, Z. Y. Ding, and Z. T. Sui, "Effect of Curing System on Mechanical Property of Slag-Based Geopolymer," *Adv. Mat. Res.,* **250** 3372-76 (2011).
[73]J. L. Bell, P. E. Driemeyer, and W. M. Kriven, "Formation of Ceramics from Metakaolin-Based Geopolymers. Part II: K-Based Geopolymer," *J. Am. Ceram. Soc.,* **92**[3] 607-15 (2009).
[74]P. Duxson, G. C. Lukey, and J. S. J. van Deventer, "Thermal Evolution of Metakaolin Geopolymers: Part 1 - Physical Evolution," *J. Non-Cryst. Solids,* **352**[52-54] 5541-55 (2006).
[75]E. Prud'homme, P. Michaud, E. Joussein, C. Peyratout, A. Smith, S. Arrii-Clacens, J. M. Clacens, and S. Rossignol, "Silica Fume as Porogent Agent in Geo-Materials at Low Temperature," *J. Eur. Ceram. Soc.,* **30**[7] 1641-48 (2010).
[76]A. Tucker and C. Ward, "Critical State of Bubbles in Liquid-Gas Solutions," *J. Appl. Phys.,* **46**[11] 4801-08 (1975).
[77]C. E. Brennen, "Cavitation and Bubble Dynamics," **Vol. 44**. Oxford University Press, USA, (1995).
[78]P. Duxson, A. Fernández-Jiménez, J. L. Provis, G. C. Lukey, A. Palomo, and J. S. J. Deventer, "Geopolymer Technology: The Current State of the Art," *J. Mater. Sci.,* **42**[9] 2917-33 (2006).
[79]E. P. Plueddemann, "Silane Coupling Agents." Plenum Press: New York, (1991).
[80]J. F. Hyde and J. R. Wehrly, "Polymerization of Organopolysiloxanes," US Patent 2891920 (1959).
[81]W. K. W. Lee and J. S. J. van Deventer, "The Effects of Inorganic Salt Contamination on the Strength and Durability of Geopolymers," *Colloid. Surface. A,* **211**[2-3] 115-26 (2002).
[82]C. Friedel and A. Ladenburg, "Ueber Das Siliciumchloroform Und Dessen Derivate," *Justus Liebigs, Annalen der Chemie und Pharmacie,* **143** 118-28 (1867).
[83]Y. S. Zhang, W. Sun, Q. L. Chen, and L. Chen, "Synthesis and Heavy Metal Immobilization Behaviors of Slag Based Geopolymer," *J. Hazard. Mater.,* **143**[1-2] 206-13 (2007).

[84]O. K. Johannson, F. O. Stark, G. E. Vogel, and R. M. Fleischmann, "Evidence for Chemical Bond Formation at Silane Coupling Agent Interfaces," *J. Compos. Mater.,* **1**[3] 278-92 (1967).
[85]H. Ishida and J. L. Koenig, "Fourier Transform Infrared Spectroscopic Study of the Silane Coupling Agent/Porous Silica Interface," *J. Colloid Interface Sci.,* **64**[3] 555-64 (1978).
[86]S. R. Culler, H. Ishida, and J. L. Koenig, "Structure of Silane Coupling Agents Adsorbed on Silicon Powder," *J. Colloid Interface Sci.,* **106**[2] 334-46 (1985).
[87]P. Fierens, G. Vandendunghen, W. Segers, and R. van Elsuwe, "Silane-Silanol Condensation Catalyzed by Organotin Compounds," *React. Kinet. Catal. Lett.,* **8**[2] 179-87 (1978).
[88]I. J. Boyer, "Toxicity of Dibutyltin, Tributyltin and Other Organotin Compounds to Humans and to Experimental Animals," *Toxicology,* **55**[3] 253-98 (1989).
[89]E. J. A. Pope and J. D. Mackenzie, "Sol-Gel Processing of Silica: II. The Role of the Catalyst," *J. Non-Cryst. Solids,* **87**[1–2] 185-98 (1986).
[90]J. M. J. Vankan, J. J. Ponjeé, J. W. De Haan, and L. J. M. Van de Ven, "On the Nature of Chemical Binding of Organic Silanes to Water-Free Silica Surfaces: A High-Resolution Solid-State NMR Spectroscopic Study," *J. Colloid Interface Sci.,* **126**[2] 604-09 (1988).
[91]J. P. Blitz, R. S. S. Murthy, and D. E. Leyden, "Studies of Silylation of Cab-O-Sil with Methoxymethylsilanes by Diffuse Reflectance FTIR Spectroscopy," *J. Colloid Interface Sci.,* **121**[1] 63-69 (1988).
[92]B. E. Glad, A. Boies, and S. Girshick, "Photo-CVD Coating of Nanoparticles with Silicon Dioxide,″ pp. 124-25 in NNIN REU Research Accomplishments. **Vol. 2007**Edited by M. Mallison.
[93]A. M. Cabral, R. G. Duarte, M. F. Montemor, and M. G. S. Ferreira, "A Comparative Study on the Corrosion Resistance of AA2024-T3 Substrates Pre-Treated with Different Silane Solutions," *Prog. Org. Coat.,* **54**[4] 322-31 (2005).
[94]M. T. Scholz and G. V. Tiers, "Coating Composition Having Anti-Reflective, and Anti-Fogging Properties," US Patent 5585186 (1996).
[95]M. W. Daniels, J. Sefcik, L. F. Francis, and A. V. McCormick, "Reactions of a Trifunctional Silane Coupling Agent in the Presence of Colloidal Silica Sols in Polar Media," *J. Colloid Interface Sci.,* **219**[2] 351-56 (1999).
[96]J. Shah, S. S. Kim, and T. J. Pinnavaia, "A Versatile Pathway for the Direct Assembly of Organo-Functional Mesostructures from Sodium Silicate," *Chemical Communications (Cambridge)*[5] 572-3 (2004).
[97]F. Schwertfeger, W. Glaubitt, and U. Schubert, "Hydrophobic Aerogels from $Si(OMe)_4$/$MeSi(OMe)_3$ Mixtures," *J. Non-Cryst. Solids,* **145**[0] 85-89 (1992).
[98]R. Jansen, A. Zimmermann, E. Jacquinot, and D. Smith, "Xerogels and Process for Their Preparation," US Patent 5795556 (1998).
[99]Z. Zhang, "Hydrophobic, Fluorinated Silica Xerogel for Low-K Applications," Ph.D. Thesis, University of North Texas (2004).
[100]C. Tanford, "Thermodynamics of Micelle Formation: Prediction of Micelle Size and Size Distribution," *Proceedings of the National Academy of Sciences,* **71**[5] 1811-15 (1974).
[101]C. Stubenrauch, "Microemulsions: Background, New Concepts, Applications, Perspectives.″ Blackwell Publishing: West Sussex, UK., (2009).

[102]J. Lipfert, L. Columbus, V. B. Chu, S. A. Lesley, and S. Doniach, "Size and Shape of Detergent Micelles Determined by Small-Angle X-Ray Scattering," *J. Phys. Chem. B,* **111**[43] 12427-38 (2007).
[103]S. Melle, M. Lask, and G. G. Fuller, "Pickering Emulsions with Controllable Stability," *Langmuir,* **21**[6] 2158-62 (2005).
[104]Y. De Smet, J. Malfait, C. De Vos, L. Deriemaeker, and R. Finsy, "Ostwald Ripening of Concentrated Alkane Emulsions: A Comparison of Fiber-Optics Dynamic Light Scattering and Conventional Dynamic Light Scattering," pp. 252-55. in Trends in Colloid and Interface Science Xi*,* **Vol. 105.** *Progress in Colloid and Polymer Science.* Edited by J. Rosenholm, B. Lindman, andP. Stenius. Springer Berlin / Heidelberg, 1997.
[105]A. J. Queimada, I. M. Marrucho, and J. A. P. Coutinho, "Surface Tension of Pure Heavy N-Alkanes: A Corresponding States Approach," *Fluid Phase Equilib.,* **183–184**[0] 229-38 (2001).
[106]M. Kahlweit and R. Strey, "Phase Behavior of Ternary Systems of the Type H_2O•Oil•Nonionic Amphiphile (Microemulsions)," *Angew. Chem. Int. Ed.,* **24**[8] 654-68 (1985).
[107]W. C. Griffin, "Classification of Surface-Active Agents by 'HLB'," *Journal of the Society of Cosmetic Chemists,* **1** 311-26 (1949).
[108]J. T. Davies, "A Quantitative Kinetic Theory of Emulsion Type I: Physical Chemistry of the Emulsifying Agent,″ pp. 426-38 in Second International Congress of Surface Activity.
[109]I. J. Lin and L. Marzall, "Partition Coefficent, HLB and Effective Chain Length of Surface Active Agents," *Prog. Colloid Polym. Sci.,* **63** 99-104 (1978).
[110]O. B. Ho, "Electrokinetic Studies on Emulsions Stabilized by Ionic Surfactants: The Electroacoustophoretic Behavior and Estimation of Davies' HLB Increments," *J. Colloid Interface Sci.,* **198**[2] 249-60 (1998).
[111]A. O'Lenick, "Silicone Emulsions and Surfactants," *Journal of Surfactants and Detergents,* **3**[3] 387-93 (2000).
[112]M. Sahimi, "Applications of Percolation Theory.″ Taylor and Francis: London, (1994).
[113]D. P. Bentz and E. J. Garboczi, "Percolation of Phases in a Three-Dimensional Cement Paste Microstructural Model," *Cem. Concr. Res.,* **21**[2–3] 325-44 (1991).
[114]D. L. Kong, J. G. Sanjayan, and K. Sagoe-Crentsil, "Comparative Performance of Geopolymers Made with Metakaolin and Fly Ash after Exposure to Elevated Temperatures," *Cem. Concr. Res.,* **37**[12] 1583-89 (2007).
[115]N. M. Alford and A. A. Rahman, "An Assessment of Porosity and Pore Sizes in Hardened Cement Pastes," *J. Mater. Sci.,* **16** 3105-14 (1981).
[116]R. G. Larson and N. R. Morrow, "Effects of Sample Size on Capillary Pressures in Porous Media," *Powder Technol.,* **30**[2] 123-38 (1981).
[117]D. Bonen, "Gypsum-Cement System for Construction Materials," United States Patent 6241815 (2001).
[118]J. Aguado, D. P. Serrano, and J. M. Rodríguez, "Zeolite Beta with Hierarchical Porosity Prepared from Organofunctionalized Seeds," *Microporous Mesoporous Mater.,* **115**[3] 504-13 (2008).
[119]D. Jaumain and B.-L. Su, "Monitoring the Brönsted Acidity of Zeolites by Means of in Situ FT-IR and Catalytic Testing Using Chloromethane as Probe Molecule," *Catal. Today,* **73**[1–2] 187-96 (2002).

[120]R. A. Cairncross, L. F. Francis, and L. E. Scriven, "Competing Drying and Reaction Mechanisms in the Formation of Sol-to-Gel Films, Fibers, and Spheres," *Drying Technol.,* **10**[4] 893-923 (1992).
[121]V. F. F. Barbosa, K. J. D. MacKenzie, and C. Thaumaturgo, "Synthesis and Characterisation of Materials Based on Inorganic Polymers of Alumina and Silica: Sodium Polysialate Polymers," *Int. J. Inorg. Mater.,* **2**[4] 309-17 (2000).
[122]L. A. Blum, "Role of Surface Speciation in the Low-Temperature Dissolution of Minerals," *Nature,* **331**[6155] 431-33 (1988).
[123]A. A. Shaikh, A. D. Salman, S. McNamara, G. Littlewood, F. Ramsay, and M. J. Hounslow, "In Situ Observation of the Conversion of Sodium Carbonate to Sodium Carbonate Monohydrate in Aqueous Suspension," *Ind. Eng. Chem. Res.,* **44**[26] 9921-30 (2005).
[124]M. J. Blunt, "Flow in Porous Media — Pore-Network Models and Multiphase Flow," *Curr. Opin. Colloid Interface Sci.,* **6**[3] 197-207 (2001).
[125]M. Tuller, D. Or, and L. M. Dudley, "Adsorption and Capillary Condensation in Porous Media: Liquid Retention and Interfacial Configurations in Angular Pores," *Water Resour. Res.,* **35**[7] 1949-64 (1999).
[126]S. Brunauer, P. H. Emmett, and E. Teller, "Adsorption of Gases in Multimolecular Layers," *J. Am. Chem. Soc.,* **60**[2] 309-19 (1938).
[127]E. P. Barrett, L. G. Joyner, and P. P. Halenda, "The Determination of Pore Volume and Area Distributions in Porous Substances. I. Computations from Nitrogen Isotherms," *J. Am. Chem. Soc.,* **73**[1] 373-80 (1951).
[128]P. I. Ravikovitch, S. C. O. Domhnaill, A. V. Neimark, F. Schueth, and K. K. Unger, "Capillary Hysteresis in Nanopores: Theoretical and Experimental Studies of Nitrogen Adsorption on MCM-41," *Langmuir,* **11**[12] 4765-72 (1995).
[129]E. W. Washburn, "The Dynamics of Capillary Flow," *Phys. Rev.,* **17**[3] 273-83 (1921).
[130]F. Moro and H. Bohni, "Ink-Bottle Effect in Mercury Intrusion Porosimetry of Cement-Based Materials," *J. Colloid Interface Sci.,* **246**[1] 135-49 (2002).
[131]J. Zhou, G. Ye, and K. van Breugel, "Characterization of Pore Structure in Cement-Based Materials Using Pressurization–Depressurization Cycling Mercury Intrusion Porosimetry (PDC-MIP)," *Cem. Concr. Res.,* **40**[7] 1120-28 (2010).
[132]A. Reverberi, G. Ferraiolo, and A. Peloso, "Determination by Experiment of the Distribution Function of the Cylindrical Macropores and Ink Bottles in Porous Systems," *Anal. Chim.,* **56** 1552-61 (1966).
[133]C. A. León y León, "New Perspectives in Mercury Porosimetry," *Adv. Colloid Interface Sci.,* **76–77**[0] 341-72 (1998).
[134]A. Tsetsekou, G. Androutsopoulos, and R. Mann, "Mercury Porosimetry Hysteresis and Entrapment Predictions Based on a Corrugated Random Pore Model," *Chem. Eng. Commun.,* **110**[1] 1-29 (1991).
[135]R. F. Angulo, V. Alvarado, and H. Gonzalez, "Fractal Dimensions from Mercury Intrusion Capillary Tests,″ in Latin American Petroleum Engineering Conference II.
[136]P. A. Webb and C. Oor, "Analytical Methods in Fine Particle Technology.″ Micromeritics Instrument Corporation: Norcross, GA, (1997).
[137]A. Savitzky and M. J. E. Golay, "Smoothing and Differentiation of Data by Simplified Least Squares Procedures," *Anal. Chem.,* **36**[8] 1627-39 (1964).

[138]I. Langmuir, "The Constitution and Fundamental Properties of Solids and Liquids. II. Liquids.," *J. Am. Chem. Soc.,* **39**[9] 1848-906 (1917).
[139]M. Jaroniec, M. Kruk, J. P. Oliver, and S. Koch, "A New Method for the Accurate Pore Size Analysis of MCM-41 and Other Silica Based Mesoporous Materials," pp. 71-80. in Stud. Surf. Sci. Catal.*,* **Vol. 128.** Edited by K. K. Unger, G. Kreysa, andJ. P. Baselt. Elsevier, 2000.
[140]Micromeritics, "Micro Active,″ 1.01 ed. Micromeritics Instrument Corp.: Norcross, GA, (2012).
[141]D. A. Payne, K. S. W. Sing, and D. H. Turk, "Comparison of Argon and Nitrogen Adsorption Isotherms on Porous and Nonporous Hydroxylated Silica," *J. Colloid Interface Sci.,* **43**[2] 287-93 (1973).
[142]A. Kiselev, "Non-Specific and Specific Interactions of Molecules of Different Electronic Structures with Solid Surfaces," *Discuss. Faraday Soc.,* **40** 205-18 (1965).
[143]G. Y. Gor, M. Thommes, K. A. Cychosz, and A. V. Neimark, "Quenched Solid Density Functional Theory Method for Characterization of Mesoporous Carbons by Nitrogen Adsorption," *Carbon,* **50**[4] 1583-90 (2012).
[144]S. C. Carniglia, "Construction of the Tortuosity Factor from Porosimetry," *J. Catal.,* **102**[2] 401-18 (1986).
[145]S. Lowell, "Continuous Scan Mercury Porosimetry and the Pore Potential as a Factor in Porosimetry Hysteresis," *Powder Technol.,* **25**[1] 37-43 (1980).
[146]S. Lowell and J. Shields, "Influence of Contact Angle on Hysteresis in Mercury Porosimetry," *J. Colloid Interface Sci.,* **80**[1] 192-96 (1981).
[147]R. W. Smithwick and E. L. Fuller Jr, "A Generalized Analysis of Hysteresis in Mercury Porosimetry," *Powder Technol.,* **38**[2] 165-73 (1984).
[148]W. C. Conner Jr, A. M. Lane, and A. J. Hoffman, "Measurement of the Morphology of High Surface Area Solids: Hysteresis in Mercury Porosimetry," *J. Colloid Interface Sci.,* **100**[1] 185-93 (1984).
[149]H. Scher and R. Zallen, "Critical Density in Percolation Processes," *J. Chem. Phys.,* **53**[9] 3759-61 (1970).
[150]A. Cassie and S. Baxter, "Wettability of Porous Surfaces," *T. Faraday Soc.,* **40** 546-51 (1944).
[151]R. N. Wenzel, "Resistance of Solid Surfaces to Wetting by Water," *Ind. Eng. Chem,* **28**[8] 988-94 (1936).
[152]T. Young, "An Essay on the Cohesion of Fluids," *Philos. T. R. Soc.,* **95** 65-87 (1805).
[153]W. Choi, A. Tuteja, J. M. Mabry, R. E. Cohen, and G. H. McKinley, "A Modified Cassie-Baxter Relationship to Explain Contact Angle Hysteresis and Anisotropy on Non-Wetting Textured Surfaces," *J. Colloid Interface Sci.,* **339**[1] 208-16 (2009).
[154]T.-S. Wong and C.-M. Ho, "Dependence of Macroscopic Wetting on Nanoscopic Surface Textures," *Langmuir,* **25**[22] 12851-54 (2009).
[155]E. Bormashenko, "General Equation Describing Wetting of Rough Surfaces," *J. Colloid Interface Sci.,* **360**[1] 317-19 (2011).
[156]S. Lowell and J. E. Shields, "Hysteresis, Entrapment, and Wetting Angle in Mercury Porosimetry," *J. Colloid Interface Sci.,* **83**[1] 273-78 (1981).
[157]T. Kinton. in**.** Refractron Technologies Corp., 2012.
[158]J. Rouquerol, G. Baron, R. Denoyel, H. Giesche, J. Groen, P. Klobes, P. Levitz, A. V. Neimark, S. Rigby, and R. Skudas, "Liquid Intrusion and Alternative Methods for the

Characterization of Macroporous Materials (IUPAC Technical Report)," *Pure Appl. Chem.,* **84**[1] 107 (2012).
[159]P. Klobes, K. Meyer, and R. G. Munro, "Porosity and Specific Surface Area Measurements for Solid Materials.″ US Department of Commerce, Technology Administration, National Institute of Standards and Technology, (2006).
[160]N. C. Wardlaw and R. Taylor, "Mercury Capillary Pressure Curves and the Intepretation of Pore Structure and Capillary Behaviour in Reservoir Rocks," *B. Can. Petrol. Geol.,* **24**[2] 225-62 (1976).
[161]J. Van Brakel, S. Modry, and M. Svata, "Mercury Porosimetry--State-of-the-Art," *Powder Technol.,* **29** 1-12 (1981).
[162]L. R. Parks, "Cross-Linked Sodium Polyacrylate Adsorbent," US Patent 4295987 (1981).
[163]S. S. Musil, G. Kutyla, and W. Kriven, "The Effect of Basalt Chopped Fiber Reinforcement on the Mechanical Properties of Potassium Based Geopolymer," pp. 31-42. in Developments in Strategic Materials and Computational Design III: Ceramic Engineering and Science Proceedings, Volume 33, Issue 10**.** Edited by W. M. Kriven, A. L. Gyekenyesi, G. Westin, andJ. Wang. American Ceramics Society, Daytona Beach, FL, 2012.
[164]J. L. Provis and J. S. J. Deventer, "Direct Measurement of the Kinetics of Geopolymerisation by in-Situ Energy Dispersive X-Ray Diffractometry," *J. Mater. Sci.,* **42**[9] 2974-81 (2006).
[165]R. Schweins, J. Hollmann, and K. Huber, "Dilute Solution Behaviour of Sodium Polyacrylate Chains in Aqueous NaCl Solutions," *Polymer,* **44**[23] 7131-41 (2003).
[166]K. R. Rogan, "The Variations of the Configurational and Solvency Properties of Low Molecular Weight Sodium Polyacrylate with Ionic Strength," *Colloid. Polym. Sci.,* **273**[4] 364-69 (1995).
[167]S. Sacanna and D. J. Pine, "Shape-Anisotropic Colloids: Building Blocks for Complex Assemblies," *Curr. Opin. Colloid Interface Sci.,* **16**[2] 96-105 (2011).
[168]B. E. Glad and W. M. Kriven, "Optimization of Gas Adsorption Porosimetry for Geopolymer Analysis," *J. Am. Ceram. Soc.*[submitted] (2013).
[169]E. S. Rufino and E. E. C. Monteiro, "Infrared Study on Methyl Methacrylate–Methacrylic Acid Copolymers and Their Sodium Salts," *Polymer,* **44**[23] 7189-98 (2003).
[170]M. Pantoja, B. Díaz-Benito, F. Velasco, J. Abenojar, and J. C. del Real, "Analysis of Hydrolysis Process of Γ-Methacryloxypropyltrimethoxysilane and Its Influence on the Formation of Silane Coatings on 6063 Aluminum Alloy," *Appl. Surf. Sci.,* **255**[12] 6386-90 (2009).
[171]B. E. Glad and W. M. Kriven, "Humidity Effects on the Completion of Geopolymerization in Dilute Evaporative Slurries," pp. 25-30. in Developments in Strategic Materials and Computational Design III: Ceramic Engineering and Science Proceedings, Volume 33, Issue 10**.** Edited by W. M. Kriven, A. L. Gyekenyesi, G. Westin, andJ. Wang. American Ceramics Society, Daytona Beach, Fl., 2012.
[172]C. F. Maitland, C. E. Buckley, B. H. O'Connor, P. D. Butler, and R. D. Hart, "Characterization of the Pore Structure of Metakaolin-Derived Geopolymers by Neutron Scattering and Electron Microscopy," *J. Appl. Crystallogr.,* **44** 697-707 (2011).
[173]T. F. Baumann, M. A. Worsley, T. Y.-J. Han, and J. H. Satcher Jr, "High Surface Area Carbon Aerogel Monoliths with Hierarchical Porosity," *J. Non-Cryst. Solids,* **354**[29] 3513-15 (2008).

[174]M. Scheffler and P. Colombo, "Cellular Ceramics: Structure, Manufacturing, Properties and Applications.″ John Wiley & Sons, (2006).
[175]S. S. Kistler, "Method of Producing Aerogels," US Patent 2093454 (1937).
[176]H. Yokogawa and M. Yokoyama, "Hydrophobic Silica Aerogels," *J. Non-Cryst. Solids,* **186**[0] 23-29 (1995).
[177]V. S. Ramachandran, "Concrete Admixtures Handbook: Properties, Science, and Technology.″ Noyes Publications, (1995).
[178]M. J. Prince and H. W. Blanch, "Bubble Coalescence and Break-up in Air-Sparged Bubble Columns," *AlChE J.,* **36**[10] 1485-99 (1990).
[179]B. S. Chan and Y. H. Tsang, "A Theory on Bubble-Size Dependence of the Critical Electrolyte Concentration for Inhibition of Coalescence," *J Colloid Interface Sci,* **286**[1] 410-13 (2005).
[180]P. Kumar and K. L. Mittal, "Handbook of Microemulsion Science and Technology.″ CRC, (1999).
[181]J. R. Elliott and R. H. Krieble, "Organosilicon-Silica Sols," US Patent 2441422 (1948).
[182]Y. S. Zhang, W. Sun, Z. J. Li, X. M. Zhou, Eddie, and C. K. Chau, "Impact Properties of Geopolymer Based Extrudates Incorporated with Fly Ash and PVA Short Fiber," *Constr. Build. Mater.,* **22**[3] 370-83 (2008).
[183]A. Nazari, S. Riahi, and A. Bagheri, "Designing Water Resistant Lightweight Geopolymers Produced from Waste Materials," *Mater. Des.,* **35** 296-302 (2011).
[184]R. Tadmor, "Line Energy and the Relation between Advancing, Receding, and Young Contact Angles," *Langmuir,* **20**[18] 7659-64 (2004).
[185]V. V. Pujar and J. D. Cawley, "Effect of Stacking Faults on the X-Ray Diffraction Profiles of B-SiC Powders," *J. Am. Ceram. Soc.,* **78**[3] 774-82 (1995).
[186]V. G. Pol, S. V. Pol, A. Gedanken, S. H. Lim, Z. Zhong, and J. Lin, "Thermal Decomposition of Commercial Silicone Oil to Produce High Yield High Surface Area SiC Nanorods," *J. Phys. Chem. B,* **110**[23] 11237-40 (2006).
[187]BASF, "Chemical and Physical Characteristics of Metamax HRM." in BASF Chemical Reference Sheets**.** 2012.

APPENDIX A

GEOPOLYMER SYNTHESIS AND FORMULATIONS

For clarity, the precise synthesis routes of the various geopolymers mentioned in this document are described in detail here.

A.1. Geopolymer Precursors Used

Sodium silicate solution

Sodium silicate solution (waterglass) was prepared as follows: 160.0 g sodium hydroxide (Sigma-Aldrich Co., LLC, St. Louis, MO) was added to 360.0 g DI water in a stainless steel container and stirred using a polytetrafluoroethane stir bar with a magnetic stir plate until fully dissolved. The container was then sealed with polyethylene terephthalate plastic film, and the temperature of the stir plate was set to approximately 45 ºC. A total of 240.0 g fumed silica (Cab-o-sil LM-150D, Cabot Corp., Boston, MA) was then added in small batches of approximately 10 g, each time allowing for complete or almost complete dissolution of the silica before adding the next batch, with the container remaining sealed when not adding silica. After all silica was added, the container was resealed and the contents were allowed to stir at the elevated temperature for 24 hours. After 24 hours, the solution of sodium silicate was poured into a polyethylene container, and allowed to equilibrate at ambient conditions for at least two weeks.

Metakaolin

Metakaolin (kaolinite clay calcined at between 500 ºC and 800 ºC, and preferably between 650 ºC and 725 ºC) is produced commercially in several grades. MetaMax HRM (3.6

μm median particle size[117], BASF Corp., Florham Park, NJ) and MetaMax EF (2.7 μm median particle size[117], Engelhard Corp.) were used as received. Neither ball-milling nor attrition-milling of MetaMax EF down to a minimum median diameter of 0.8 μm contributed meaningful qualitative differences in final product properties as compared to MetaMax EF.

Impurities in the metakaolin[187] slightly altered the nominal composition, as described in Table A.1. For clarity, for water-content related experiments the nominal value was adjusted to account for these impurities.

Table A.1. Nominal Composition vs. Actual Composition (x•1•y•z, for $xNa_2O•Al_2O_3•ySiO_2•zH_2O$)

Nominal Composition	Formulations	Actual Composition
1•1•4.0•11	A, A2	1.06•1•4.23•11.58
1•1•3.9•11	B	1.03•1•4.17•11.25
1•1•4.0•z, z≠11	C, C2, D	1.06•1•4.23•z
1•1•3.9•197	E	1.03•1•4.17•197

A.2. Organic Additives Used

A summary of all organic precursors used, their abbrivations (if any) and the chapters of their use is listed in Table A.2.

A.3. Synthesis and Mixing Equipment Used

Planetary centrifugal mixer: ARE-250 (Thinky Corp., Tokyo) with polyethylene sample container.

Ultrasonicator: W-385 Ultrasonicator (Heat Systems Ultrasonics).

Humidity chamber: 1000H Series (TestEquity LLC).

Table A.2. List of Organic Additives and Their Abbreviations		
Additive	Abbreviation	Chapters Used
Acrylic acid	AA	6
Aminopropyltrimethoxysilane	AMS	3
Ammonium polyacrylate (40% solution in water)	Darvan 821A	4, 7
Dimethyldiethoxysilane	DIDE	7
Dimethyldimethoxysilane	DIDM	7
Diphenyldimethoxysilane	DPhDM	7
Dodecane	$C_{12}H_{26}$	7
Hexane	C_6H_{14}	7
Methacrylic acid	MAA	6
Methacryloxymethyltrimethoxysilane	MEMO-Me	6
Methacryloxypropylmethyldimethoxysilane	MEMO-2,1	3,6
Methacryloxypropyltrimethoxysilane	MEMO	6
Methyltriethoxysilane	MTES	7
Phenylaminopropyltrimethoxysilane	PAMS	3,6
Poly(acrylic acid)	PAA	6
Tetramethylsilane	TMS	7
Tetraethoxysilane	TEOS	7
Trimethylethoxysilane	TMES	7

A.4. Formulation Summary

Formulation A: Standard geopolymer, high silica formulation

A mass of 19.00 g waterglass was added to 11.10 g Metamax HRM after any additives. The components were then mixed with the planetary centrifugal mixer for 180 s at 1000 RPM, and then debubbled for 60 s at 1200 RPM. The resulting Formulation is nominally 1•1•4.0•11. The viscous slurry was poured into molds and placed in curing conditions as appropriate.

Formulation A2: Standard geopolymer, high silica large mold formulation

A mass of 95.0 g waterglass was added to 55.5 g Metamax HRM and mixed in the planetary centrifugal mixer for 480 s at 1000 RPM, and then debubbled for 180 s at 1200 RPM.

The resulting formulation is nominally 1•1•4.0•11. The viscous slurry was poured into molds and placed in curing conditions as appropriate.

Formulation B: Standard geopolymer, low silica fFormulation

A mass of 18.50 g waterglass was added to 11.10 g Metamax HRM and mixed using the planetary centrifugal mixer for 180 s at 1000 RPM, and then debubbled for 60 s at 1200 RPM. The resulting Formulation is nominally 1•1•3.9•11. The viscous slurry was applied to the substrate using a spatula, and placed in curing conditions as appropriate.

Formulation C: Evaporative Geopolymer, No Pre-mixture

A mass of 2.78 g Metamax EF was placed in a polypropylene container (Solo Cup Co., Lake Forest, IL) and a prescribed quantity of water (usually 40.0 g) was added. Then 4.75 g waterglass was added to the mixture. The mixture was ultrasonicated for 5 minutes at 240 watts while stirred on a stir plate until well-mixed. The resulting dilute slurry had a nominal composition 1•1•4.0•z (z=197 for 40.0 g, or as specified) but some water evaporated during mixing. The sample was then placed in the humidity chamber or in a sealed container with a large excess of calcium sulfate (Drierite, W. A. Hammond Co., Xenia, OH), and maintained at 25 ºC until mass loss was not observed.

Formulation C2: Evaporative Geopolymer with Premix

A mass of 11.10 g Metamax EF was placed in a polypropylene container (Solo Cup Co.) and a prescribed quantity of water was added, along with 0.50 ± 0.03 g 40 wt% poly(methyl acrylate) solution (Darvan 821A, R. T. Vanderbilt Co., St. Norwalk, CN) and 19.0 g waterglass.

The resulting thick slurry (of composition 1•1•4.0•z, z=18.1, 22.9, 34.2, or 37.4, before additives) is sealed, stirred with a stir plate for up to seven days. This constituted the premix.

For the cured samples an amount of material equivalent to 0.025 mol geopolymer was removed, diluted to 1•1•4.0•197, and any additives were included at this time. The mixture was then ultrasonicated for 8 minutes at 240 watts while being stirred on a stir plate, and placed in the controlled humidity chamber or in a sealed container with a large excess of calcium sulfate (Drierite), and maintained at 25 ºC until mass loss was not observed.

Formulation D: Emulsion Geopolymer

A mass of 2.78 g Metamax EF was placed in a polypropylene container (Solo Cup Co.) and a proscribed quantity of water (usually 40.0 g) and some additives. The additives usually consisted of a hydrophobic phase and a surfactant phase, but some materials were found to fulfill both roles simultaneously. This mixture was then ultrasonicated for 9 minutes at 240 watts while being stirred on a stir plate. Then 4.75 g waterglass is added dropwise as quickly as possible, while ultrasonication continued for a further 6 minutes (a total of 15 minutes). This resulting dilute slurry had nominal composition 1•1•4.0•z before additives (z=197 for 40.0 g, or as specified), but some water and some additives evaporated during the mixing. The resulting mixture was placed in the controlled humidity chamber or in a sealed container with a large excess of calcium sulfate (Drierite), and maintained at 25 ºC until mass loss was not observed.

Formulation E: Premix Emulsion Geopolymer

A mass of 10.00 g Metamax EF was placed in a high density polyethylene container (Thinky Corp.) with 30.0 g water and 0.40 ± 0.03 g 40 wt% poly(ammonium methyl acrylate)

solution (Darvan 821A) and 16.67 g waterglass. The resulting slurry (of composition 1•1•3.9•50.0 before additives) is sealed, stirred with a stir plate for seven days. This constituted the premix.

An amount of material equivalent to 0.012 mol geopolymer was removed from the premix (15.72 g), placed in a polypropylene container (Solo Cup Co.), diluted to 1•1•3.9•197, and any additives were included at this time. The mixture was then ultrasonicated for 8 minutes at 240 watts while being stirred on a stir plate, and placed in the controlled humidity chamber or in a sealed container with a large excess of calcium sulfate (Drierite), and maintained at 25 ºC until mass loss was not observed.